

Final work : Numerical investigation of the ground vortex ingestion into the intake under crosswind

Auteur : Chennuru, Venkata Yashwanth Teja

Promoteur(s) : Dimitriadis, Grigorios

Faculté : Faculté des Sciences appliquées

Diplôme : Master en ingénieur civil en aérospatiale, à finalité spécialisée en "turbomachinery aeromechanics (THRUST)"

Année académique : 2021-2022

URI/URL : <http://hdl.handle.net/2268.2/15929>

Avertissement à l'attention des usagers :

Tous les documents placés en accès ouvert sur le site le site MatheO sont protégés par le droit d'auteur. Conformément aux principes énoncés par la "Budapest Open Access Initiative"(BOAI, 2002), l'utilisateur du site peut lire, télécharger, copier, transmettre, imprimer, chercher ou faire un lien vers le texte intégral de ces documents, les disséquer pour les indexer, s'en servir de données pour un logiciel, ou s'en servir à toute autre fin légale (ou prévue par la réglementation relative au droit d'auteur). Toute utilisation du document à des fins commerciales est strictement interdite.

Par ailleurs, l'utilisateur s'engage à respecter les droits moraux de l'auteur, principalement le droit à l'intégrité de l'oeuvre et le droit de paternité et ce dans toute utilisation que l'utilisateur entreprend. Ainsi, à titre d'exemple, lorsqu'il reproduira un document par extrait ou dans son intégralité, l'utilisateur citera de manière complète les sources telles que mentionnées ci-dessus. Toute utilisation non explicitement autorisée ci-avant (telle que par exemple, la modification du document ou son résumé) nécessite l'autorisation préalable et expresse des auteurs ou de leurs ayants droit.



Faculty of Applied Sciences
University of Liége

Numerical investigation of the ground vortex ingestion into the intake under crosswind

Submitted in partial fulfilment of the requirements for the degree of
Master's in Civil Engineer in Aerospace, professional focus in
"Turbomachinery Aeromechanics (THRUST)"

by Venkata Y.T. Chennuru

Academic year: 2021–2022

**Imperial College
London**

Author

Venkata Yashwanth Teja Chennuru
Department of Aerospace Engineering
University of Liége – KTH Royal Institute of Technology

Place for Project

Imperial College
London, United Kingdom

Internal Supervisor

Greg Dimitriadis
Professor
Department of Applied sciences
University of Liége

External Supervisor

Mehdi Vahdati
Principle Research Fellow
Department of Mechanical Engineering
Imperial College London

Abstract

Aiming to increase aircraft fuel efficiency, Ultra High By-pass ratio (UHBR) engines are gaining popularity. When operated under static or near static conditions, subject to crosswind, UBHR engines can experience a lip separation on the windward side of the intake and the formation of a ground vortex extending from the stagnation point on the ground into the intake called a ground vortex. These vortices create considerable stagnation pressure losses and flow distortion at the engine fan face affecting the efficiency of the engine and structural integrity of the fan. Furthermore, the ground vortices can generate forces that can suck debris from the ground into the intake, mainly over poorly maintained runways. This Foreign Object Digestion (FOD) can lead to compressor blades' erosion, reducing the engine's service life. Considering the advantages of numerical analysis over full and scaled model experiments, the ground vortex ingestion is studied numerically. Present work aims to provide the best numerical setup to analyse this phenomenon using the experimental data for validation.

Initially, a few studies are conducted to determine the appropriate turbulence model and the significance of the boundary layer profile for simulations. A grid sensitivity study is performed using steady-state RANS, and the vortex is learned to be stable in low crosswind conditions. URANS is solved for medium and high crosswind conditions to fully understand the vortex's unsteadiness using coarse mesh. The temporal convergence study determines the time stepping for the unsteady simulation. This research demonstrated periodic vortex motion in medium and high crosswind conditions at ≈ 10 Hz, and ≈ 22 Hz, respectively. Furthermore, the separation exists in high crosswind conditions, and the shear layer oscillates at a broadband frequency rather than a single or narrow band. Good agreement is found between the time-averaged URANS results and the experiment data using coarse mesh. The proposed numerical setup can therefore be used for further analysis of ground vortex ingestion studies.

Keywords: Ground vortex ingestion, unsteady distortion, crosswind conditions, Numerical setup.

Acknowledgement

The current research project's development and report submission brings the two-year MSc. THRUST joint degree to a close. During my studies, this program provided me with international experience at KTH University (Sweden) and the University of Liége (Belgium) and thesis development at Imperial College London (United Kingdom).

I want to thank my supervisor Professor Mehdi Vahdati for providing me with the opportunity and resources to work on my master's thesis in his research group at Imperial College. I thank his entire research team, especially Fanzhou Zhao, for providing his valuable input and support during my work. I also want to thank my internal supervisor, Professor Greg Dimitriadis, from the University of Liége, for his interest and insights into this project.

Special thanks to all my family members, mainly my mom, dad, and sister, for their support in pursuing my masters in Sweden. Most importantly, I want to mention my two closest friends who supported me emotionally and psychologically during the difficult moments of my life in London.

Finally, I would like to mention all my classmates in the THRUST programme for the last two years who helped me to adapt to the new learning environment and equally contributed to my growth.

Contents

Abstract	i
Acknowledgments	ii
List of Figures	vi
1 Introduction	1
1.1 Current Knowledge	2
1.2 Objectives	3
1.3 Outline	3
2 Literature Review	5
2.1 Inlet vortex occurrence	5
2.2 Mechanisms for Vortex Formation	6
2.3 Criteria for Vortex Formation	8
2.4 Past CFD studies	14
2.5 Chapter Summary	16
2.6 Deficiencies in Existing Literature	17
3 Experimental Data	18
3.1 Introduction	18
3.2 Non-dimensional variables	19
3.3 Experiment Intake Model	20
3.4 The 8' × 6' Wind Tunnel	21
3.5 Measurement Techniques	21
3.5.1 Pressure Measurement	22
3.5.2 Velocity Measurement	23
3.6 Testing conditions	24

3.7	Experiment results	25
3.8	Summary of AIAA PAW-05 results	26
4	Computational Methodology	29
4.1	Aerodynamic Flow Solver	29
4.2	Computational Domain	29
4.3	Grid and boundary conditions	30
4.4	Setup optimisation	31
4.4.1	Impact of inlet velocity profile	31
4.4.2	Turbulence model	33
4.5	Chapter Summary	36
5	Steady state analysis	38
5.1	Grid Independence Study	38
5.2	Discussion	47
6	Unsteady analysis	49
6.1	Analysis of Unsteady Simulations	49
6.1.1	Temporal convergence	49
6.1.2	High Crosswind Case	52
6.1.3	Medium Crosswind Case	55
6.2	Static pressure boundary condition	59
6.2.1	Medium Crosswind Case	60
6.2.2	High Crosswind Case	61
6.3	Comparison with experimental data	65
6.4	Chapter Summary	68
7	Conclusions and Recommendation	70
7.1	Conclusions on the Project	70
7.2	Recommendations for future work	72
Bibliography		78

List of Figures

1.1	Visualisation of an ingested ground vortex ©Keith Blincow	2
2.1	Ground vortex ingestion observed in real life engines.	6
2.2	Inlet vortex flow model	8
2.3	Streamlines associated with twin inlets at 90° of yaw in an irrotational upstream flow	9
2.4	Streamlines associated with inlet at 90° of yaw in an irrotational upstream flow .	10
2.5	Flow regime at (a) low Non-dimensional velocity ratio (U^*) and (b) high U^* , in an irrotational upstream flow	11
2.6	Correlation of U^* and height-to-outer-diameter ratio (H/D) for vortex formation	12
2.7	Contours of total pressure at the fan face for (a) height-to-lip-diameter ratio (h/D_l) = 0.25 and (b) h/D_l = 0.40	13
2.8	Flow into intake for 20 kts headwind + 4.4 kts crosswind	15
3.1	Schematic of intake illustrating the model dimensions.	21
3.2	Front view picture of intake model, with the total pressure rakes installed.	22
3.3	Total pressure measurement point within the intake duct for crosswind conditions (h/D_l = 0.25)	23
3.4	Measurement planes used in the experiments (h_l = 0.083 D_l)	24
3.5	Total pressure contours at the AIP for increasing crosswind speed	25
3.6	VLES computational results	27
4.1	Computational domain used for simulations	30
4.2	Comparison of inlet Boundary Layer (BL) for Uniform and imposed profile at 25 D_l /3 from intake centreline.	32
4.3	Mean Navier-Stokes residual of ρu_x for high crosswind with uniform and imposed BL profile at inlet.	33

4.4	Comparison of Intake Pressure Recovery (IPR) contours for with uniform and imposed BL profile with increasing U^*	34
4.5	The vortex-aligned average vector flow-field (a,b) with contours of normalised vorticity and (c,d) out-of-plane velocity flow-field for cases with uniform (left) and imposed (right) intake BL profile at $U^* = 5.2$	35
4.6	IPR contours for different turbulence models at $h/D_l = 0.25$ for $U^* = 5.2$	37
5.1	Mean Navier-Stokes residual of ρu_x for Low, Medium and High crosswind cases using fine mesh.	39
5.2	IPR contours for a $h/D_l = 0.25$ and $M_i = 0.55$	40
5.3	$u - v$ vector and vorticity field for a $U^* = 18.3$, $h/D_l = 0.25$ and $M_i = 0.55$	41
5.4	IPR contours for a $h/D_l = 0.25$ and $M_i = 0.55$	43
5.5	$u - v$ vector and vorticity field for a $U^* = 9.1$, $h/D_l = 0.25$ and $M_i = 0.55$	44
5.6	Mean Navier-Stokes residual of ρu_x for $U^* = 5.2$	44
5.7	IPR contours for a $h/D_l = 0.25$ and $M_i = 0.55$	45
5.8	$u - v$ vector and vorticity field for a $U^* = 5.2$, $h/D_l = 0.25$ and $M_i = 0.55$	46
6.3	Probe-1 on Particle Image Velocimetry plane (PIV) with FFT analysis on top and time series data of ω_z^* in the bottom	52
6.5	The vortex location superimposed on PIV plane to represent vortex major and minor motion	55
6.7	Variation of total pressure (top) and vorticity (bottom) at the AIP and PIV respectively at five instants of time for $U^*=9.1$	56
6.10	FFT analysis of probe-1 on Aerodynamic Interference Plane (AIP) on top and time series data of IPR in the bottom	60
6.13	Probe on PIV with FFT analysis on top and time series data of ω_z^* in the bottom	63
6.15	Variation of IPR at several x -planes parallel to AIP (top) and $z=0$ plane parallel to ground (bottom) through the intake at four random time instants	64
6.16	Comparison of time average data	66
6.17	Comparison of time average data	67
6.18	Averaged ground vortex core locations at the vortex measurement plane (experiment data highlighted in ovals) with markers representing the average location, bars indicate the standard deviation in $x - y$ plane	68

List of Tables

3.1	Crosswind Operating Conditions of intake at $h/D_l = 0.25$	24
4.1	Initial boundary condition used for the simulations	31
5.1	Non-dimensional parameters for different mesh sizes at $U^* = 18.3$	41
5.2	Non-dimensional parameters for different mesh sizes at $U^* = 9.1$	42
5.3	Non-dimensional parameters for different mesh sizes at $U^* = 5.2$	47
6.1	Imposed static pressure boundary condition values at intake exit	60

Nomenclature

List of Acronyms

SPIV	Stereoscopic Particle Image Velocimetry
PIV	Particle Image Velocimetry plane
IPR	Intake Pressure Recovery
AIP	Aerodynamic Interference Plane
BL	Boundary Layer
SA	Spalart–Allmaras
FOD	Foreign Object Debris
LES	Large Eddy Simulations
DC_{60}	Distortion coefficient
RANS	Reynolds-Averaged Navier–Stokes equations
UHBR	Ultra High By-pass Ratio
AIAA	American Institute of Aeronautics and Astronautics
POD	Proper Orthogonal Decomposition

List of Symbols

D_i	Intake throat diameter, m
D	Intake outer diameter, m
D_l	Intake lip diameter, m
h	Shortest distance between the intake and the ground plane, m
h_l	PIV plane height from ground plane, m
$P_{0,\infty}$	Free-stream total pressure, Pa
P_0	Total pressure, Pa
p	Static pressure, Pa
U_i	Intake centerline velocity, m/sec
U_∞	Crosswind velocity, m/sec
U^*	Non-dimensional velocity ratio, –
H/D	height-to-outer-diameter ratio, –
h/D_l	height-to-lip-diameter ratio, –
A_∞	Area of captured streamtube, –
u	Velocity component in x direction (x +ve to the intake), m/sec
v	Velocity component in y direction (y +ve to starboard), m/sec
w	Velocity component in z direction (z +ve away from the ground), m/sec
ω_z	out-of-plane vorticity component, s

Chapter 1

Introduction

One of the aspirational goals set by the International Civil Aviation Organisation (ICAO) in 2019 is to increase the fuel efficiency of the engines by 2% [1]. In the light of making aircraft engines more fuel efficient, Ultra High By-pass Ratio (UHBR) turbofans (as explained by Barbosa [2]) are considered a way to achieve this goal. The UHBR turbofan configuration comes with large intake diameters, which severely affects the flow entering the intake of the aero engine when operated close to the ground. Because of the larger intake, the distance between the intake and the ground is reduced for conventional wing-mounted engines. When this type of engine is operated under static or near static conditions, there is a possibility that a strong ground vortex can be ingested into the intake (Fig. 1.1).

Under these circumstances, this *ground (or inlet) vortex* can be a big problem. It stretches all the way from the ground plane into the inlet and can erode the blade by lifting ground debris or foreign particles into the intake [3],[4]. Besides, ingesting the inlet vortex will create non-uniform inflow in front of the aero engine, referred to as inlet distortion [5],[6]. The performance of the fans and compressors can be grievously affected by inlet distortion in terms of efficiency, performance, life and stability. During an intake design, the inlet flow distortion is calculated at the Aerodynamic Intake Plane (AIP), which is the crossflow plane located close to the engine fan. Ideally, the inlet flow conditions at the AIP should be uniform; however, inlet distortion is omnipresent during usual engine operation owing to the variations in air pressure, temperature, wind speed and directions.

With fan diameters growing larger and larger, fan vibration has been recognised as an additional repercussion of the ground vortex ingestion [8],[9]. The distorted flow associated with the ground vortex entering the intake introduces pressure, momentum losses, and large velocity gradients, which can seriously alter the inlet flow angle seen by the fan blade. This can poten-



Figure 1.1: Visualisation of an ingested ground vortex ©Keith Blincow [7]

tially lead to a high level of vibrations and the possible failure of fans due to high cycle fatigue. Considering all the ill effects of inlet distortion and the challenges faced by engine manufacturers, understanding inlet distortion is paramount. On top of that, the current knowledge on distortion is inadequate; therefore, further research on this front is required.

The full-scale tests with the engine are mostly expensive, and the small-scale models fail to reproduce the entire flow field of the real engine. Moreover, the experiments studying the effects of the ingested vortex can damage the engine and prove very costly. In contrast, Computational Fluid Dynamics (CFD) simulations provide an economical and faster alternative. With the advancement in numerical algorithms and computational capability, CFD is becoming a favourable alternative to experimental studies.

1.1 Current Knowledge

The mechanisms of vortex formation and ingestion have been a popular research subject since the 1950s [4]. Since then, the inlet-vortex phenomenon has been examined by several investigators because of the ingestion problems initially and later motivated by the engine instability. Several experiments both small-scale ([10], [3]) and full-scale ([4],[11]) have been performed to understand the formation of the ground vortices.

It is identified that the existence of a stagnation region in front of the intake is believed to be required for the vortex to appear. Rodert and Garrett [4], in his work, found that the air entering the engine from all directions creates a region on the ground close to the intake where there is no flow creating a stagnation region. This has been recognised to depend on two key

non-dimensional parameters fundamentally. The first one is the ratio of intake centreline height to inlet diameter (H/D_l), and the second one is the ratio of the inlet throat velocity to the free-stream velocity (U_i/U_∞). For this to happen, the capture streamtube must interact with the ground surface, H/D_i must be small, and U_i/U_∞ must be enormous. This requirement is later experimentally confirmed by Brix et al. [12].

Today's design trend in the industry to avoid ingestion of inlet vortices depends on the vortex map where the previous researchers have correlated combinations of H/D_l vs U_i/U_∞ for when vortices are observed, and no-vortices are identified. This led to establishing two regions with and without the vortex as a function of ground clearance and velocity ratio. However, this graph doesn't provide any details on what happens to the vortex characteristics as the engine operates in the vortex region.

Several researchers have tried different methods to eliminate the stagnation point on the ground, which is the main reason for the existence of the ground vortex, were documented [13]. Most mitigation methods used a jet of air from the compressor and pointed at the vortex formation region to eliminate the Foreign Object Debris (FOD) issue. However, after review, these methods were not very effective and created more problems than the vortex itself. Despite the flow control methods being developed, the current design trend of increasing the size of the engine is going to make the intake susceptible to ingesting the ground vortex. Therefore it is becoming vitally important to analyse and understand the severity of the vortex when it is formed.

1.2 Objectives

This current work mainly aims to numerically understand the vortex characteristics during different crosswind conditions. The main objectives of this project are:

1. To study and understand the unsteadiness of the ground vortex motion on the intake in crosswind conditions using numerical analysis.
2. To find out the best numerical setup to reproduce the experimental testing conditions.
3. To assess the accuracy of the current solver, HADES[®](see § 4.1) in simulating the aero-dynamic impact of ground vortex ingestion on inlet performance.

1.3 Outline

The introduction presented in this chapter is followed by a survey of current literature available regarding the ingestion of ground vortex in chapter 2. Chapter 3 explains the experimental data

used to validate the results from the current work and the essential non-dimensional parameters used. Then, the computational methods employed in this thesis, providing insight into numerical modelling and setup, are explained in chapter 4. Chapter 5 discusses the steady state results, followed by unsteady results presented in chapter 6. Finally, chapter 7 concludes the work by summarising the most relevant conclusions, discussing the shortcomings of this work and providing recommendations for future work.

Chapter 2

Literature Review

A brief review of the published work concerned with the formation of the ground vortex is presented in this chapter. In the first section, the cases of real-life ground vortex ingestion are introduced. Then in section 2.2, the mechanisms involved in forming vortices are presented based on the previous research. Followed by the criteria for the formation of the vortex that has been established to date. Finally, a concise discussion of the available CFD studies in the public domain is reviewed.

2.1 Inlet vortex occurrence

Since the beginning of jet engines in large commercial airlines in the mid-twentieth century, ingestion of foreign objects has been an exciting topic of study. In time, the inlet-vortex phenomenon has been examined by several investigators because of the ingestion problems initially and later motivated by the engine instability. In the beginning, the studies have been primarily concerned with predicting the suction force of the ground vortex. However, a vortex also represents a severe flow distortion at the inlet of the fan leading to a loss in total pressure and even fan damage. It is therefore highly desirable to understand the conditions at which the vortex is formed, to evaluate the susceptibility of an installation for ground vortex ingestion.

The ground vortex is generally not visible in normal atmospheric conditions. However, in a humid climate, due to the high velocities within the vortex core, the temperature of local flow can go below the dew point, encouraging condensation of the associated flow [14]. Moreover, if water or sand is present on the ground around the stagnation region, it can be sucked into the vortex and thus outline the ingestion.

Figure 2.1 shows the examples of inlet vortex formation and ingestion in four distinct real-life scenarios: (a) shows the ingestion of propulsion-induced vortex flows into the inlet of YC-14



Figure 2.1: Ground vortex ingestion observed in real life engines (images (a),(b),(d) are from [14])

during high thrust conditions (the engine is placed on top of the wing), (b) shows the ground vortex ingestion among engine intake, ground and the adjacent engine for Asuka STOL (Short Take-Off and Landing) research aircraft during static conditions, (c) shows the vortex ingestion into the intake of Rolls-Royce RB211-524G engine during the crosswind conditions, and (d) represents the ingestion of ground vortex generated by an outboard propeller for C-130 transport aircraft. These figures demonstrate that the ground vortex can occur in a wide range of operating and design scenarios.

2.2 Mechanisms for Vortex Formation

The mechanisms of vortex formation and ingestion have been a popular research subject since the 1950s [4]. Initially, experiments were conducted using the engines on the test beds to study the inlet vortices ([4],[11]). Since it is very costly to conduct full-scale experiments, scaled model inlets were tested in wind tunnels [3] towards the beginning of the 1970s. In the last decade

with the advancement of numerical algorithms and computational capabilities, CFD is used to understand this complex phenomenon [15],[16],[17].

To understand the reason behind FOD ingestion into jet engines, Rodert and Garrett [4] performed experiments with an axial flow jet engine and found out that the ground vortices were the main reason for FOD in the engines. This formation of the ground vortices was found to be dependent on the engine speed, engine height and surface speed. Rodert and Garrett also stated that the air entering the engine from all directions creates a region on the ground close to the intake where there is no flow creating a stagnation region. This acts as a focal point for the vorticity upstream to be concentrated and stretched into the intake. Then Klein [10] Kline [18] performed a series of experiments and proposed two more conditions for the formation of inlet vortices:

1. The existence of ambient vorticity (independent of the presence of inlet at the ambient location) in the fluid drawn into the intake.
2. There must be an updraft from the stagnation point to the inlet.

Klein also proved that the boundary layer on the ground is not an important source of vorticity. Fig. 2.2 is a model proposed by Colehour and Farquhar [19], and they stated that if the circulation of the flow at the stagnation region is not zero, then the flow field will extend to infinity, creating a vortex. Since, in the case of an intake, an inlet suction is present above the stagnation region, the vortex will enter the intake from the stagnation region.

Later De Siervi *et al.* [20] performed some pioneering experiments using scaled nacelle models in a water tunnel. Hydrogen bubbles were used in his experiments to visualise the vortices in the flow. De Siervi *et al.* famous experiment with a twin-inlet model in which one engine acted like a mirror image of the other instead of the ground is shown in Fig 2.3. This experiment, performed in steady state crosswind conditions with the irrotational upstream flow, revealed a new mechanism for vortex formation, which was not recognised before. Their experiments revealed two important conclusions about the formation of a vortex:

1. The ground boundary layer is not needed.
2. The presence of ambient vorticity is not essential.

The circulation of the inlet and the trailing vortices are roughly equal in magnitude but opposite in sign because there was essentially no circulation around the intake at a location far from the lip [20]. The fact that the vortex appeared in an irrotational flow field with no upstream vorticity sources disproves the first condition proposed by Klein. De Siervi *et al.* suggested that vortex

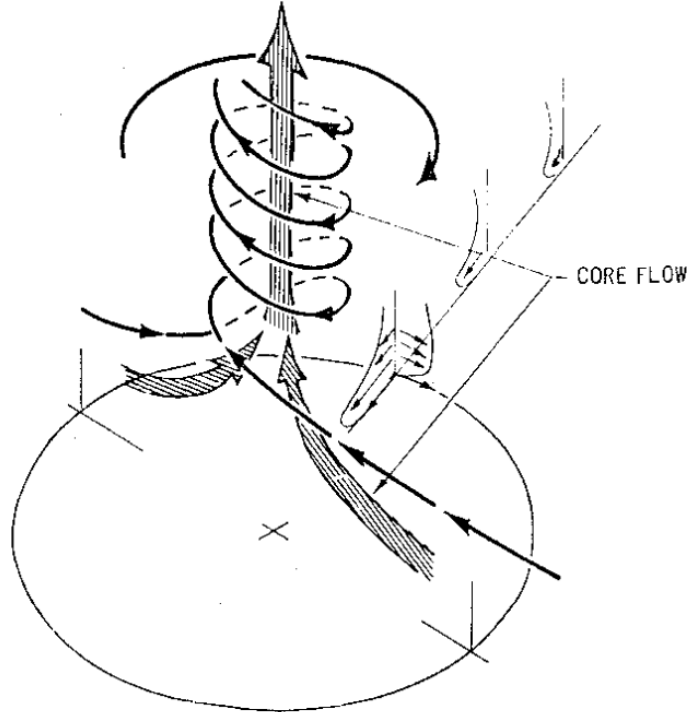


Figure 2.2: Inlet vortex flow model [19]

is produced due to the asymmetry produced by the inlet flow, but the vorticity source was still not found. By studying the case in transient conditions, it was concluded that the source of vorticity was created by the viscous effects of the boundary layer formed outside the inlet. This work was complemented by Liu *et al.* [21] in his work using smoke flow visualisation to provide some quantitative data in the crosswind inlet conditions.

2.3 Criteria for Vortex Formation

The sucked (or captured) streamtube of air is defined as the streamtube which divides the flow into internal that is ingested into the intake and external flow that travel downstream outside the intake. The characteristics of the sucked streamtube can be estimated from the conservation of mass as follows:

$$\rho_\infty A_\infty U_\infty = \rho_i A_i U_i$$

$$\frac{A_\infty}{A_i} = \frac{\rho_i}{\rho_\infty} \frac{U_i}{U_\infty}$$

For an incompressible flow this area ratio (or capture ratio) A_∞/A_i will be equal to U^* . De Siervi *et al.* [20] performed some experiments with the inlet in an irrotational flow by varying U^* , and at high values of approximately 20, he observed a vortex in the lower part of the inlet at a 6’O clock position with a clockwise sense of rotation when viewed looking into the inlet. Further

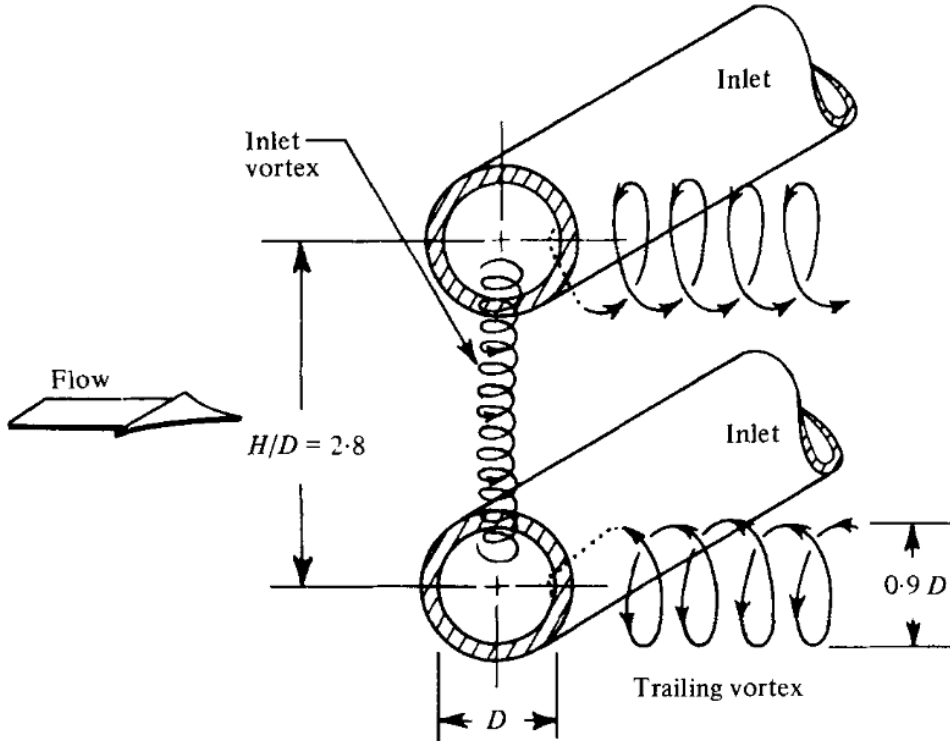


Figure 2.3: Streamlines associated with twin inlets at 90° of yaw in an irrotational upstream flow [20]

examination of the flowfield revealed another important feature, the presence of a *trailing vortex*, on the downstream side (outside) of the inlet lip region, as shown in Fig. 2.4. From the hydrogen bubble visualisation of the flow, he concluded that the trailing vortex is considerably larger than the inlet vortex in diameter and rotates in the clockwise direction when viewed from upstream. Since the flow is irrotational, to begin with, there cannot be only a single vortex because of the large net circulation around the inlet at any station along the inlet. So, the presence of the inlet vortex requires the presence of a trailing vortex with a circulation of comparable magnitude and the opposite direction. Furthermore, De Siervi *et al.* observed a change in circulation along the length of the inlet by examining the separation of the flow as it passed over (or under) the inlet from outside. This change in circulation was linked to a skew in the separation line, which is qualitatively represented in Fig. 2.4.

At the far-field inlet section, the vortex was almost at a 12'O clock position, which settled roughly at a 4'O clock position at the lip of the inlet with an increase in the velocity. This combination of a shift in the position and the increase in the velocity implied a substantial circulation at the lip was due to the non-symmetric pressure field resulting from the ground-plane-cylinder interactions at high U^* . However, this variation in the circulation along the inlet is directly linked to the formation of the trailing-vortex system and thus led to the generation

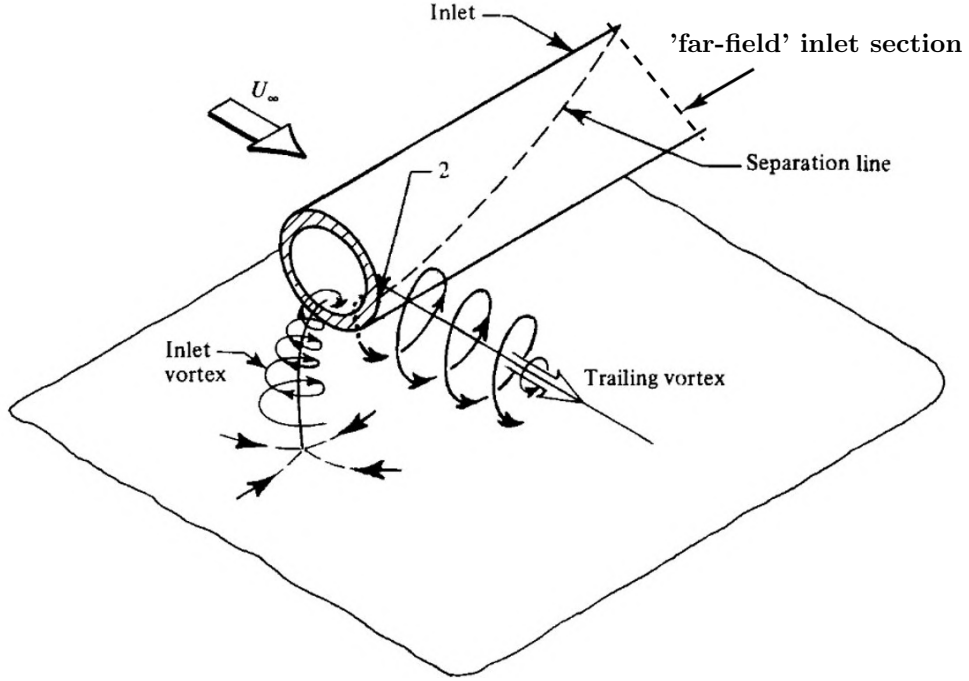


Figure 2.4: Streamlines associated with inlet at 90° of yaw in an irrotational upstream flow [20]

of the inlet-vortex.

De Siervi *et al.* [20] went on to perform another experiment on the same configuration by varying the U^* and established a relationship between the capture area and the velocity ratio as illustrated in Fig. 2.5. The velocity ratio U^* determines the projection of the captured streamtube at the far field relative to the intake dimension. When the Crosswind velocity (U_∞) is large, the engine mass flow demand will decrease; as compensation, the Area of captured streamtube (A_∞) also decreases to match this demand. In this case, from Fig. 2.5a, no ground vortex is observed when the sucked streamtube has no ground plane contact. However, two contra-rotating vortices will trail from the leeward side of the intake.

As the velocity ratio gradually increases, the captured area of the streamtube will also increase. Eventually, the sucked streamtube becomes large enough and comes into contact with the ground plane, as shown in Fig. 2.5b. Then the ground vortex, the trailing vortex system, abruptly appears. This intermittent attachment behaviour of the ground vortex and the abrupt behaviour by which the vortex attaches to the ground was also observed by Brix *et al.* [12]. All the water tunnel experiments performed by De Siervi *et al.* [20] were only qualitative in nature. Moreover, the influence of the distance between the inlet and the ground, H , can play a part in the interaction between the sucked streamtube and the ground plane. This introduces another significant non-dimensional parameter, H/D , alongside the U^* .

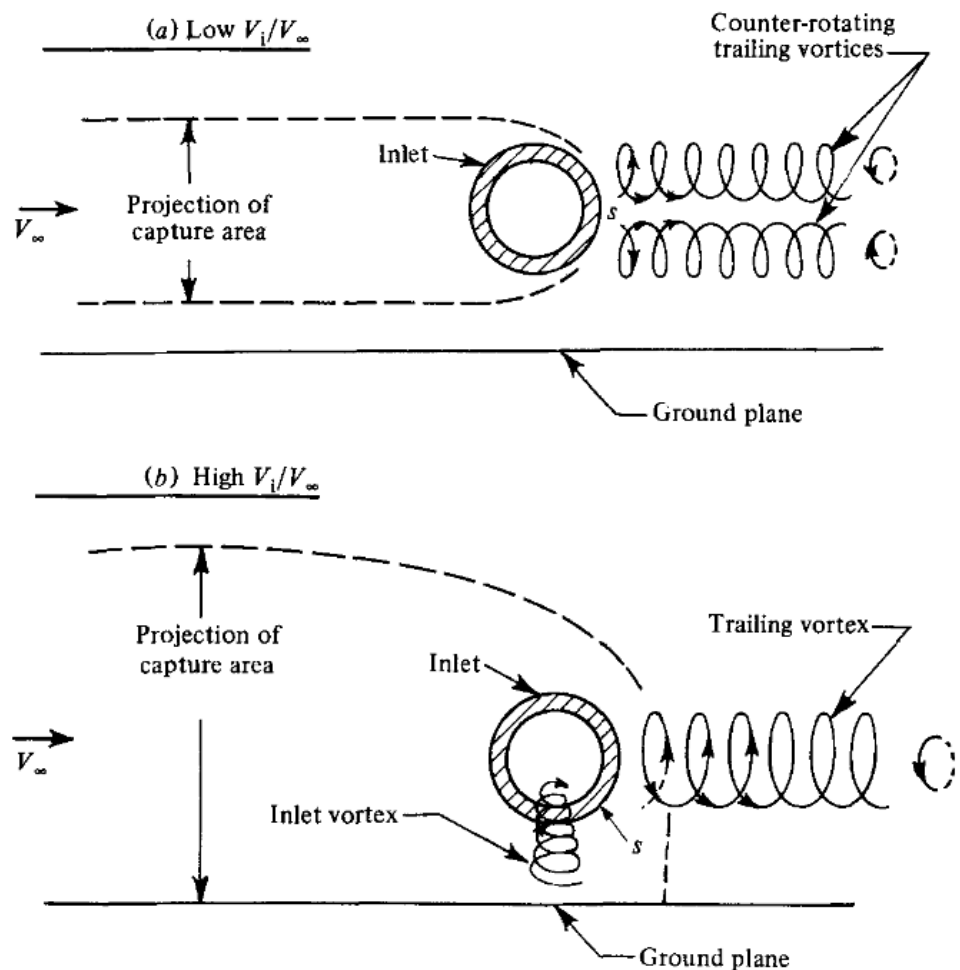


Figure 2.5: Flow regime at (a) low U^*/V_∞ and (b) high U^*/V_∞ , in an irrotational upstream flow [20]

Subsequently, Liu [22], Shin *et al.* [23], provided quantitative measurement data for the inlet vortex formation through their experimental investigation. The dependency of H/D , and U^* was graphically illustrated by Liu by correlating the two non-dimensional parameters for cases with and without vortices. The no-vortex/vortex map in Fig. 2.6 presents two regions; the conditions where a vortex can be observed and cannot. Based on this Shin *et al.* constructed a vortex map around all the existing data from the previous researchers. Additionally, Nakayama and Jones [24] presented an empirical criterion based on previous research in Eq. 2.1 which is also included in the Fig. 2.6

$$A_o/A_i = 24(H/D_i) - 17 \quad (2.1)$$

Nakayama and Jones [24] performed their experiments on recent high-bypass ratio engines for small H/D , and the results contradicted all the aforementioned boundaries. His data indicates that a vortex can form lower than reported velocity ratios. It should also be noted that all the experiments performed by Liu *et al.* [21] and Shin *et al.* [23] were purely crosswind configurations, and the estimations were based on flow visualisations only.

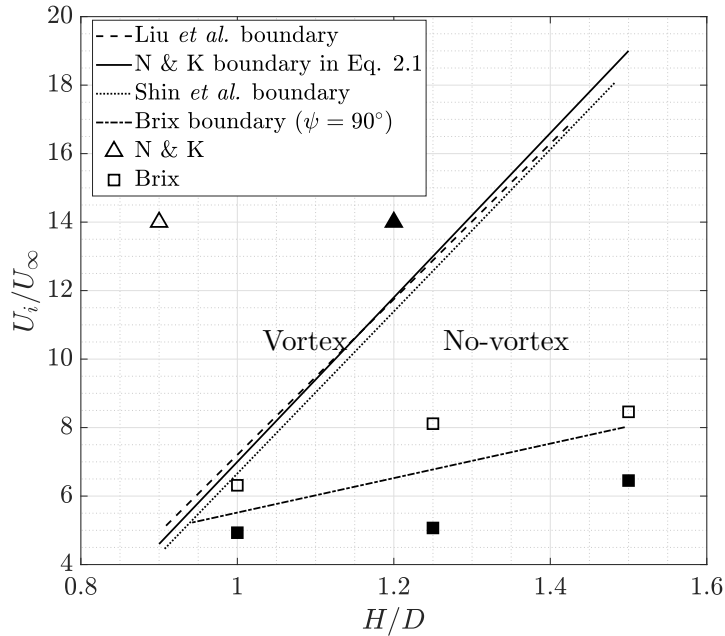


Figure 2.6: Correlation of U^* and H/D combinations revealing a region of vortex formation and no-vortex formation (with filled and unfilled markers respectively)

In the early 2000s, Brix *et al.* [12] presented a vortex formation map with a criterion for crosswind conditions, extracted approximately and included in Fig. 2.6. It is unknown whether this criterion was based on quantitative visualisation results, but he proposed a considerable difference between his established boundary under crosswind conditions and the existing thresh-

olds. This disparity can be attributed to potentially different experimental conditions and the different methods used to detect a vortex. But, on the whole, it can be noted that for higher U^* , the intake doesn't have to be very close to the ground for the existence of a ground vortex. More recently, Murphy [5] during his PhD studies, conducted an extensive study on a scale model for a wide range of experimental conditions. He varied both the non-dimensional parameters (U^* , H/D) under headwind, crosswind, quiescent and take-off conditions. Furthermore, he was one of the first researchers to use Stereoscopic Particle Image Velocimetry (SPIV) to study the inlet vortex and provide some quantitative data regarding the vortex on the ground plane (more details of the experiment are provided in § 3). His data revealed that the inlet vortex strength increases with a reduction in the U^* for a constant h/D_l , and the strength of the vortex will reduce (or will disappear) as the h/D_l is increased for a constant U^* (shown in Fig 2.7). These results are consistent with the mechanism proposed by De Siervi *et al.* [20] that the strength of the vortices depends greatly on the vorticity generated along the inlet body and consequently on the approaching freestream velocity.

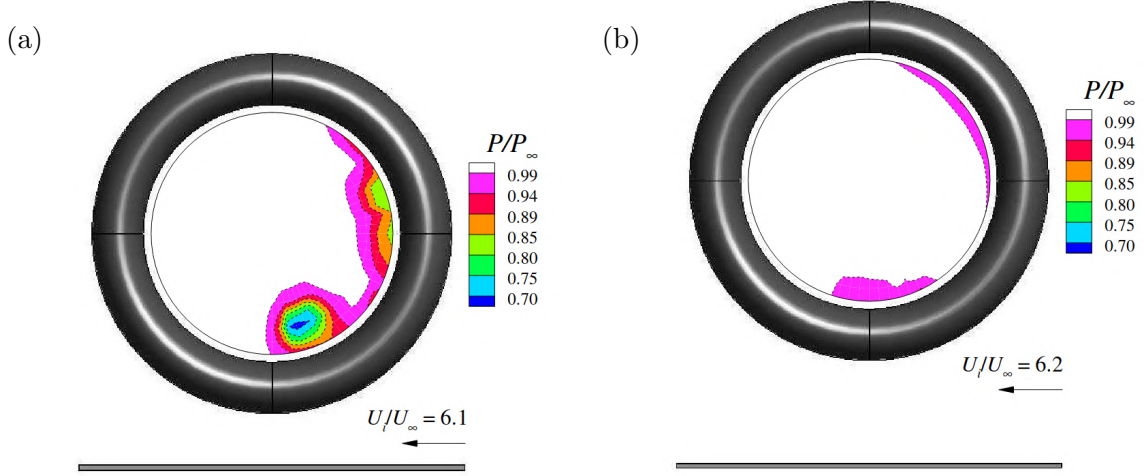


Figure 2.7: Contours of total pressure at the fan face for (a) $h/D_l = 0.25$ and (b) $h/D_l = 0.40$ at a comparable velocity ratio of $U^* \approx 6.2$ and at constant $\delta^*/D_l = 0.93$. [5]

Moreover, Murphy concluded that the vortex formed in crosswind conditions is much stronger than the ones formed in headwind conditions, which led to distortion at the fan face of up to 40 times stronger than in the latter case. Besides, faster crosswinds will yield a stronger ingested vortex with high core vorticity and can lead to separation on the windward side of the intake lip. This provides all the more reason to investigate the ground vortices in crosswind conditions numerically.

2.4 Past CFD studies

There has been increasingly more published literature to study the behaviour of ground vortices using CFD in the last 12 years. Karlsson and Fuchs [25],[26] were one of the first to study the ground vortex using Large Eddy Simulations (LES). They performed computation under headwind and crosswind conditions at a fixed H/D of 1 at a U^* of 10, with a Re of 55000 based on inner diameter (D_i). Their data reveal a sequence of flow modes with time. They classified these large vortex structures with their characteristic frequency and their shape. Further analysis showed the presence of multiple ground vortices, stream-wise vortices and traces of horseshoe vortices from the ground. Karlsson and Fuchs note that the ground vortex would break down without any change in the test parameters and would start forming again as described by Bissinger and Braun [27].

Consequently, Secareanu *et al.* [28] has performed LES to study ground vortices and validated his data against Laser Doppler Anemometry (LDA) and 2D Particle Image Velocimetry (PIV) data at the same operating conditions. He obtained data on the ingestion of particles by a vortex-inlet system. Despite the difficulties, the datasets showed a very good agreement. Therefore, from these studies, it can be said that the LES technique correctly predicted the flow physics.

Yadlin and Shmilovich [29] performed some Reynolds-Averaged Navier–Stokes equations (RANS) simulations of ground vortex formation for an extensive range of configurations, including multiple intakes. The results agree with the general full-scale observations of intake-to-intake vortices and fuselage to intake vortices. Jermy and Ho [30] performed computational studies using RANS equations in ANSYS Fluent solver to study the ground vortex under headwind conditions. The results correctly predicted the basic flow phenomenon, but the usage of incompressible flow equations (though the flow speed is in the compressible range). Additionally, a grid size of 0.1 – 0.2 million was used for the simulations, implying a low domain and boundary layer resolution. This parameter choice affected his results near the lip and AIP regions.

Green [8] conducted a numerical investigation on a large civil fan assembly and found the presence of the ground vortex (Fig. 2.8). The movement of the ground vortex on the ground is the major cause of resonant vibration in the fan blade. He also found that the strength of the vortex is directly related to the level of force seen on the blade. Whereas the location of the vortex (in terms of spanwise position on the blade) influences the interaction of the modeshape. Furthermore, the size of the vortex had an impact on the harmonic content of the excitation force. Large vortices generate stronger excitation on the low engine modes and small vortices

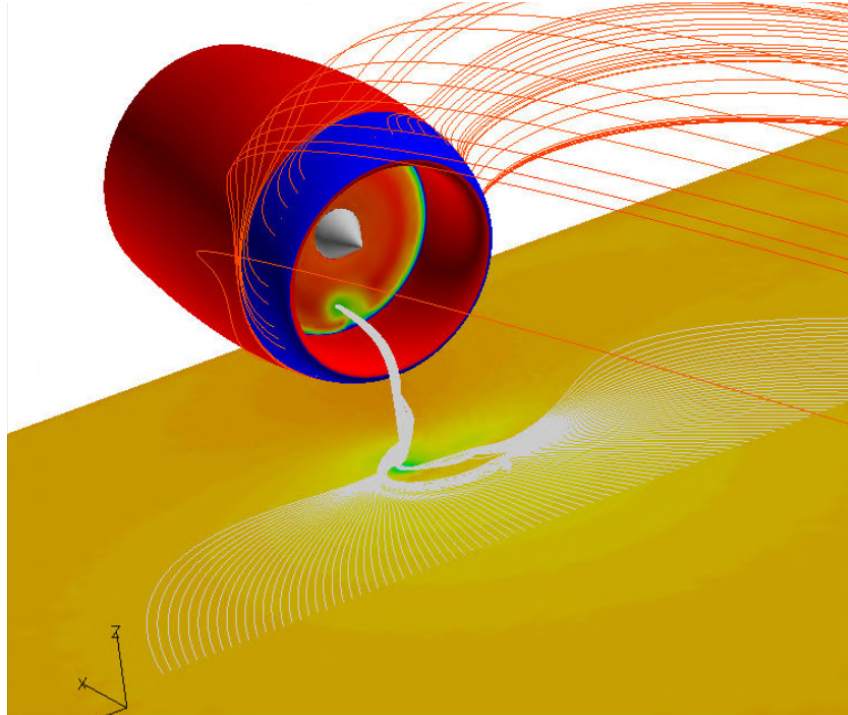


Figure 2.8: Flow into intake for 20 kts headwind + 4.4 kts crosswind [8].

influence the high engine orders.

Trapp and da Motta Girardi [15],[16] performed steady-state RANS computations on DLR-FR nacelle with almost 5 millions elements. The simulations were performed using different types of wall boundary conditions, slip and no-slip, and found that there has to be at least one no-slip boundary condition for the ground vortex to exist. Furthermore, he performed simulations considering viscous and inviscid flow and concluded that only viscous flow produces a ground vortex even though vortical flows are generally considered inviscid. Though the flow physics from all these published results agree with the mechanisms proposed by De Siervi *et al.* [20], there was no experimental data to validate their numerical solutions.

Zantopp *et al.* [31], Mishra *et al.* [32] have also studied the ground vortex formation computationally by using Murphy [5] data for validation purposes. The formerly performed simulations under headwind and crosswind conditions, while the latter performed simulations under a wide range of yaw angles (ψ). Zantopp *et al.* found that under most headwind conditions, the flow field is unsteady, and the unsteady characteristics were affected both by the U^* and H/D . Furthermore, using URANS, Zantopp *et al.* produced good qualitative results of the basic trends of the ground vortex flow field for both headwind and crosswind conditions. Moreover, his results show that the vortex strength decreases as the yaw angle ψ 90° to 30° (at a step of 10°). This is further complemented by Mishra *et al.* computations at different ψ , revealing the strongest

vortex systems under tailwind and crosswind conditions.

More recently, Horvath [33] performed URANS simulations to study the transient formation process of the inlet vortices and used Murphy [5] experimental data for validation. The fundamental flow physics of the trailing, ground and secondary vortices were captured, and the behaviour of the vortices with time was studied. The near-ground static pressure from the results supported the coexistence of multiple weak inlet vortices that merge into a strong inlet vortex. The author also suggested that velocity ratio correlation for a given H/D ([20]) is not applicable for the unsteady vortex formation process. Considering that the results are numerical and, in the author's words, "quantitatively, comparing the numerical data with the experiments is not accurate enough". The validity of his conclusions could be questioned.

Chen *et al.* [17] investigated the ground vortex field and nacelle inlet flows both experimentally and numerically using steady-state RANS at a low engine speed of 26 and 32 m s^{-1} . The results suggested that the ground vortex intensity increases and decreases with U^* for a constant U_i . While the ground vortex frequency is inversely related to its intensity, it ranges from 9 Hz to 22 Hz. The authors also observed that the ground vortex is blown away with an increase in U^* and provided four ground vortex blown-away phases, namely the encouraging phase, the initial blowing phase, the rapid blowing phase and the end blowing phase, depending on the variation of vortex intensity on the ground and its influence on the inlet distortion.

Considering the seriousness of the ground vortex ingestion and the unavailability of extensive computational research in this area, the society of American Institute of Aeronautics and Astronautics (AIAA) has conducted a Propulsion Aerodynamic Workshop [34] based on Murphy [5] experiments under crosswind conditions in November of 2020. The objective is to assess the accuracy of existing computer codes and modelling methods in simulating the aerodynamic impact on the inlet performance by ground vortex ingestion. The summary of all the work done as a part of the workshop is presented in §3.8 after the experiment details for a better understanding of the reader.

2.5 Chapter Summary

This chapter presents an overview of the ground vortex problem, recapitulating the basic mechanisms of vortex formation from literature, several observations made by the previous investigators and their conclusions. Researchers postulated some conditions for the existence of a ground vortex which were later complemented by experimental and numerical results. This is the summary of the current knowledge on ground vortices in aircraft:

1. Two fundamental requirements for the formation of the ground vortex are:
 - A ground plane stagnation point ahead of the intake suction.
 - A source of vorticity in the flow.
2. The dependency of the non-dimensional height h/D_l and velocity ratio U^* on the formation of the inlet vortices during crosswind conditions.
3. Under crosswind conditions, the vortex system comprises a strong ground vortex and a trailing vortex from the leeward lip of the intake.
4. The vortex formed in crosswind conditions has a more severe effect on the fan than the ones formed in headwind or tailwind conditions.

2.6 Deficiencies in Existing Literature

Ground vortex ingestion is still not well understood despite having been an interesting research topic for almost seven decades. While efforts are increasingly devoted to the research of understanding its motion using CFD, several challenges and unknowns still exist in this area. These can be outlined as:

1. Axiomatically, the motion of the ground vortex is very complex; most of the results available in CFD literature are not validated against the experiments to establish the accuracy of their method or solver.
2. Conventionally, Direct Numerical Simulations (DNS) can predict the behaviour better, but considering the computational cost, a cheaper alternative should be tested and employed to study this problem for industrial purposes.

Chapter 3

Experimental Data

3.1 Introduction

One of the objectives of this project is the validation of the developed CFD code (HADES[®]) for the numerical study of distortion on intake geometry in crosswind conditions. This validation is performed based on the experiment carried out on an intake geometry. These experiments were performed in a low-speed wind tunnel by Dr John Murphy as a part of his PhD work at the Cranfield University in 2008 [35]. This data was also recently used for 5th AIAA Propulsion Aerodynamic Workshop (PAW05) 2020 [34] to assess the accuracy of the existing computer codes and modelling techniques in simulating the impact of ground vortex ingestion on the performance of inlet.

It consisted of a cylindrical intake mounted in the centre of the wind tunnel working section close to the ground plane. The experiment was performed under different crosswind conditions. The time average pressure distribution was extracted using the pressure taps, and the velocity was calculated using SPIV during the measurements.

This chapter initially presents the important non-dimensional parameters vital in understanding the formation and the characteristics of the ground vortex. Followed by a description of the experimental model, wind tunnel and the measurement techniques used in the experiments. Then the testing conditions provided by the AIAA PAW-05 [34] are presented and the results recreated from the data are analysed. Finally, the work performed by the participant companies are research institutes in the workshop is summarized.

3.2 Non-dimensional variables

This section explains some of the relevant parameters used in Murphy's PhD thesis [5] and other non-dimensional variables used in this report. The variables used in this report are consistent with the experiments for clarity and validation.

Non-dimensional vorticity: In this study, the instantaneous vorticity component, ω , is non-dimensionalised by the Intake centerline velocity (U_i) and the Intake lip diameter (D_l). Throughout this report, the non-dimensional vorticity is denoted by ω^* and is used as the primary descriptor to characterise the vortex. Particularly, since the behaviour of the vortex is studied on the ground plane (parallel to $x - y$), the out-of-plane vorticity component (ω_z) (Eq. 3.1) is often used to understand the behaviour of the vortex.

$$\omega_z^* = \frac{\omega_z D_l}{U_i} \quad (3.1)$$

Intake Pressure Recovery: IPR is the non-dimensional pressure term which is the ratio between the total pressure at that location on AIP, $P_{0,AIP}$ to the Free-stream total pressure ($P_{0,\infty}$). This non-dimensional quantity will help in understanding the impact of the ingested vortex on the intake AIP (Eq. 3.2). The lesser the value indicates, the more equivalent total pressure loss is present in the AIP region.

$$IPR = \frac{P_{0,AIP}}{P_{0,\infty}} \quad (3.2)$$

Ground Clearance: In this report, the ground clearance is described as the shortest distance between the intake lip and the ground, h , normalised by the intake lip diameter, D_l (Fig. 3.3). This parameter is of great importance to this study. As mentioned in § 2, the distance between the ground clearance decreases with the increasing design trend of high-by-pass ratio turbofans. Making the intake more susceptible to ingesting a ground vortex over a wider range of operating conditions. For this entire report, the ground clearance, h/D_l , is a constant of 0.25.

Velocity Ratio: U^* is the ratio between the U_i and the Crosswind velocity U_∞ . It is derived from the law of conservation of mass. As explained in the previous section, with increasing the U^* for given ground clearance, the sucked streamtube will also increase. This streamtube is more likely to interact with the ground, promoting vortex formation.

Distortion coefficient: Another parameter used in conjunction with IPR is distortion coefficient, DC_{60} . This distortion descriptor is based on the difference between the area-weighted average total pressure at AIP, and the worst average 60° sector total pressure, $\bar{P}_{0,min,60}$ divided

by the average dynamic head at the AIP, \bar{q}_f .

$$DC_{60} = \frac{\bar{P}_{0,\text{avg}} - \bar{P}_{0,\text{min},60}}{\bar{q}_f}$$

Where \bar{q}_f can be simplified as the difference between the weighted average total pressure and the static pressure at AIP. Therefore, the above equation modifies as:

$$DC_{60} = \frac{P_{0,\text{avg}} - P_{0\text{min},60}}{P_{0,\text{avg}} - P_{\text{avg}}} \quad (3.3)$$

It should also be noted that, while DC_{60} is used a lot by aerodynamicists in studying or measuring distortion, it is by far not the best representation of the severity of distortion.

Non-dimensional Circulation: The circulation can be calculated by integrating the vorticity over the circular areas with increasing radial distance from the vortex centre (see [5]). It is related to vorticity by the following relation:

$$\bar{\Gamma} = \int \omega_z dA$$

It is expected that by non-dimensionalising the circulation (Γ^*), it will remain constant if the intake velocity (U_i) or the intake diameter (D_i) is altered (see [5]). Therefore, Γ^* takes the form:

$$\Gamma^* = \frac{\bar{\Gamma}}{D_l U_i} \quad (3.4)$$

Boundary layer thickness: This parameter is characterised using the displacement thickness of the boundary layer, δ^* , normalised by the intake lip diameter, D_l . The boundary layer profile was provided by the experiments, and a small study was performed in the § 4.4.1 to study its effect on the vortex characteristics.

3.3 Experiment Intake Model

The intake geometry was axisymmetric, cylindrical in shape and an approximate $1/30^{\text{th}}$ scaled model. A schematic of this model is given in fig. 3.1. This model did not include any central hub or a rotating fan. The inner diameter (D_i) of the intake is 0.1 m with a ratio to the outer diameter (D/D_i) equal to 1.4. The lip diameter, often referred to as intake diameter (D_l), is 1.2 times the inner diameter of the intake (D_i). The intake length (L_i) is $7D_l$, and the elliptical lip has an axis ratio of 2.

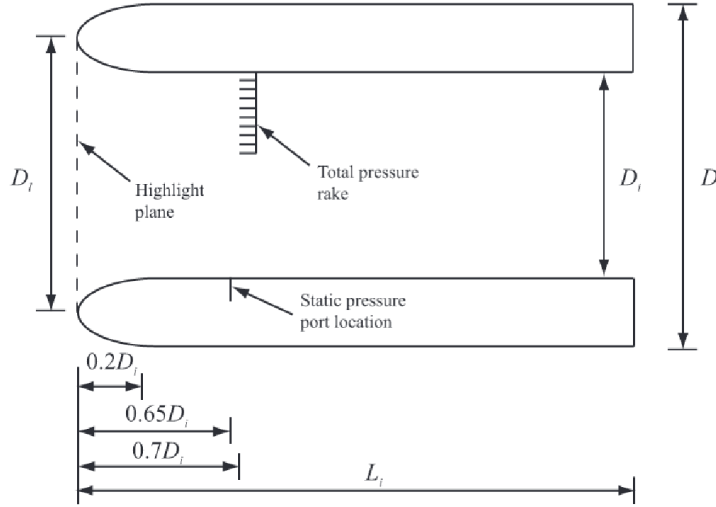


Figure 3.1: Schematic of intake illustrating the model dimensions [5].

3.4 The $8' \times 6'$ Wind Tunnel

These experiments were performed in a low-speed wind tunnel owned by Cranfield University. It has a working section of $2.4\text{ m} \times 1.8\text{ m}$, and it is a closed return, closed test section wind tunnel. The operating wind speeds of the tunnel range from 5 m s^{-1} to 50 m s^{-1} with low incoming turbulence flow ($T_i < 0.1\%$)[36]. However, the operating speed in the experiments was limited to a maximum of 40 m s^{-1} . This wind tunnel has the capability of changing its floor; using this feature, and a ground plane was installed on the floor of the tunnel to perform the measurements for the ground vortex in crosswind configurations. The intake model was supported by two ring mounts, which themselves are attached to variable height strut extension. This helped in varying the ground clearance of the model as per requirement. For this project, the ground clearance (h_l) is kept at a constant of 0.083 times the lip diameter (D_l), as shown in Fig. 3.4. The variable height strut is connected to the tunnel mounting plate, which can be rotated through 360° in steps of approximately 1° . For the crosswind conditions, the mounting plated was rotated ninety degrees from the flow direction.

3.5 Measurement Techniques

The objective of this experiment was to measure the unsteadiness of the ground vortex and the distortion caused by it in the intake. Hence, two main parameters were of interest when the experiment was performed: (a) the total pressure on the AIP plane to understand the effect of distortion on intake and (b) the velocity on the PIV plane (see Fig. 3.4) to study about the ground vortex.

The measurement techniques used in the experiment are explained here briefly; Murphy's PhD presents more detailed information. [5].

3.5.1 Pressure Measurement

For total pressure measurement, the intake is equipped with four stationary rakes with nine probes on each rake, as shown in Fig. 3.2. Each probe has a head diameter of 1.5 mm which is 1.25% of the lip diameter. This rake is placed, so the probe inlets are aligned in a single plane to coincide with the equivalent fan face location. That is at a distance of $0.7D_l$ from the lip of the intake in the $y - z$ plane. This plane will be often referred to as AIP. The entire assembly is rotated along the centerline axis of the intake to sample additional data inside the intake circumferentially. As mentioned before, there is no hub or a fan, as the flow is driven by a vacuum chamber.

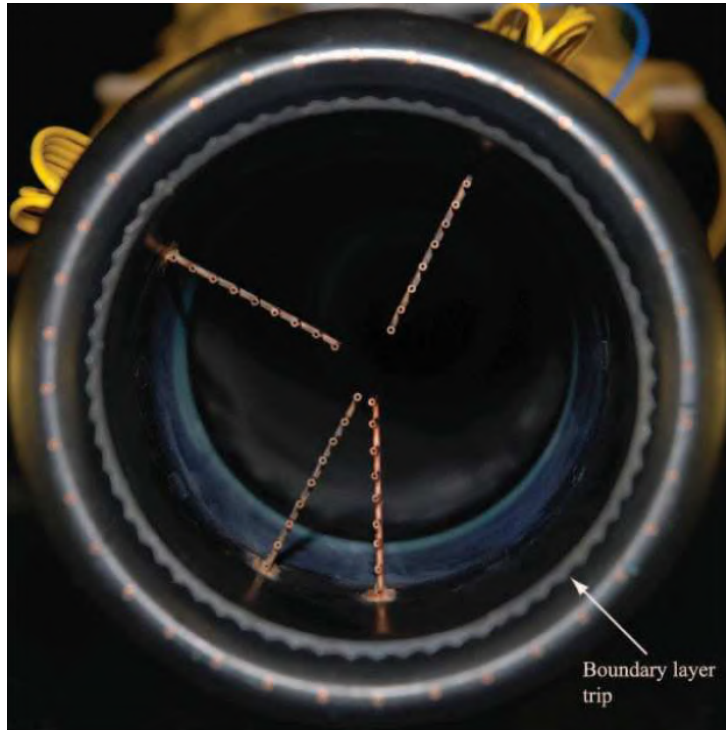


Figure 3.2: Front view picture of intake model, with the total pressure rakes installed.[5]

The total pressure was recorded at 342 locations inside the intake during the crosswind conditions. In Fig. 3.3, the total pressure probe locations are mentioned using the black dots. 36 equispaced static pressure ports were also positioned inside the intake at an axial distance of $0.65D_l$ in line with the AIP. The static pressure probe is shown using red dots in Fig. 3.3. All these pressure ports are connected to differential pressure transducers with a range of ± 5 psi.

For the experiments, an acquisition time of 5 seconds was used with a sampling frequency of 600 Hz. Therefore, the total pressure data is an average 3000 sample collected over a short span of 5 seconds.

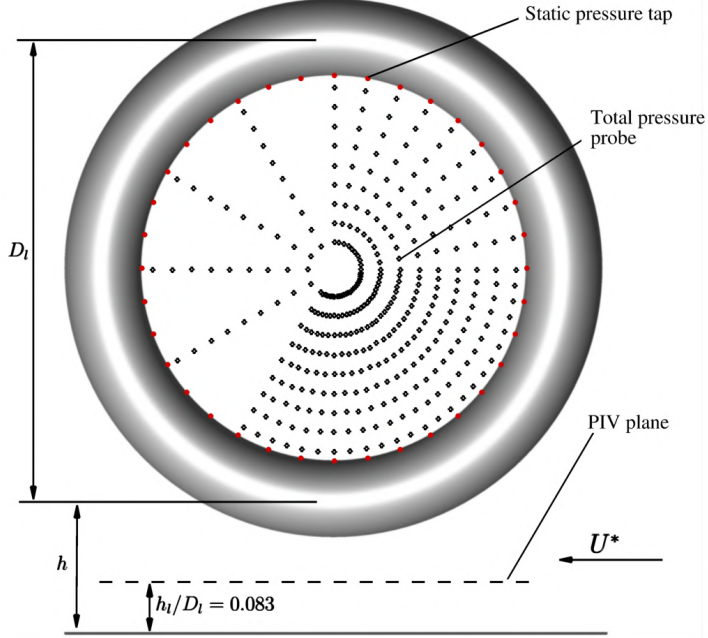


Figure 3.3: Total pressure measurement point within the intake duct for crosswind conditions ($h/D_l = 0.25$)

3.5.2 Velocity Measurement

Stereoscopic Particle Image Velocimetry (SPIV) is used to measure the three components of velocity (u, v, w) in the plane of interest. It is a non-intrusive, global flowfield, optical, quantitative flow visualization technique, and it is widely used in fluid dynamics research [37]. A TSI spectroscopic PIV system was used to acquire the three components of velocity on a plane. This PIV system used two four-mega pixel cameras with 60 mm focal length positioned under the wind tunnel floor. They were arranged at $\pm 45^\circ$ to the measurement plane. A high-powered double pulsed laser with a wavelength of 532 nm and pulse energy of 120 mJ was used. The details about the cameras and laser positioning for SPIV are found in Murphy [5]. For all the experiments performed, a light sheet was placed in a plane parallel to the ground ($x - y$ plane) at the height of h_l as seen in Fig. 3.4, and all the velocity components were extracted on this plane.

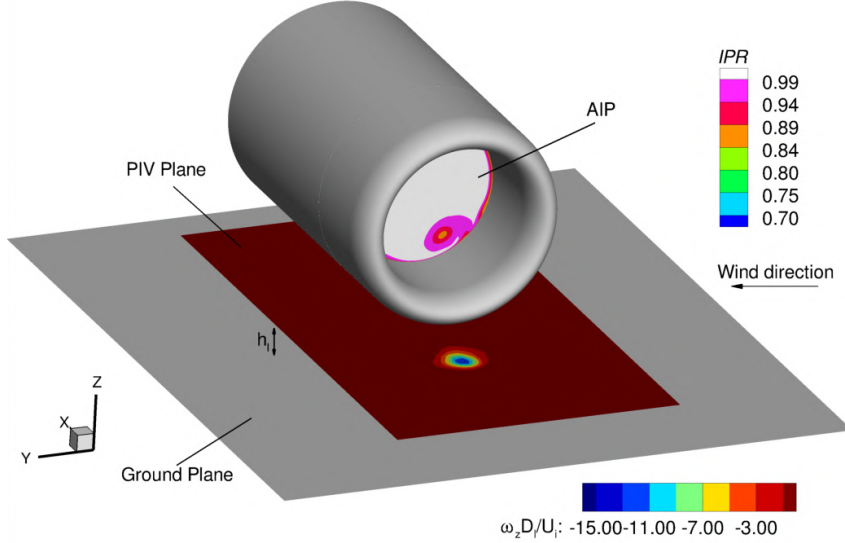


Figure 3.4: Measurement planes used in the experiments ($h_l = 0.083D_l$)

3.6 Testing conditions

The presence of crosswind makes the intake more susceptible to lip separation, and the interaction of this separation with the ingested ground vortex could have severe effects. The experiment was performed at a range of crosswind airspeeds aiming to determine the effect of ground vortex ingestion caused on the intake. However, the experiment data is only available at three operating conditions tabulated in Tab. 3.1 from the AIAA workshop [34], [38]. These inlet conditions are derived from the inlet static and total pressure measurements assuming constant temperature. Under these conditions, the intake Reynolds number ranged between $0.3 - 1.26 \times 10^6$ based on the intake model. Due to the low Reynolds number, strips were placed inside (Fig. 3.2) and outside of the intake lip to promote transition and avoid premature laminar separation.

Table 3.1: Crosswind Operating Conditions of intake at $h/D_l = 0.25$

Case	P_∞ , Pa	T_∞ , K	U_∞ , m/s	U^* , -	\dot{m}_i , kg/s
1	100882.7	290	9.917	18.339	1.46
2	100910.5	290	20.004	9.095	1.46
3	100994.6	290	35.458	5.249	1.46

3.7 Experiment results

For all the three working conditions listed in Tab. 3.1, total pressure and static pressure measurement were provided on the AIP in the AIAA workshop [34]. Using this data, the IPR distributions across the AIP for individual test case are *recreated* and are presented in Fig. 3.5 for low ($U^* = 18.3$), medium ($U^* = 9.1$), and high ($U^* = 5.2$) crosswind velocities.

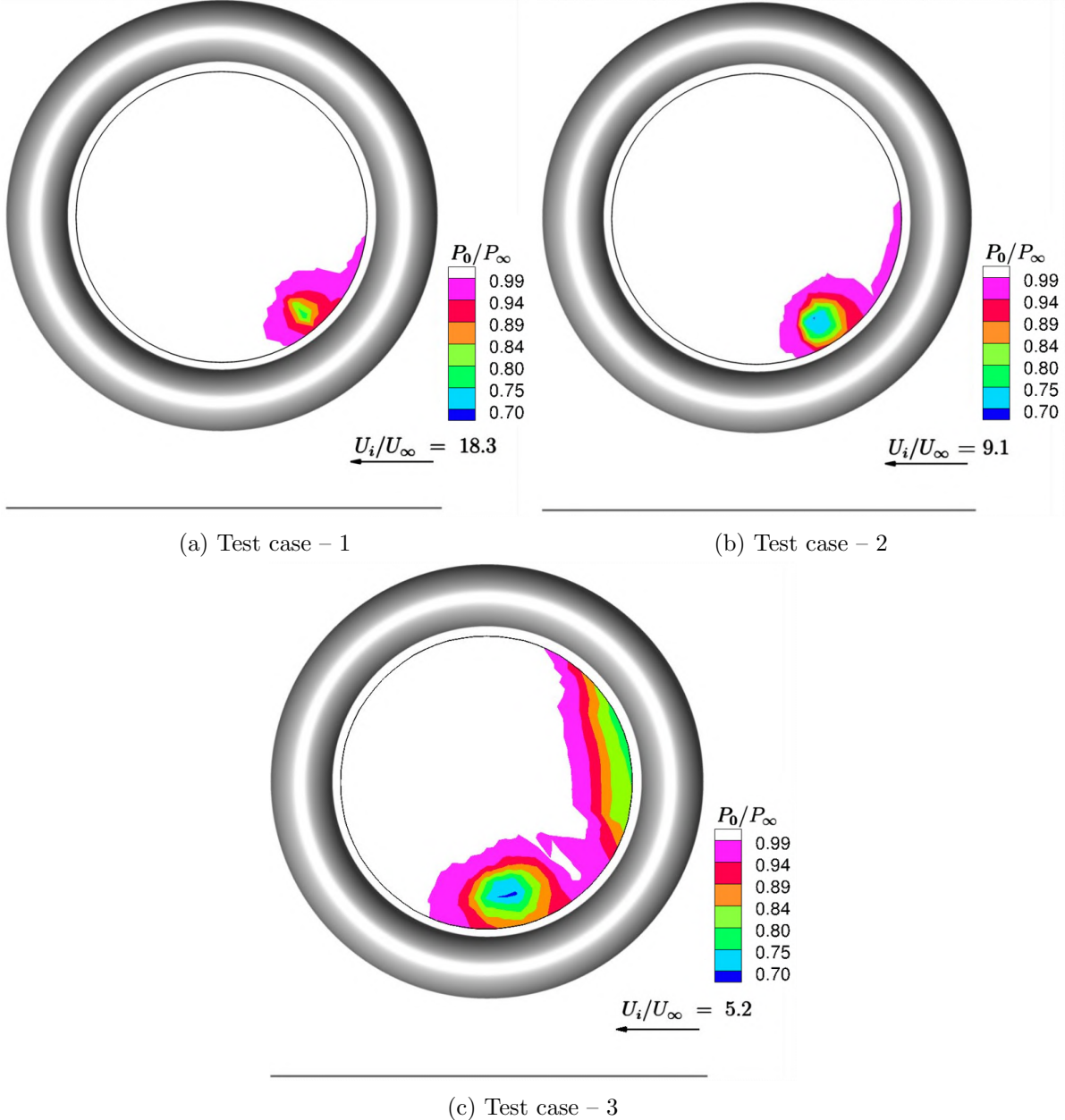


Figure 3.5: Total pressure contours at the AIP for increasing crosswind speed (images recreated from the data provided in AIAA Workshop [34])

The wind is coming from the right-hand side onto the intake, which is placed at a constant height (h_l) from the ground. Due to the ingested ground vortex, one can see a total pressure

loss in the contours presented in Fig. 3.5 on the windward side of the intake. The white region in the figure corresponds to no pressure loss. For the lowest crosswind case, it can be seen that there is an ingested vortex at the 4 O'clock position, which is indicated by a total pressure loss created in that region. For the medium crosswind case, the position of the vortex did not change a lot, but the vortex core became stronger, indicating the increase in total pressure loss. Finally, the total pressure loss increased further for the high crosswind condition, and the vortex moved close to the 6 O'clock position. Therefore, as the crosswind speed increases, the total pressure loss also increases. Furthermore, for the case-3, there is flow separation observed on the AIP at the 3 O'clock position. This flow separation could interact with the vortex, thereby increasing the unsteadiness of the vortex, pushing it away from the windward side.

Under these testing conditions, it was also observed that the boundary layer in the experiments was found to be replicated by the Eq. 3.5, with an average δ of 0.104 m and n of 8.28. Therefore, the ground plane boundary layer profile would be Eq. 3.6.

$$\frac{y}{\delta} = \left(\frac{u(y)}{U_\infty} \right)^n \quad (3.5)$$

$$u(y) = U_\infty \left(\frac{y}{0.104} \right)^{\frac{1}{8.28}} \quad (3.6)$$

AIAA recommended to use this profile in the numerical simulations since the ground boundary layer can play an important role in the formation of the inlet vortex.

3.8 Summary of AIAA PAW-05 results

Following the 5th Propulsion and Aerodynamics workshop (PAW-05) in November 2020, several researchers started investigating the axisymmetric intake used by Murphy [5] in his studies, using a variety of numerical modelling techniques starting from RANS up to high-fidelity methods like very large eddy simulations (VLES) [39, 40, 41, 42, 43] for three particular operating conditions provided in PAW-05 workshop [34]. The three conditions are at a U^* of 18.3, 9.1 and 5.25 for a constant h/D_l of 0.25 above ground. Broadly, the physics of the inlet vortex ingestion predicted by all these investigators match well with the experiment results. But, the accuracy of the results was highly dependent on the type of numerical model, grid density and the software used. A huge inconsistency was observed in the distortion descriptor, DC_{60} , for the three conditions, with a general trend of increasing with a decrease in U^* . For the smallest crosswind case ($U^*=18.3$), the flow was observed to be steady by Selvanayagam *et al.* [39]. As the U^* decreases, the vortex becomes unstable due to the oscillatory behaviour of the ground

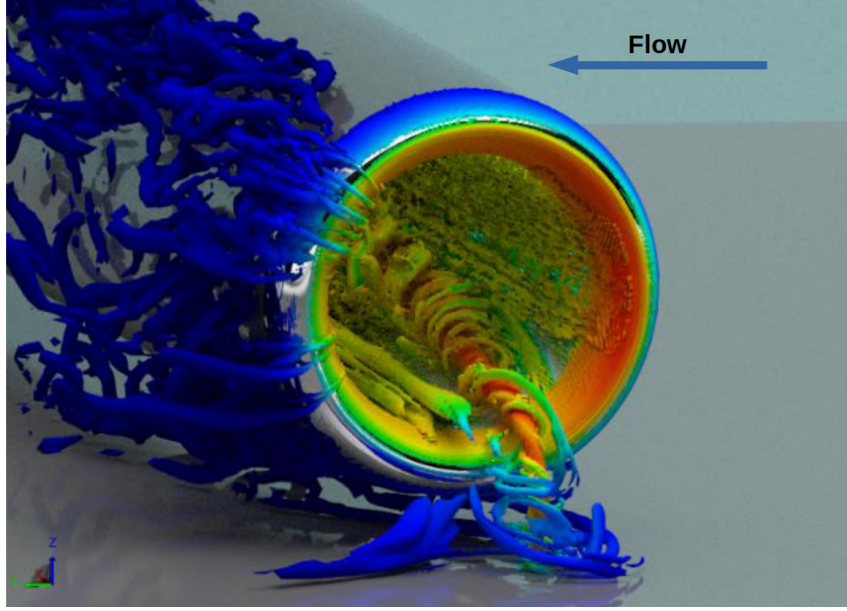


Figure 3.6: Instantaneous isosurfaces of velocity magnitude of Case–1 using VLES by Ribeiro [40].

vortex for the other two cases. Furthermore, for U^* of 5.25, lip separation on the windward side of the intake is observed, leading to an increase in distortion on AIP alongside an increase in the size and unsteadiness of the vortex compared to low crosswind speed conditions.

Ribeiro [40] used VLES and found good agreement with the experimental data for the vortex locations and the total pressure plots across the AIP concerning the PIV data from the experimental studies. Figure 3.6 depicts the path traced by the ground vortex as it enters the intake by the velocity isosurfaces and some secondary vortical structures around the ground vortex like a spiral. Though the results from his work exhibit a very good match, the eddy level calculation used by VLES is computationally expensive.

Potturi *et al.* [42] achieved grid convergence between 128 million and 414 million cells for the lowest crosswind, implying that grid convergence for this problem is not easily achievable. He also studied the effects of four different turbulent models in CFD++ and concluded that $k - \epsilon$, SARC-QCR, and Hellsten realisable $k - \epsilon$ models predicted good results while Menter's SST couldn't predict the behaviour well for low and medium crosswind speeds. However, none of the turbulence models predicted the presence of ground vortex for high crosswind case of $U^* = 5.25$.

Harjes *et al.* [44] performed a methods assessment of an aero-engine intake in crosswinds, and they quantified the impact of the Reynolds number and turbulence modelling approach for a realistic geometry. Hysteresis was observed in their RANS simulations when the intake mass flow was increased or decreased, resulting in different topologies; one had an intake flow

separation on the windward side while the other had a homogeneous intake flow. The impact of the incoming boundary layer was studied in a wind tunnel by Mouton [45]. He found out that the intake operation range is increased when the higher turbulence intensity is generated by the uniform grid. While the crosswind velocities and the movement of the ingested vortex change a lot when an atmospheric boundary layer is generated in the wind tunnel. Therefore, the incoming velocity profile can alter the flow dynamics of an aero-engine.

Babcock *et al.* [43] summarises the PAW-05 workshop by mentioning some very important conclusions. He acknowledged that the accurate prediction of the ingestion of inlet ground vortex is a very complex task, but CFD has proven to be a very useful tool in studying this kind of flow. This successful workshop with a total of 12 participants involved more than 200 individual runs using 9 different solvers, and different meshes and turbulence models tended to predict the smoother features of the vortex and the separation region. The CFD's lower crosswind case was less challenging than the higher crosswind flows. Furthermore, Babcock *et al.* stated that the two-equation turbulence models tended to perform better than one-equation models in predicting DC_{60} , though neither of the models accurately captured the depth of the total pressure loss. Unsteady results did not benefit any better results, despite the inherent unsteadiness in the flow. Finally, he suggested that the initial studies focus on the lower velocity conditions to avoid the added complexity of the vortex and separation flow interaction.

Chapter 4

Computational Methodology

4.1 Aerodynamic Flow Solver

The flow solution is numerically computed using the in-house code HADES[®], which is a 3D time-accurate, compressible, viscous, finite volume, hybrid RANS/LES flow solver for unstructured meshes. The flow variables are represented on the nodes of a generic mesh, and the numerical fluxes are computed along the edges of the grid. The Solver is based on the one-equation Spallart-Allmaras turbulence model [46]. At viscous wall boundaries standard wall function Pope [47] is used. The overall solution method is implicit, with second-order accuracy in space and time. It has to be noted that in this work, the compressible solver is employed.

For steady-state flow computations, the solution is advanced in pseudo-time using local time stepping and solution acceleration techniques; dual time stepping is used for time-accurate unsteady computations. Unsteady flow computations can be computed using unsteady Reynolds-averaged Navier-Stokes (URANS) equations. Validation and verification of HADES[®] in various 2D canonical flows and high-speed 3D compressible applications can be found in past publications by He *et al.* [48],[49]

4.2 Computational Domain

The geometry chosen for this study is the simplified intake proposed at the 5th PAW by AIAA [34]. For the CFD simulations, the intake geometry was placed inside a computational domain of length $25D_l$, width $25D_l$ and height of $12.5D_l$ as shown in Fig. 4.1. The intake is placed $0.25D_l$ above the ground plane and is $7D_l$ long, extending downstream to improve the numerical stability of the model. The centre-line cross-section of the intake along the $x - z$ plane is equidistant from both the inlet and the outlet wall ($12.5D_l$ from either wall). As shown in

Fig. 4.1, the intake exit extends all the way to the end of the domain, maintaining a clear distinction from the domain back-wall. This acts as a different surface to help generate an independent flow inside the intake irrespective of the domain walls.

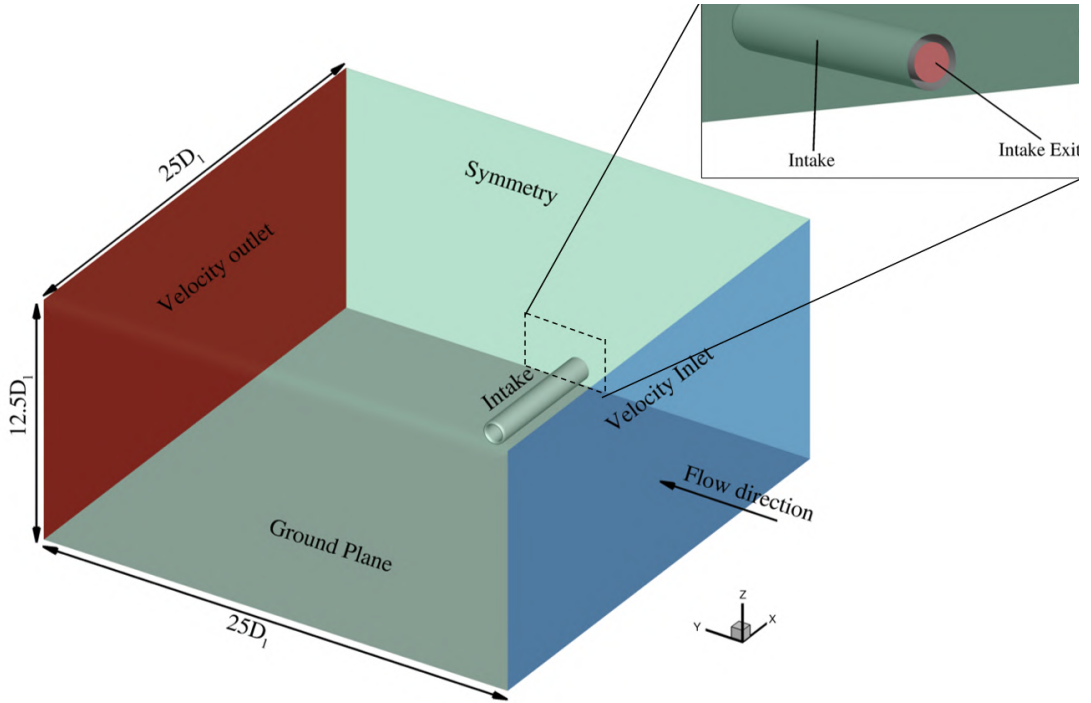


Figure 4.1: Computational domain used for simulations

4.3 Grid and boundary conditions

The mesh used for simulations in this thesis is obtained from Cranfield university. To access the influence of the mesh size on the results, three grids were generated using the computation domain shown in Fig. 4.1. The three grids are labelled coarse, medium and fine mesh with 7.1, 17.2 and 41.1 million elements, respectively. Structured multi-block grids were generated with multiple inflation layers using hexahedral cells. To capture the viscous effects near the wall, the nearest layer to the wall is at a non-dimensional distance of $y^+ \approx 1$ for all the grids. These small values of y^+ will also help accurately resolve the boundary layer near the ground plane and around the intake surface.

The boundary conditions used for the initial computations are tabulated in Tab. 4.1. In the next section, several studies are performed to optimise the conditions and arrive at the best approach to set up the computational domain for crosswind conditions. The velocity at the inlet was computed based on the preferred U^* . The flow inside the intake is regulated by changing the boundary conditions at the intake exit (seen in Fig. 4.1). For all the simulations in this

Table 4.1: Initial boundary condition used for the simulations

Domain	Boundary Conditions
Inlet Boundary	Velocity Inlet
Inlet Velocity Profile	None
Outlet Boundary	Velocity Outlet
Intake wall	No-slip
Ground plane	No-slip
Side walls	Symmetry
Intake Outlet	Mass Flow Outlet

report, the mass flow at the intake exit is set to a constant value of 1.46 kg s^{-1} . The ground plane and all the walls are set to no-slip boundary conditions, while all the remaining domain wall boundaries are defined as symmetrical.

4.4 Setup optimisation

4.4.1 Impact of inlet velocity profile

In this section, a small study is performed on the coarse mesh to understand the importance of providing an inlet velocity profile for this problem. The experiment is performed in a wind tunnel with a long duct section upstream to the intake, a boundary layer could develop. Since the long duct is not included in the domain, a boundary layer has to be provided at the domain inlet. Initially a uniform velocity profile ($U/U_\infty = 1$) was used at the inlet. By default, in any numerical software, there will be a BL profile corresponding to a no-slip boundary condition. In HADES®, the velocity in the BL develops to its free stream velocity very close to the ground, as seen as Uniform profile in Fig. 4.2. It is compared with the BL profile extracted from the experiments (Eq. 3.6), and it is clear that the BL from the experiments develops much farther from the ground than the default HADES BL profile. In this study, the intake is placed close to the ground; therefore, the experiment BL profile covers almost half the height of intake.

No major changes were observed for the low and medium cases during RANS simulations. For high crosswind speed as seen in Fig. 4.3, with the imposed BL profile, the mean Navier-Stokes residuals doesn't converge while for the case with uniform BL profile, the residuals converges. This implies that there is presence of unsteadiness in the former case.

Figure 4.4 compares the experimental results with the numerical results using uniform and imposed BL profile. From qualitative visualisation, one can say that for the lowest crosswind

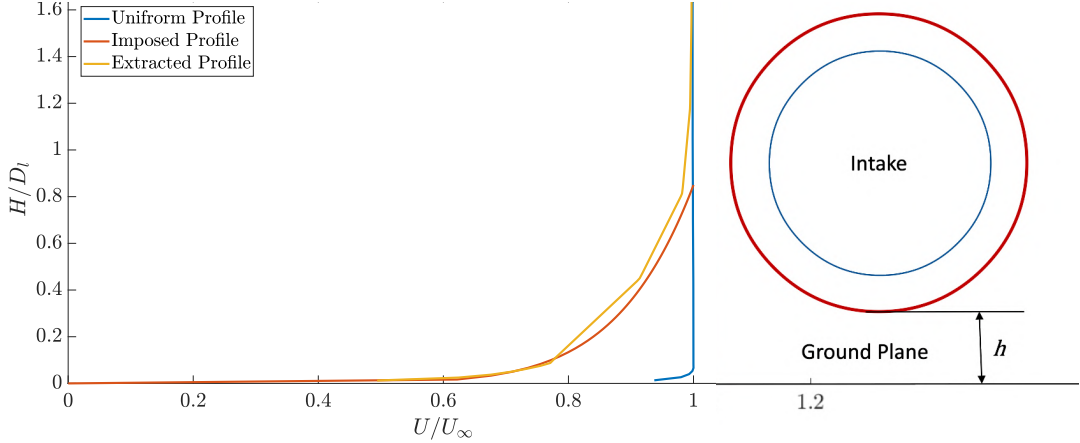


Figure 4.2: Comparison of inlet BL for Uniform and imposed profile at $25D_l/3$ from intake centreline.

speed, the BL profile has no effect on the location of the vortex but has a better total pressure prediction. The same effect is seen for the medium crosswind speed with almost no change in the position of the vortex but a slight decrease in the total pressure loss. However, for the high crosswind with uniform intake profile condition, the vortex and the separation did not appear, contradicting the experimental results. But, for the case with imposed intake BL profile, the vortex is present while the separation is still not seen at $U^* = 5.2$. Since the flow develops fully very close to the ground in the case of uniform intake BL profile, the vortex could have been blown away by the high crosswind very close to the ground. While for the other case, the wind speed inside the BL ($< U_\infty$) is not strong enough to blow the vortex away from the ground plane in front of the intake. Therefore, the influence of the vortex is still clearly visible at the AIP in terms of pressure loss. The presence of the vortex in the latter case is the unsteadiness that is responsible for the residuals not being converged for this case.

The phenomenon mentioned above can be supported by normalised vorticity contours in Fig. 4.5 a,b. it is clear that for the case with uniform inlet profile, the vortex on the ground is not present and is blown away by the strong crosswinds (U^*). The vorticity levels (pink contour) present in Fig. 4.5a could be misunderstood for a vortex, but the out-of-plane velocity flow field presented in Fig. 4.5 c denies its presence. However, in the case of the intake profile, the vortex is very strong (compared to the former case), and it is right in front of the intake on the ground plane affecting the flow inside the intake. This can also be verified by Fig. 4.5 d, where one can see a higher w velocity component in the location of the vortex.

Due to the fully developed velocities close to the ground, the vortex estimated could be stronger for the first two cases with uniform BL profile; the solver predicted a better total pressure contour on AIP. This is not a better prediction of the current condition; instead, it is equivalent

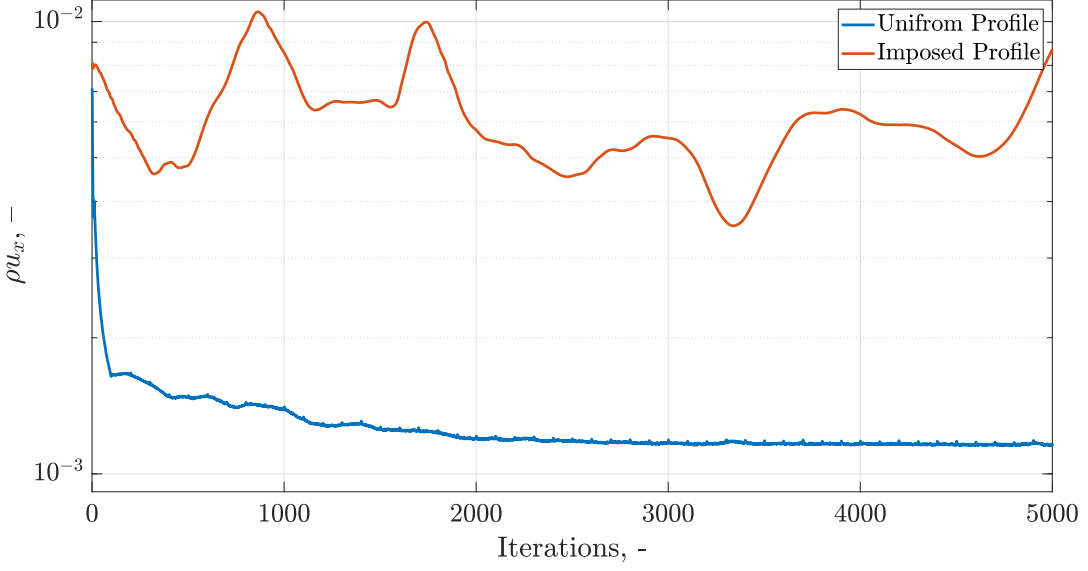


Figure 4.3: Mean Navier-Stokes residual of ρu_x for high crosswind with uniform and imposed BL profile at inlet.

to a condition with higher H/D . The uniform boundary layer setup fails to predict the presence of the vortex entirely for the high crosswind case. In contrast, the setup with the intake boundary layer predicted the existence of the vortex in the intake. So, from this study, one can see the significance of the intake BL profile in this problem. Henceforth, all the simulations performed in this report use a standard boundary layer profile shown in Eq. 3.6.

4.4.2 Turbulence model

The turbulence model plays a vital role in RANS modelling. Since SA is a one equation model, it might not be capable enough to pick up the severe unsteady effects of ground vortex ingestion. Over the years, several approaches (flavours) have been studied to address this complicated fluid flow to increase the SA turbulence model's prediction capabilities. Considering that HADES only offers Spalart–Allmaras (SA) turbulence model, few of these flavours were employed in this case, and the results are studied in this section to find the best turbulence model for this problem.

The SA turbulence model is a linear eddy viscosity model based on Boussinesq assumption [50]. The standard linear eddy viscosity model may fail to predict the rotation effects accurately or may not be able to predict at all [51]. Due to the presence of a rotating vortex in this problem, the standard SA model might not be able to predict the effects properly. Therefore an 'RC' flavour of the standard SA model [52] is studied for this problem. The term 'RC' stands for system rotation and streamline curvature inherent in this case. So, for sensitisation of the SA

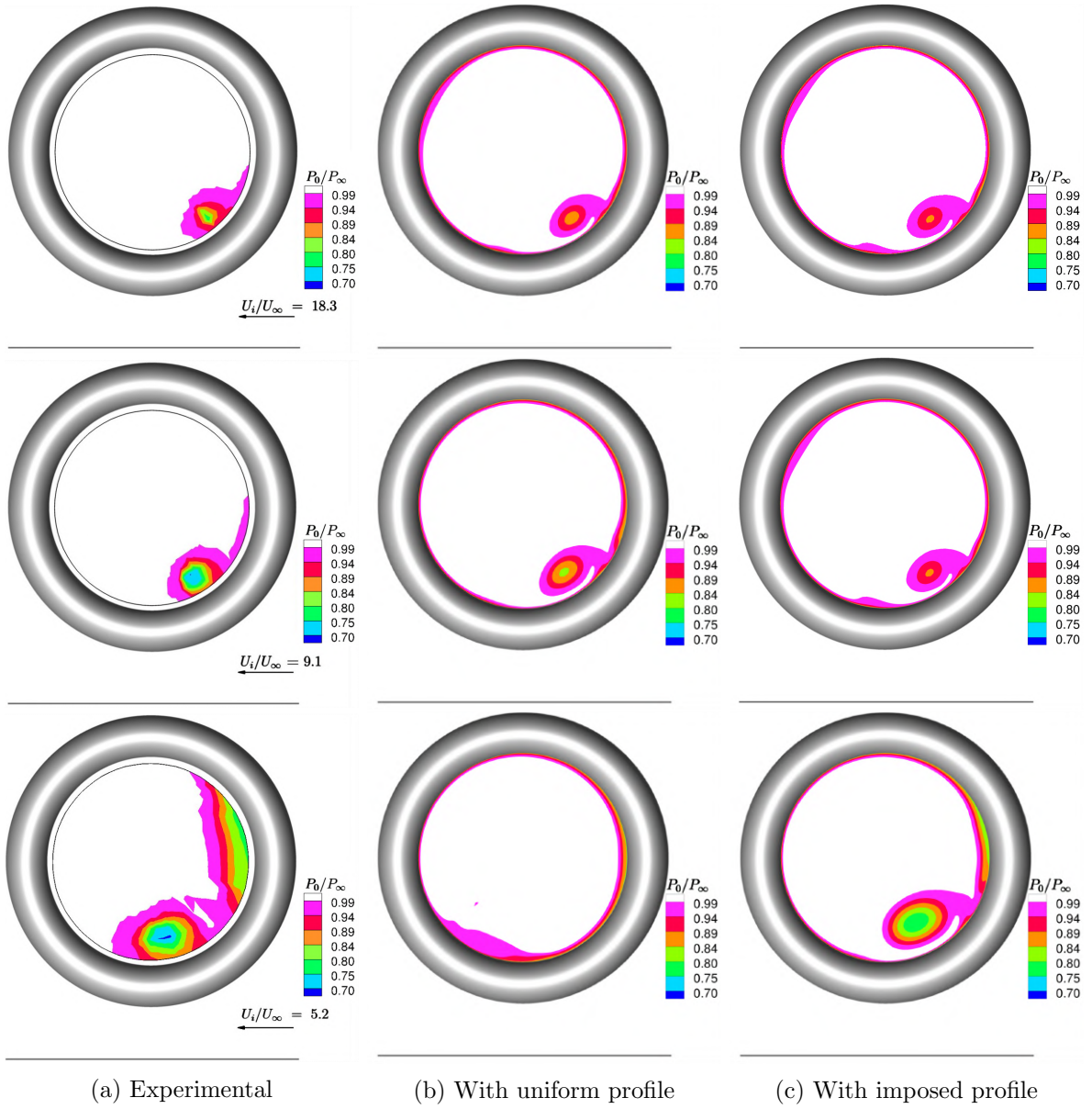


Figure 4.4: Comparison of IPR contours for with uniform and imposed BL profile with increasing U^* (Experimental (recreated from [34],[5]) on left and Numerical on centre and right)

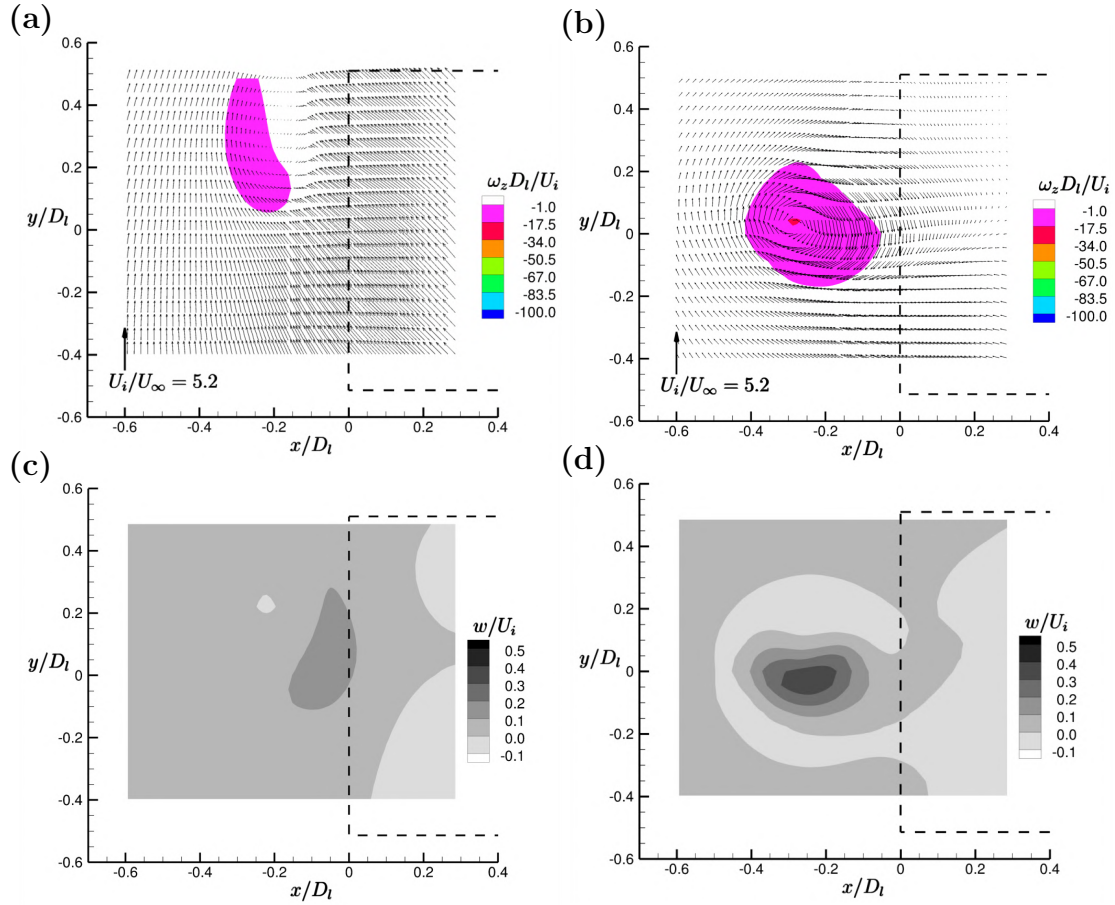


Figure 4.5: The vortex-aligned average vector flow-field (a,b) with contours of normalised vorticity and (c,d) out-of-plane velocity flow-field for cases with uniform (left) and imposed (right) intake BL profile at $U^* = 5.2$

model to RC effects, a simple rotation function which is a combination of second derivatives of the velocity field, is multiplied by the eddy viscosity transport function [53].

Another highly employed modification with linear eddy viscosity turbulence model is quadratic constitutive relation (QCR) [52]. Implementing this flavour changes the linear SA model non-linear. The missing feature of the Boussinesq eddy-viscosity approximation is to predict the secondary flow of second-kind induced by the anisotropy of the Reynolds-stress tensor. To introduce this anisotropy, nonlinear constitutive relations were used for Reynolds stress without adding additional differential equations. This enhances the capability of linear turbulence models to improve prediction for several kinds of flows [54]. To achieve this, Spalart [55] proposes a simple quadratic constitutive relation (QCR) that can capture the secondary flow of the second kind. Significant qualitative improvement from QCR2000 flavour is seen in other separation flow studies [56]. When used in conjunction with Spalart–Allmaras turbulence model with rotation/curvature correction, this model produced excellent results for separation flow [57]. Since the problem studied in this report has a separation flow, QCR2000 was also considered for this study.

Figure 4.6 represents the use of different flavours of the SA model to predict the separation flow overlooked by the standard SA model. The SA–RC model predicted the separation flow on the windward side, while the QCR2000 model failed to do it. But the combination of both the flavours in Fig. 4.6d predicted a similar result as SA–RC model. However, qualitatively speaking, it is not exactly the same; the SA–RC–QCR2000 model predicted a stronger vortex presence. Considering the success of RC–QCR2000 flavour observed with the separation flows in the past [57], the said model is used for all simulations presented in this report.

4.5 Chapter Summary

In this chapter, the computational domain, mesh and the setup are described in detail. Then from the inlet boundary layer study, it is concluded that the boundary layer plays an important role in the prediction of the ground vortex. Therefore, the BL profile measured in the experiments is considered for the numerical simulations. Finally from the turbulence model study, SA-RC-QCR2000 is considered the best model for the problem studied in this work.

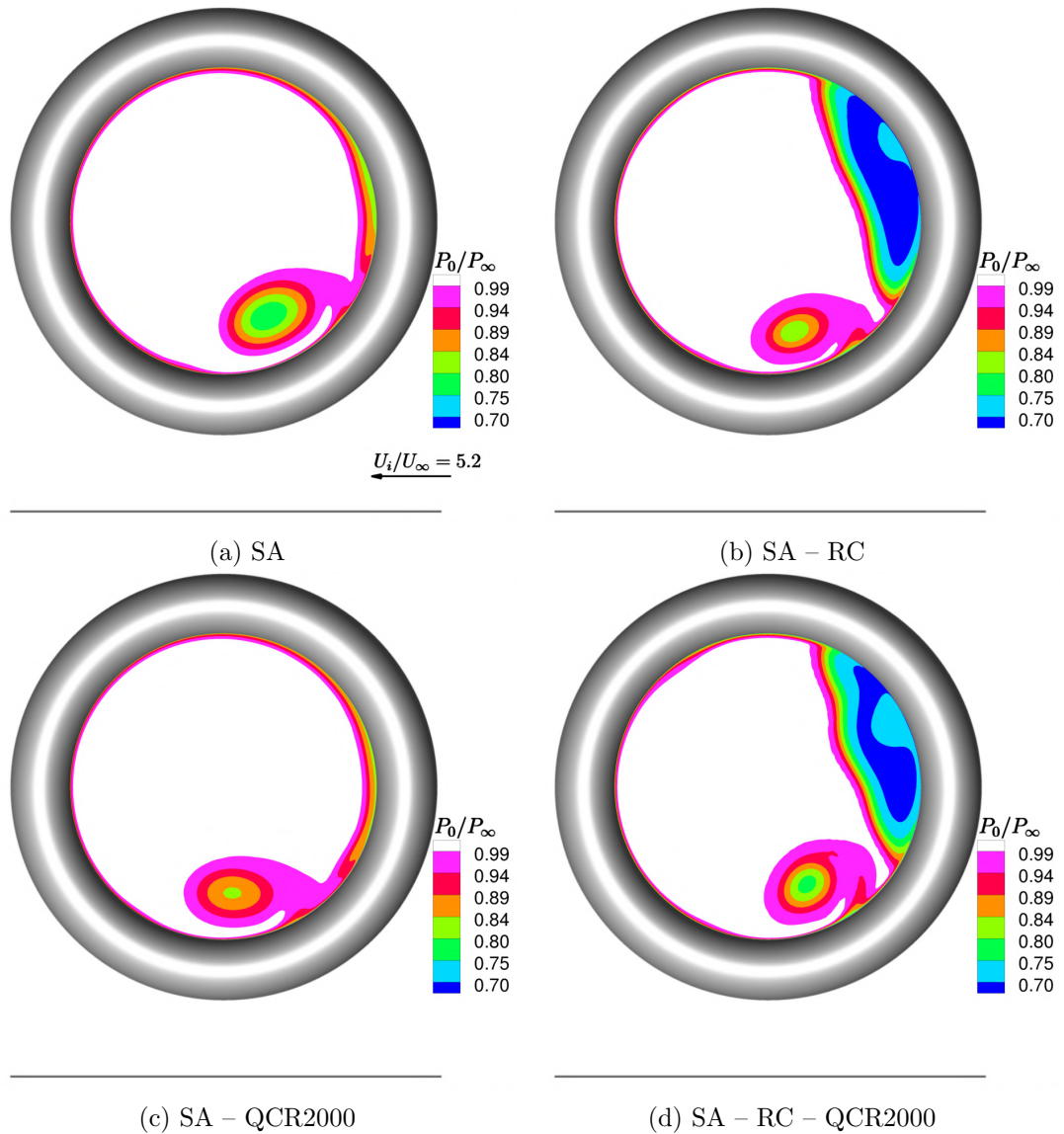


Figure 4.6: IPR contours for different turbulence models at $h/D_l = 0.25$ for $U^* = 5.2$

Chapter 5

Steady state analysis

Steady-state RANS simulations performed with the domain and methodology explained in the previous chapter are analysed and discussed here. These simulations were performed using coarse, medium and fine grids, divided based on their grid densities. A study is performed to see the effects of grid density on the numerical solution, and these results are validated using the experimental test data from AIAA PAW-05 [34].

As we have seen in the literature, two vortices exist, one on the ground and the other trailing from the lip on the leeward side of the intake. Since the ground vortex significantly impacts the total pressure at intake, it is of paramount importance, and the trailing vortex is not studied in this work. The non-dimensional parameters described in § 3.2 are used to provide a valid comparison between the experiment and the numerical data.

5.1 Grid Independence Study

An initial grid sensitivity study was carried out among the three grids to determine the impact of the grid resolution on several phenomena of interest. Mainly the ground vortex properties, intake distortion, and separation at the intake lip. For this purpose, open-source data from the PAW-05 workshop was used, and the IPR plots were recreated. For credible comparison between the numerical and experimental data, the pressure recovery at the intake and pertinent ground vortex vorticity are calculated using the method described by Murphy [5]. The IPR on the AIP plane and the ω_z^* on the PIV plane are compared for the three different grid sizes.

By looking at the initial Navier-stocks mean residual plot using fine mesh for three crosswind cases in Fig. 5.1, it is clear that as the crosswind speed increases, the level of convergence decreases. This implies that the unsteadiness present in the system is also increasing. Therefore it can be considered that the the solution is not converged in steady state.

For case-1, the lowest crosswind case, IPR is shown in Fig. 5.2a-d. The white region in the plot

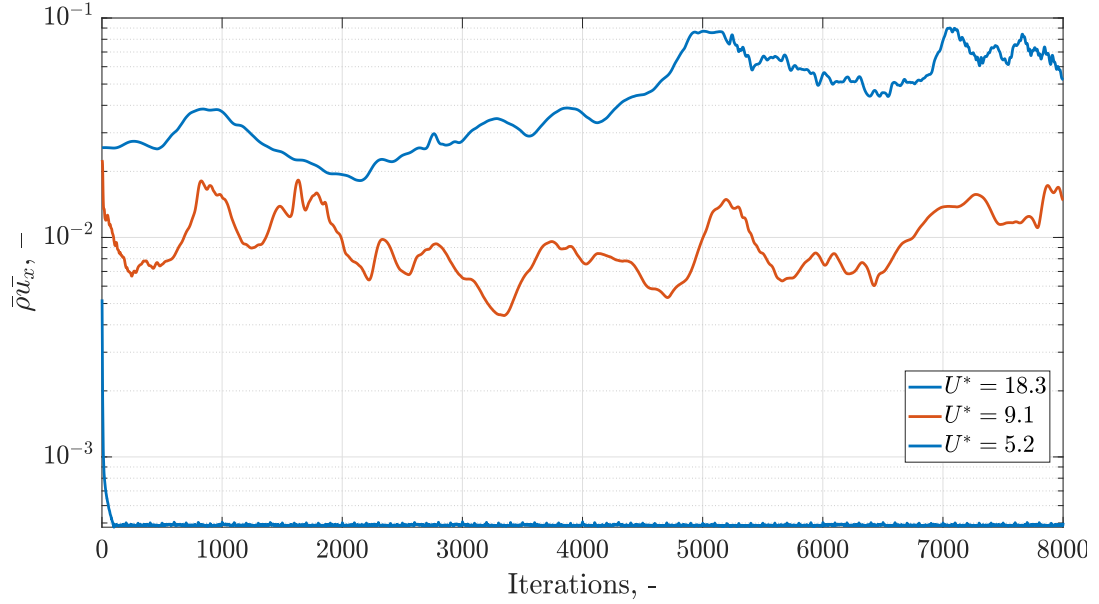


Figure 5.1: Mean Navier-Stokes residual of $\rho \bar{u}_x$ for Low, Medium and High crosswind cases using fine mesh.

is associated with no pressure loss, and qualitatively it is clear that the vortex has an effect on the AIP in the form of a total pressure loss at a 5’O clock position. The numerical prediction of the stagnation pressure is improving with the increase in grid density. The line plot shown in Fig. 5.2e is plotted by probing circumferential at a fixed radial position of highest stagnation pressure loss (essentially the core of distortion). Experimentally, there was a total pressure loss of about 24% which is predicted very closely by the fine mesh (20% loss). Furthermore, it can be seen that the location of the vortex circumferentially is estimated better by the medium mesh and fine mesh with a difference up to 5° from the experiment data (at 230°). Finally, the small total pressure loss (about 3%) at the 11 O’clock position inside the intake is the impact of the trailing vortex on the leeward side.

Fig. 5.3 is the plot of normalised out-of-plane vorticity (ω^*), where the white region (no colour) is linked with the absence of out-of-plane vorticity. The in-plane velocity vectors present a swirling motion around the plot’s pink contour, denoting the ground vortex’s existence on the PIV plane. It can be seen that the appraisal of the vortex intensity is predicted best with fine mesh, which results in higher inlet distortion on AIP, as observed before. However, the different grids predicted no significant change in the vortex core location. Also, the vortex core is at a distance of $0.2D_l$ in the x direction from the intake lip, represented by the dotted line. From these figures, it is clear that the vortex on the ground is present close to the centre-line, slightly towards the windward side and extending almost vertically into the intake.

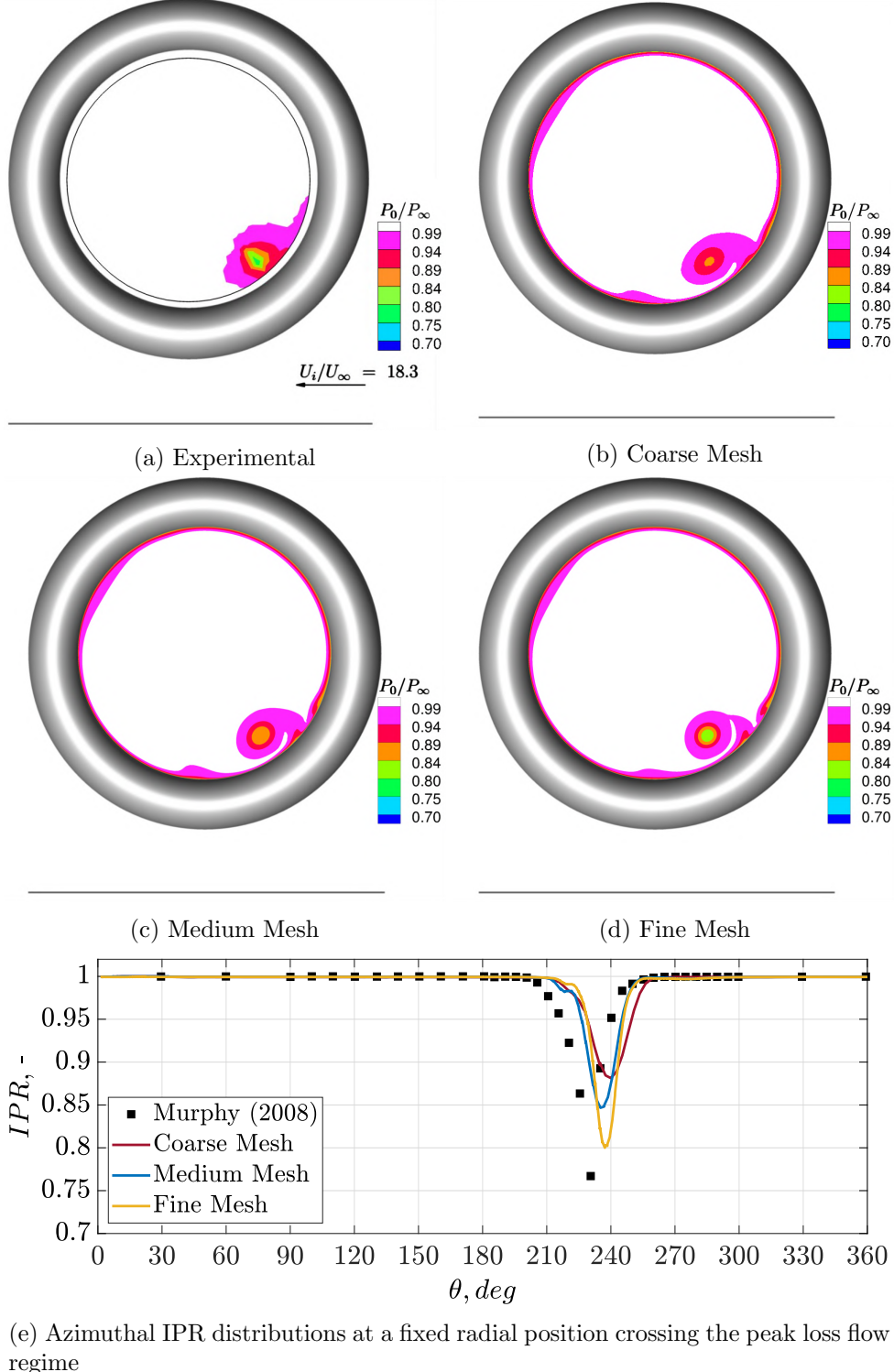


Figure 5.2: IPR contours for a $h/D_l = 0.25$ and $M_i = 0.55$ for $U^* = 18.3$ (Experiment data is recreated from [34])

Finally, the values of Distortion coefficient (DC_{60}) and Γ^* are tabulated in Tab. 5.1. The value of DC_{60} doesn't change much among the three different grids, but it is almost half as much as the experiment value. Here, it has to be noted again that DC_{60} parameter is not highly

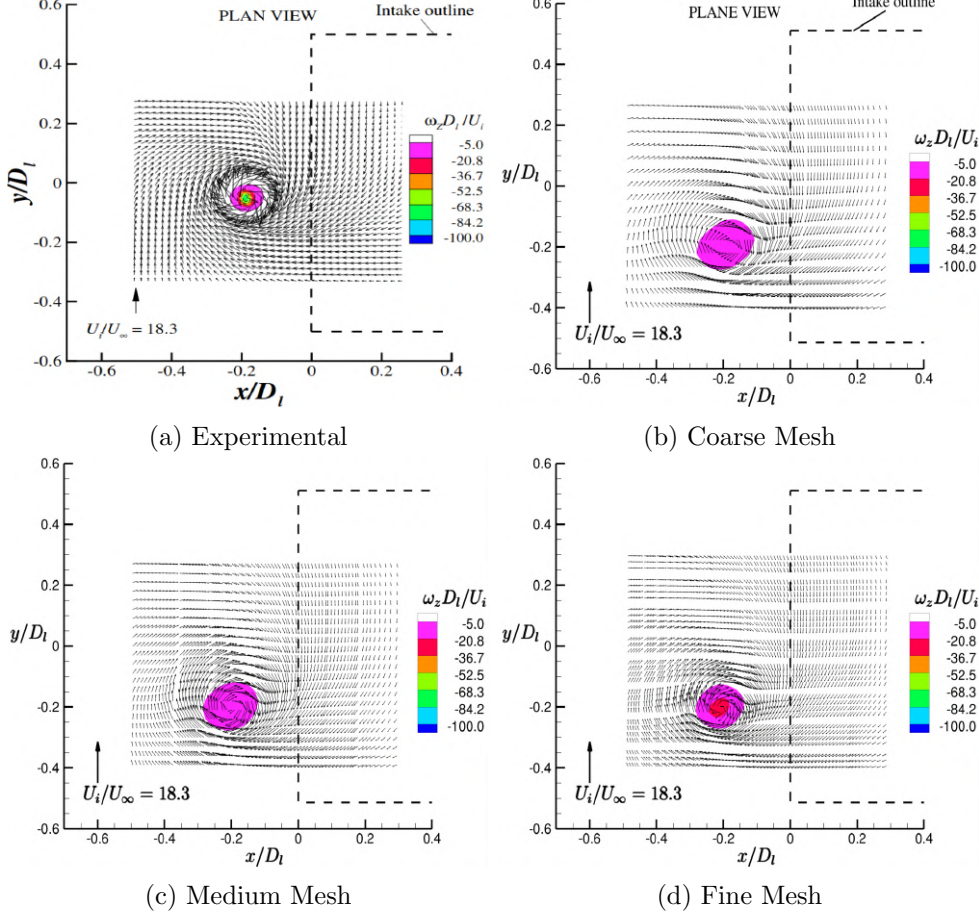


Figure 5.3: $u - v$ vector and vorticity field for a $h/D_l = 0.25$ and $M_i = 0.55$ ((a) is taken from [5])

regarded by the researchers in the field of aerodynamics since it doesn't exactly represent the distortion present in the system, but it is mostly used because a better alternative doesn't exist. The non-dimensional circulation (Γ^*) from the experimental data agrees well with the numerical results.

For Case-2 with medium velocity ratio of 9.1, IPR plots are presented in Fig. 5.4. Firstly, the location of the vortex is changing a lot among the solutions from the three grids. While the coarse mesh has done a very good job predicting the location, the medium and the fine mesh are far from the experiment data. This is evident from Fig. 5.4e. Though the total pressure loss increases with the increase in grid density, the vortex is moving away. For the coarse mesh,

Table 5.1: Non-dimensional parameters for different mesh sizes at $U^* = 18.3$

Parameter	Experimental	Coarse Mesh	Medium Mesh	Fine Mesh
DC_{60}	0.116	0.0575	0.0529	0.0512
Γ^*	0.256	0.3105	0.3017	0.3079

Table 5.2: Non-dimensional parameters for different mesh sizes at $U^* = 9.1$

Parameter	Experimental	Coarse Mesh	Medium Mesh	Fine Mesh
DC_{60}	0.217	0.107	0.119	0.135
Γ^*	0.288	0.209	0.256	0.275

a region of total pressure loss is seen at a 5 'o clock position inside the intake. But for medium and fine mesh, it is almost past the 6 o'clock position. This is attributed to the convergence level of the numerical simulations. The residuals of the Navier-Stokes equation are converged for the coarse mesh, whereas for the medium and fine mesh, they did not. This could mean that the vortex is starting to become unsteady, so the steady state was not able to find a particular solution. Therefore, the solutions presented for medium and fine mesh is not converged. For the coarse mesh, since the mesh density is large, the small unsteadiness must have been numerically dissipated, resulting in a converged solution.

Fig. 5.5 shows the vortex locations on the PIV plane from the top view. Firstly, as expected, the non-dimensional vorticity (ω^*) is better predicted by the fine mesh than the medium and the coarse mesh. Whereas the predicted location of the vortex did not change at all with different grids. The experiment data suggests that the vortex extends from the leeward side of the ground to the windward side of the intake. The vortex from the numerical results extends to different locations inside the intake from one location on PIV. The values of DC_{60} are under-predicted again as in the previous case by almost 50%, with the values being almost constant among the different grid densities. On the flip side, the normalised circulation is predicted to be very close to the experimental results as tabulated in Tab. 5.2.

For Case-3, Fig. 5.7 represents the IPR on the AIP, and an additional phenomenon apart from the distortion is observed on the intake. It is the intake lip separation on the windward side. As the crosswind speed is high, the flow coming into the intake doesn't have contact long enough with the intake wall to enter inside smoothly; therefore, a separation can be seen when the flow enters the intake. This is a very complex case because of the interaction of the separated flow and the ground vortex entering the intake. For this case, the Navier-stokes residuals for neither of the grids were converged as shown in Fig. 5.6. In contradiction to what one might expect, the coarse mesh has performed better in predicting the location and total pressure loss inside the intake than the denser grids. This could be mere coincidence. It can also be seen that the separation is over-predicted compared to the experiments, not just the total pressure loss in the separation region but also the extent of separation. All these observations can be

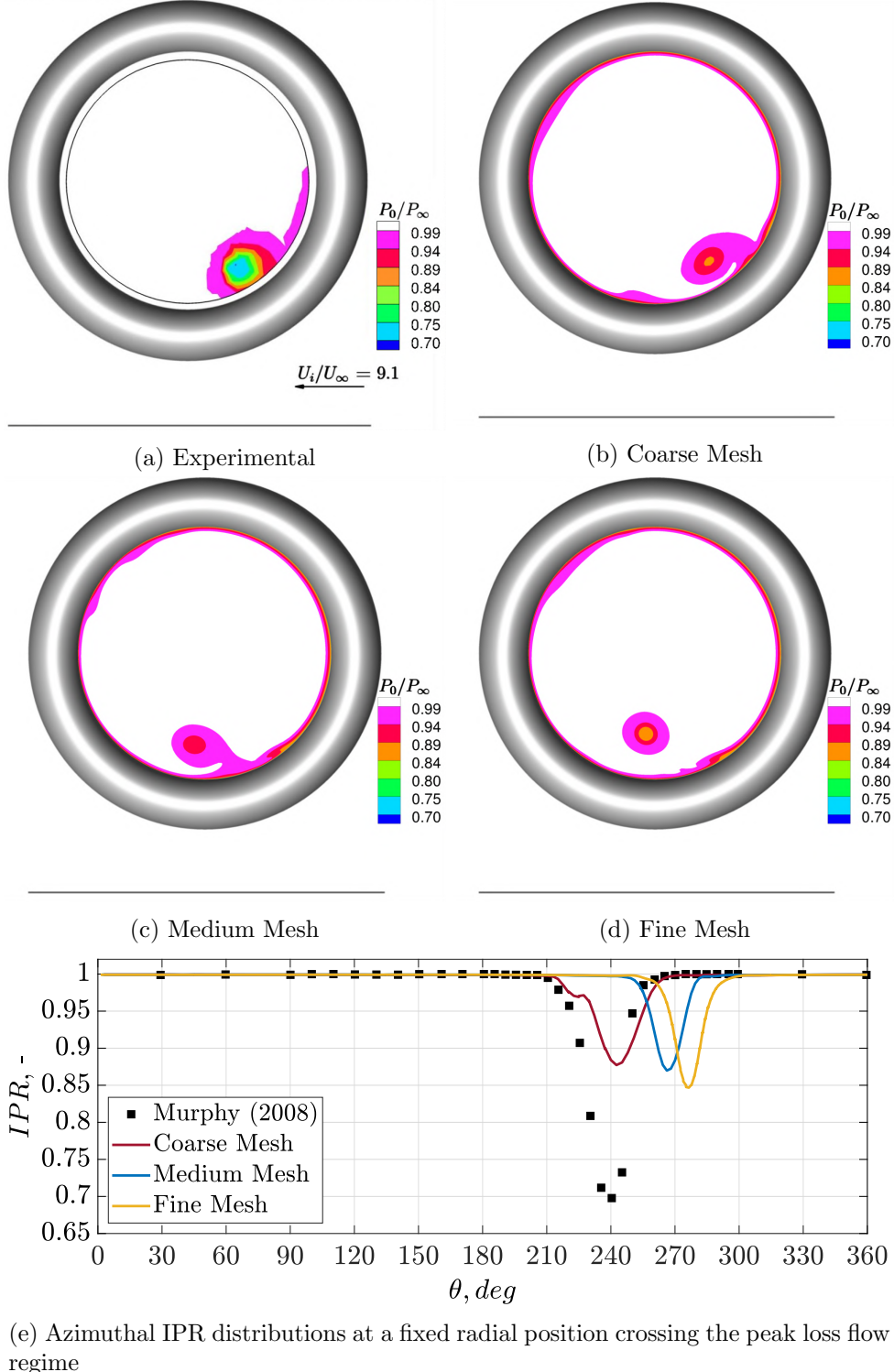


Figure 5.4: IPR contours for a $h/D_l = 0.25$ and $M_i = 0.55$ for $U^* = 9.1$ (Experiment data is recreated from [34])

quantitatively seen in Fig. 5.7e.

From the qualitative comparison of the PIV plane shown in Fig. 5.8, the vortex location was predicted differently by different grids in the steady state simulations. It can also be noted that

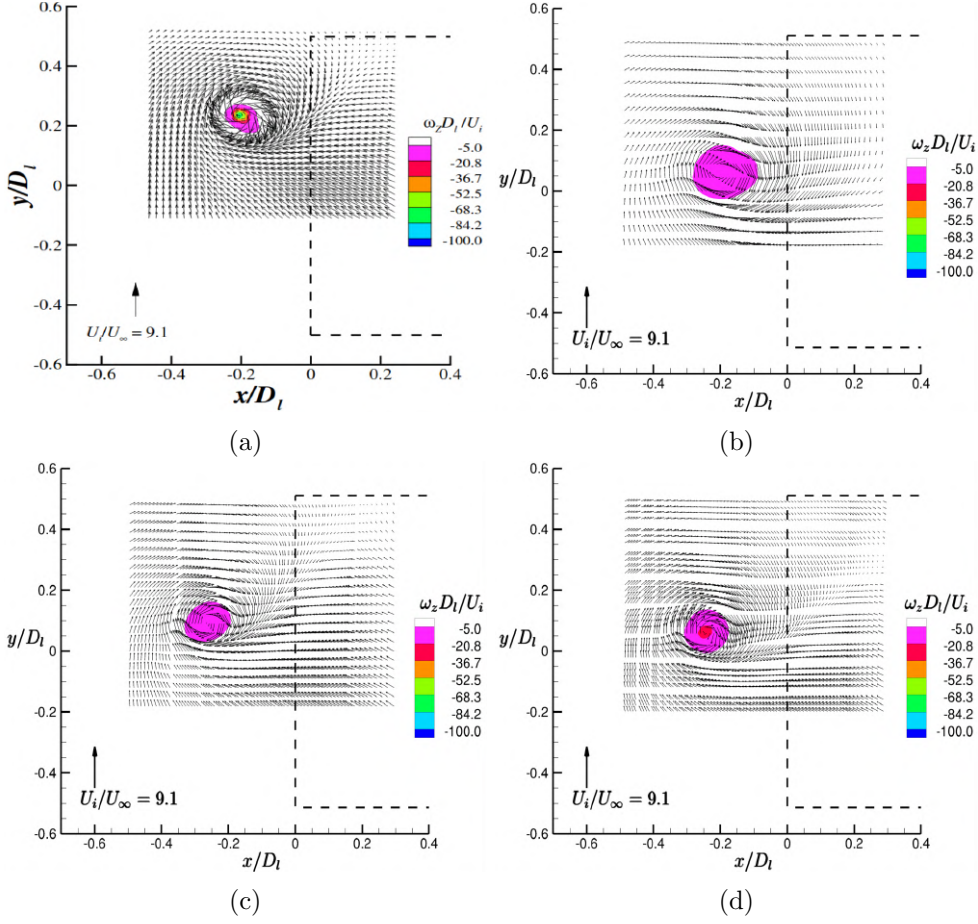


Figure 5.5: $u - v$ vector and vorticity field for a $h/D_l = 0.25$ and $M_i = 0.55$ ((a) is taken from [5])

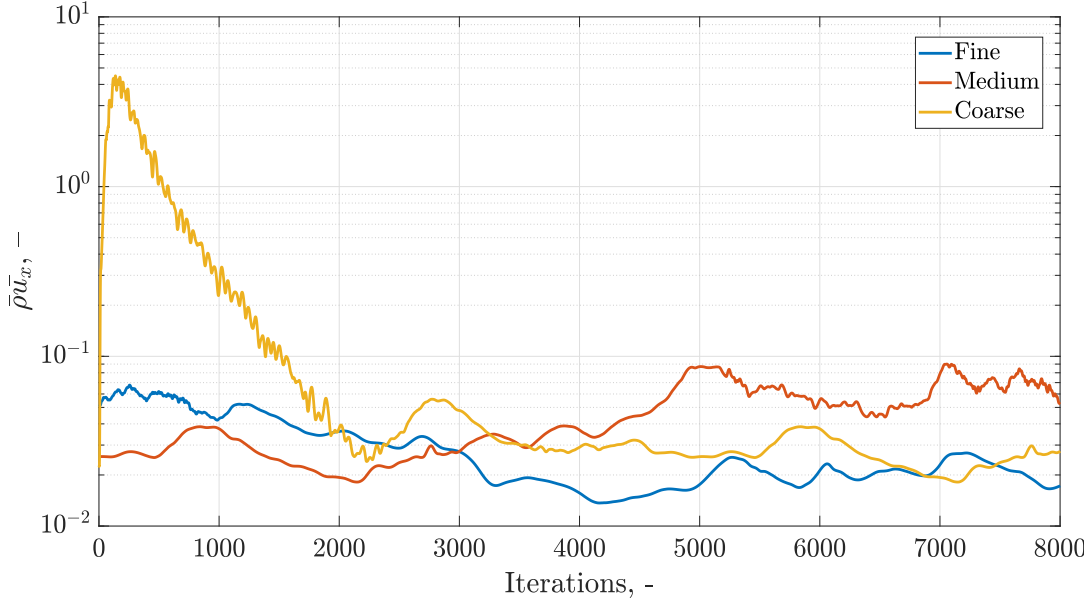


Figure 5.6: Mean Navier-Stokes residual of ρu_x for $U^* = 5.2$.

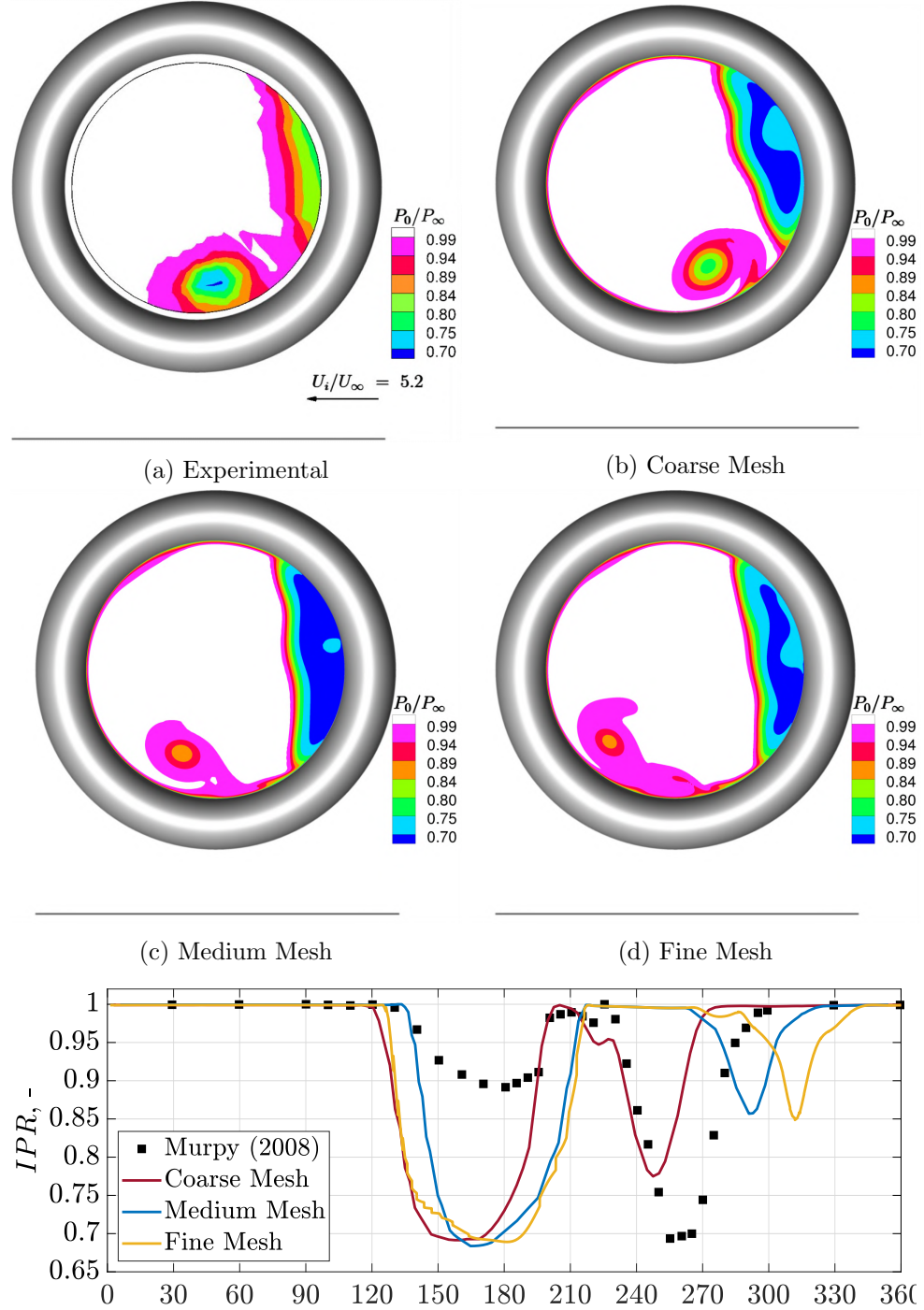


Figure 5.7: IPR contours for a $h/D_l = 0.25$ and $M_i = 0.55$ for $U^* = 5.2$ (Experiment data is recreated from [34])

the location of pressure loss on the AIP is changing with the vortex location on the ground. For the coarse mesh, the vortex on PIV is more central; therefore, the vortex in the intake was towards the windward side. This is completely opposite to the fine grid where the vortex moved

towards the leeward side. Since the experimental data shown here was a snap-shot at a random time instant, one cannot indicate which grid predicted the location better; it could be that the vortex is hovering over all these locations. Therefore, from these results, it is clear that the motion of the vortex has become highly unsteady, and the steady state cannot estimate the phenomenon properly.

The DC_{60} values for this case are tabulated in Tab. 5.3. The coefficients predicted are higher than the experimental data, which differs from the previous cases. This is due to separation; the 60° sector for minimum pressure is considered in the separation zone; therefore, the average total pressure is much less, leading to high DC_{60} values. The non-dimensional circulation values for this case are scattered about the experiment data.

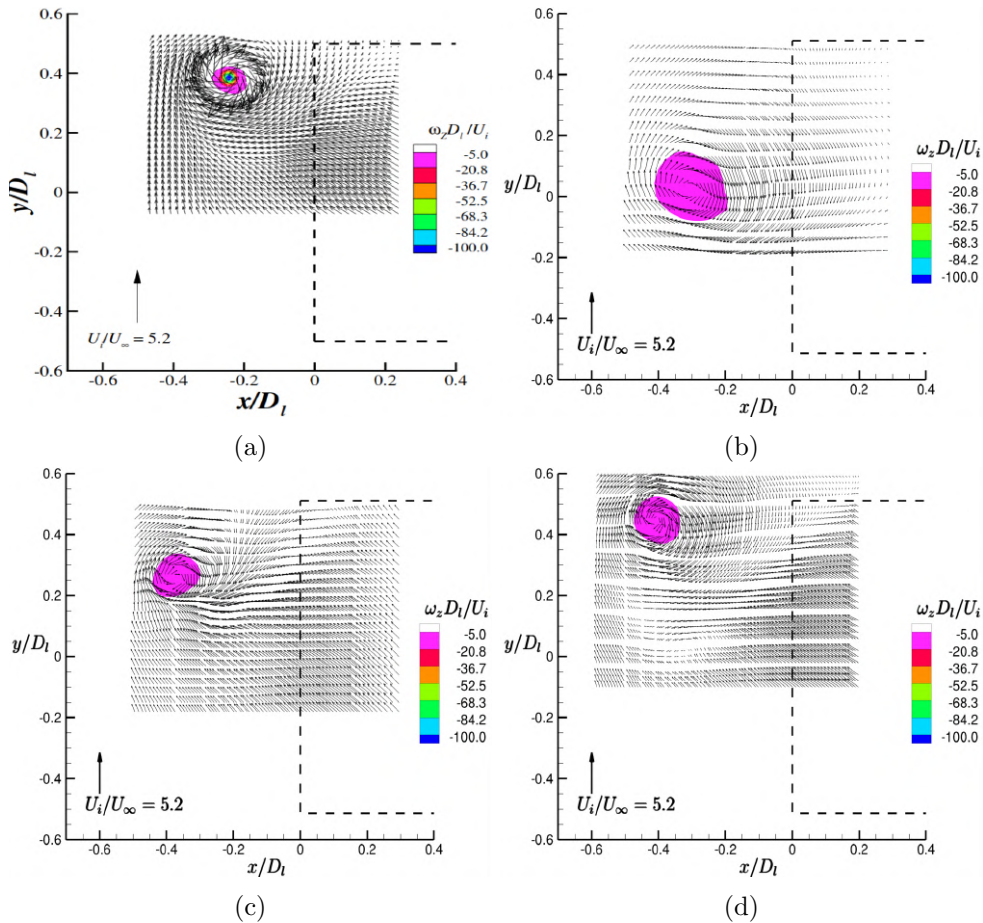


Figure 5.8: $u - v$ vector and vorticity field for a $h/D_l = 0.25$ and $M_i = 0.55$ ((a) is taken from [5])

Table 5.3: Non-dimensional parameters for different mesh sizes at $U^* = 5.2$

Parameter	Experimental	Coarse Mesh	Medium Mesh	Fine Mesh
DC_{60}	0.300	0.510	0.491	0.495
Γ^*	0.422	0.433	0.417	0.395

5.2 Discussion

The coarse mesh predicted all the flow phenomena predominantly observed during the experiments. Although fine mesh produces an accurate quantitative result, the coarse mesh is capable of producing the flow topology in these simulations. All three meshes have under-predicted the pressure loss effects of the ground vortex on the intake. However, the fine mesh results were the closest to the experimental data in the converged cases. Furthermore, the grid resolution had less influence on the location of the vortex on the ground plane for low and medium crosswind conditions from steady state results. It has to be noted that all the numerical simulations did not converge in the steady state. Furthermore, from the literature, it is clear that the ground vortex is highly unsteady at high crosswind speeds, and evidently, we have different results with different grids in the steady state RANS computations.

For case-3, the vortex was highly unsteady, and the location of the vortex on the ground plane changed a lot among the three grids. All three locations could be correct because the vortex might be hovering over these positions due to the unsteadiness. The additional inward flow separation observed is substantially over-predicted by all the numerical simulations compared to the experimental data. These phenomena were quantified using the numerical DC_{60} coefficient, and the non-dimensional circulation are tabulated above; it shows the partial capability of RANS to quantify the intake distortion.

The main conclusion from the steady state analysis are:

1. In terms of flow field topology, the influence of the spatial resolution is not very significant. Therefore, the coarse mesh of 7.1 million cells can be used to study the flow inside the intake for further cases, considering the computation costs with a fine mesh of 42.1 million.
2. For low crosswind speed, with an increase in grid density, the estimation was getting closer to the experimental data because of low unsteadiness.
3. The capability of RANS methods could be further investigated by a denser grid on the AIP and on the ground plane for the low crosswind case.
4. For cases with a medium and high crosswind, because of high unsteadiness in the vortex,

RANS is not the correct way to proceed with the study. Therefore, to study the grid independence properly, URANS simulations are performed and presented in the following section.

Chapter 6

Unsteady analysis

In this chapter, the Unsteady RANS equations are solved for both medium and high crosswind conditions. Coarse mesh is chosen for these simulations since the flow topology is not dependent on the mesh resolution. A flow field characterisation is made by showing IPR and out-of-plane vorticity contours at AIP and PIV for certain selected time steps to represent the vortex motion. Time-averaged results are compared with the experimental data to check the validity of the numerical solutions. The time series signal is also analysed in frequency domain to understand any particular insights into the characteristics of vortex motion. Comprehending these frequencies could be particularly very important in the usual case when there is a fan in the intake. This unsteadiness of the ground vortex, if periodic in the long run, could lead to fan failure by HCF.

Keeping the trend of working with non-dimensional parameters, the time evolution of the IPR and ω_z^* at several points on AIP and PIV planes will be analysed. The periodicity of the vortex is studied using frequency-based analysis using the FFT procedure.

6.1 Analysis of Unsteady Simulations

For performing unsteady simulations, the same boundary conditions were used that were determined for the steady state simulations (listed in Tab. 4.1). Initially, a time independence study was performed. After establishing temporal convergence, the most effective time step is used to run URANS simulations for the remaining cases.

6.1.1 Temporal convergence

Since there were no previous studies analysing the frequency of the ground vortex for this case, the initial time step was chosen depending on the grid size and the velocity magnitude inside

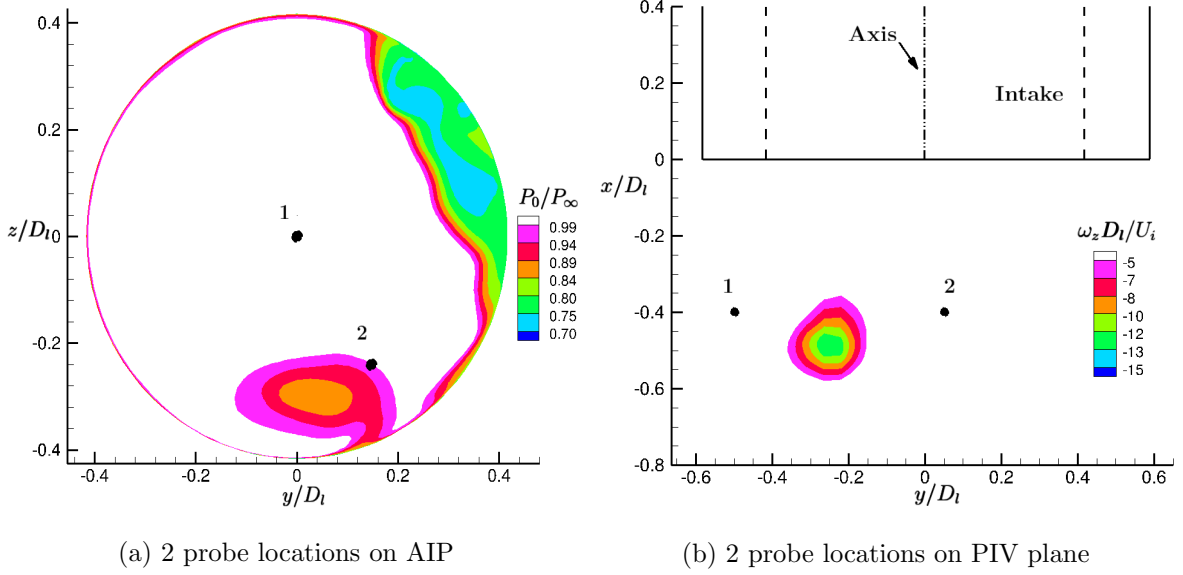


Figure 6.1: Snapshot of contours of IPR and ω_z^* of the case-3

the intake. Then the remaining two-time steps were obtained by halving the previous ones. The unsteady simulations were performed at $\Delta t_1 = 5 \times 10^{-6}$ s, $\Delta t_2 = 1 \times 10^{-5}$ s, and $\Delta t_3 = 2 \times 10^{-5}$ s. A high crosswind case ($U^* = 5.2$) was considered for this study owing to its complex distortion at the inlet due to the presence of both separation and intake vortex. It can be safely assumed that if temporal convergence has been achieved for this case at a particular time step, it can also be used to study the remaining cases. Since this inlet distortion is a complex phenomenon, the FFT of the area average IPR value of the entire plane might not provide good information about the vortex frequencies. So, few locations are chosen on the AIP, PIV planes depending on the motion of the vortex. Frequency analysis of the non-dimensional quantities on these probe locations is compared at different time steps to show the temporal convergence.

In Fig. 6.1 the locations of the probe used in this study are presented at a random instant. On the AIP plane, probe one is picked in the centre of the plane (0,0) to get clear time series data, while the second probe is picked in the path of the vortex to capture any important frequencies left out in probe-1. On the PIV plane, two probes are picked in the vortex path at either extreme.

Figure 6.2a has the IPR time series data (fluctuation about the mean) at probe 1 in the bottom plot; the signal is periodic. Upon the frequency analysis, it can be seen from the frequency domain plot that the 5×10^{-6} s and 1×10^{-5} s have a very similar result compared to 2×10^{-5} s. The first two signals have a common significant peak (highlighted) at ≈ 315 Hz, and their harmonics. From Fig. 6.2b, one can infer the same observation that 5×10^{-6} s, 1×10^{-5} s frequency domain signals look very similar. The troughs in the time series plot represent the

drop in total pressure attributed to the vortex hovering over the probe. These troughs occur periodically, and from the frequency domain, the first peak at ≈ 22 Hz represents the vortex motion. Then, one can also see a significant ≈ 315 Hz peak similar to probe-1 data, and it could be because of the intake lip separation that is seen as the high-frequency spikes in the time series data.

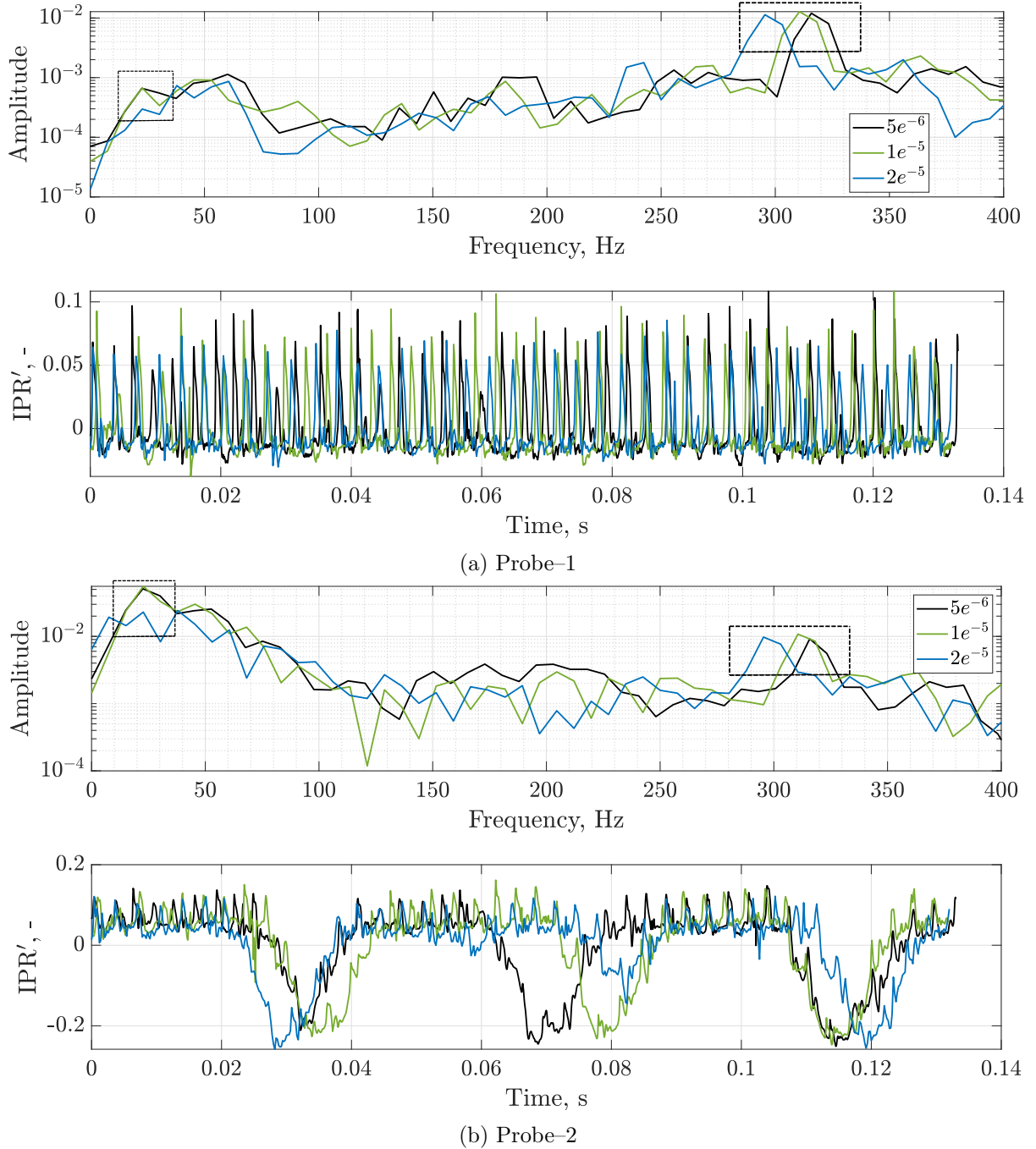


Figure 6.2: Frequency domain analysis on top and IPR time series data on bottom for porbes on AIP

In Fig. 6.3, the signal is clearer on the PIV since there is no influence of the intake lip

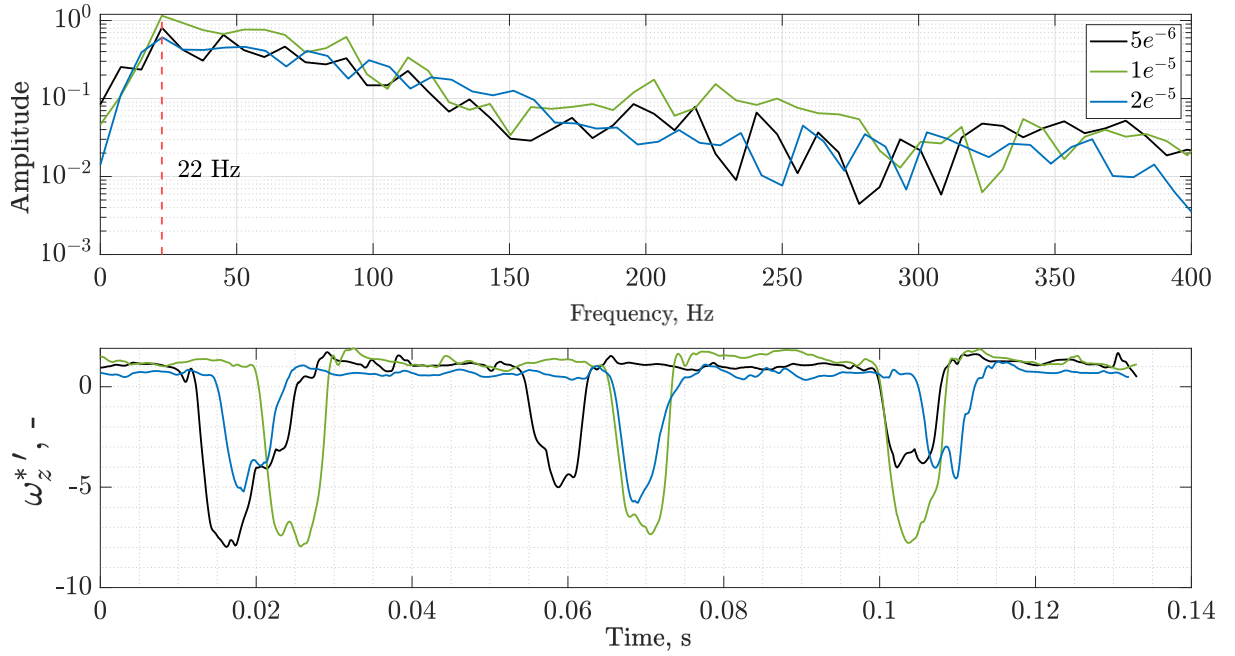


Figure 6.3: Probe-1 on PIV with FFT analysis on top and time series data of ω_z^* in the bottom

separation. Therefore, there are no high-frequency spikes in the time series data of ω_z^* shown in the bottom Fig. 6.3. Moreover, there is a clear drop in the values of ω_z^* , indicating the presence of the vortex in that particular period. This signal is fairly periodic, and this corresponds to a frequency of ≈ 22 Hz similar to one extracted from the AIP probe data. Therefore, the ground vortex moves at a frequency of ≈ 22 Hz. Also, the frequency close to 315 Hz is driven by the boundary condition at the intake exit as it is present on the ground plane but visible on AIP. This is investigated and explained further. Finally, it can be concluded that the FFT of the probe data from AIP can provide all the required frequency information of the ground vortex motion.

This small study shows that this case reached a temporal convergence with time steps of Δt_1 and Δt_2 . Since Δt_2 is larger than Δt_1 , it takes less computational resources to acquire the same length of the time signal. Therefore, a time step of 1×10^{-5} s is considered for all further unsteady simulations.

6.1.2 High Crosswind Case

To understand the behaviour of the ground vortex for high crosswind case, further unsteady simulations were performed, and some important observations were made. Five important positions of the ground vortex motion and its influence on the intake for this case are shown in Fig. 6.4. The vortex is exhibiting a periodic motion from the left extreme (downstream edge of

intake) to the right extreme (centreline of intake). As the ground vortex is moving, its strength and influence on the AIP plane vary depending on its position relative to the intake.

At instant t_1 , one can see the weak ground vortex, positioned at the left extreme on the leeward side, almost blown away by the strong crosswind extending all the way into the intake. Since the vortex core on the ground plane is far from the bottom of the intake, it has a very small influence on the total pressure on AIP(almost 6 O'clock position).

Next, at t_2 , the ground vortex is at the mid position of its path, axially a bit further away from the intake growing stronger in strength. Consequently, on the AIP, the intake distortion has increased in strength and moved from the bottom of the intake towards the windward side (5 'O clock position). At t_3 , the ground vortex is very close to the intake both in x and y directions, appearing to be very strong in this configuration. At this vantage position, the ground vortex significantly affects the intake inlet. The core of total pressure loss has moved completely to the windward side leading to a total pressure loss of more than 30% on AIP.

This variation of the strength of the vortex with the location on the ground is linked to its location inside the sucked streamtube. As discussed in the literature (see Fig. 2.5), the ground vortex is created by the interaction of the sucked streamtube with the ground, and the size of the streamtube depends on the crosswind velocity. For constant U^* , the size of the streamtube is constant; therefore, when the vortex is at the extreme on the leeward side of the intake, it is almost very close to the edge of the streamtube. At this location, as it can be seen in Fig 6.6, the velocity of the flow entering the vortex at t_1 is almost half that of t_2 , creating a very weak vortex. This could also be seen as the vortex is close to being blown away, leading to the almost disappearance of its influence on AIP. On the flip side, when it is at the right extreme, the vortex is comfortably located inside the streamtube with the flow at high velocity, entering the vortex and leading to its maximum strength.

Apart from this motion between extremities, the ground vortex also makes another periodic motion with a shorter amplitude presented in Fig. 6.4d,e. Both the minor and major locations are clearly represented in Fig. 6.5. From its position at the instant t_3 , the ground vortex enters its shorter periodic motion, with its left extreme at time t_4 , and right extreme at t_5 . In this period of time, the total pressure loss on the intake is not severe but considerable at 15%. The existence of two different periodic motions for high crosswind case could be due to the complex interaction of the ground vortex with separation. Both the oscillations occur successively; therefore, they have the same frequency of about 22 Hz.

No particular inference could be made about separation, as it doesn't seem to follow any trend. But, two things about the separation can be observed. The strength of the separation is not

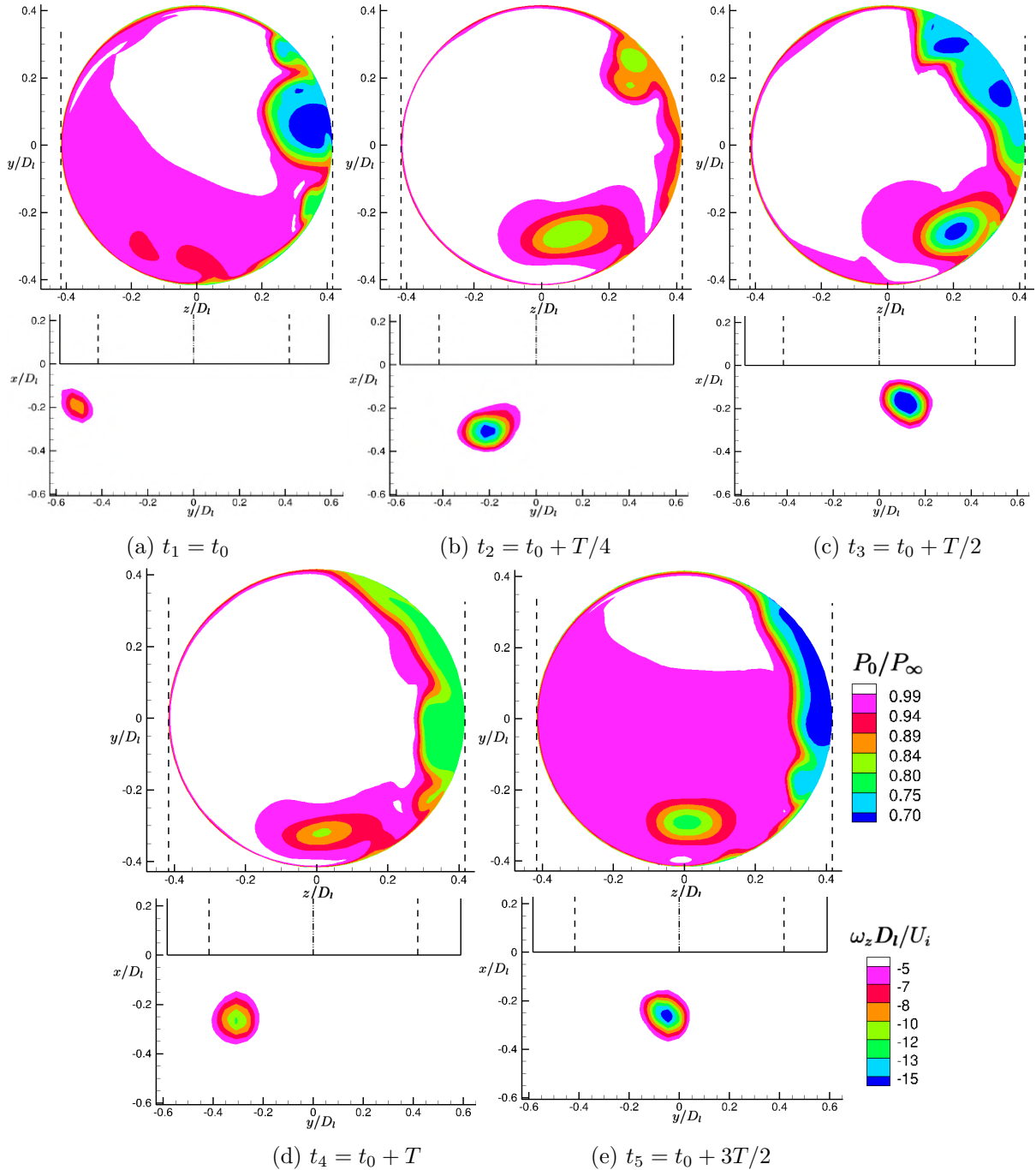


Figure 6.4: Variation of IPR (top) and ω_z^* (bottom) at the AIP and PIV respectively at five instants of time for $U^*=5.2$

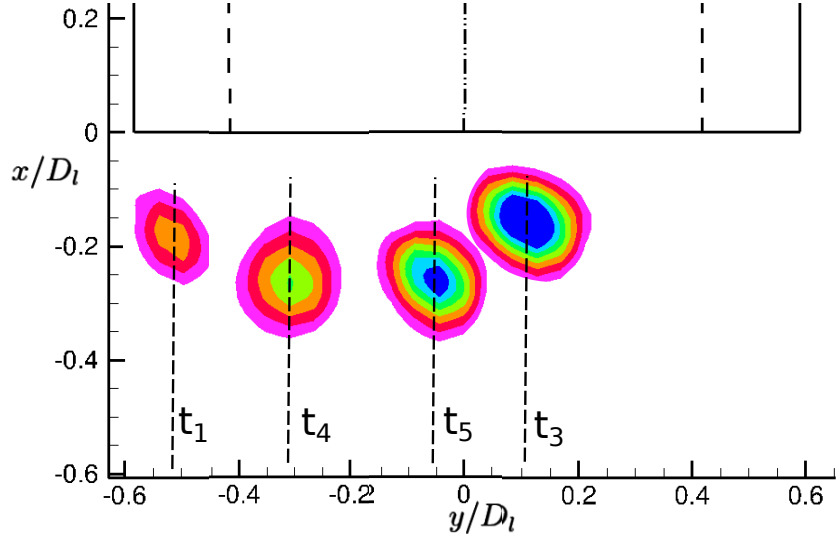


Figure 6.5: The vortex location superimposed on PIV plane to represent vortex major and minor motion

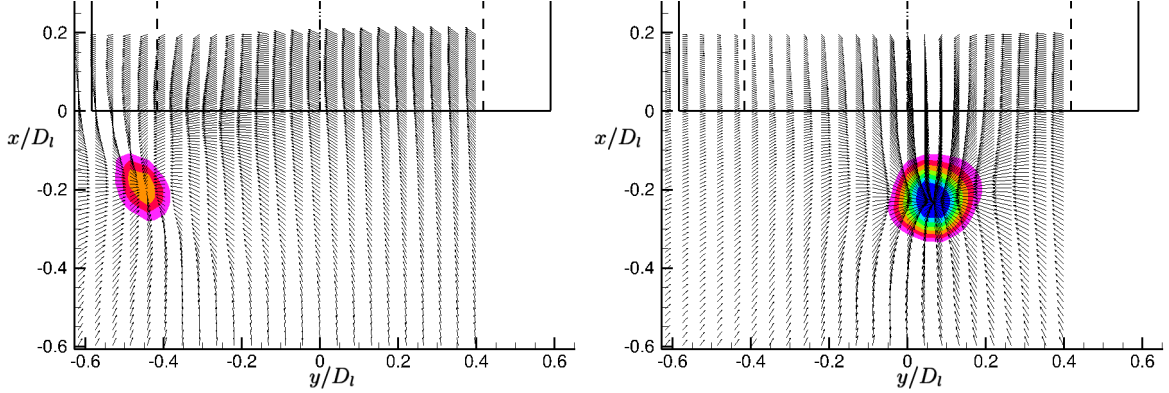


Figure 6.6: $u - v$ velocity vector plots and the vortex locations on PIV at t_1 (left), and t_3 (right)

over-estimated as in the steady state simulations. Secondly, it has a broadband frequency, and the shear layer is unstable. The pink pulsation of the entire intake surface is due to the boundary condition at intake exit leading to the high-frequency content (at ≈ 315 Hz) in the time series signal discussed before.

6.1.3 Medium Crosswind Case

The medium crosswind case is studied with URANS under the same boundary conditions at a time step of 1×10^{-5} s to understand the unsteadiness of the ground vortex. This case is expected not to show any separation on the windward side of the intake.

Figure 6.7 represents the ground vortex extreme locations, with t_1 being the right and t_2 being the left extreme. There is no significant vortex movement on the ground that can be observed

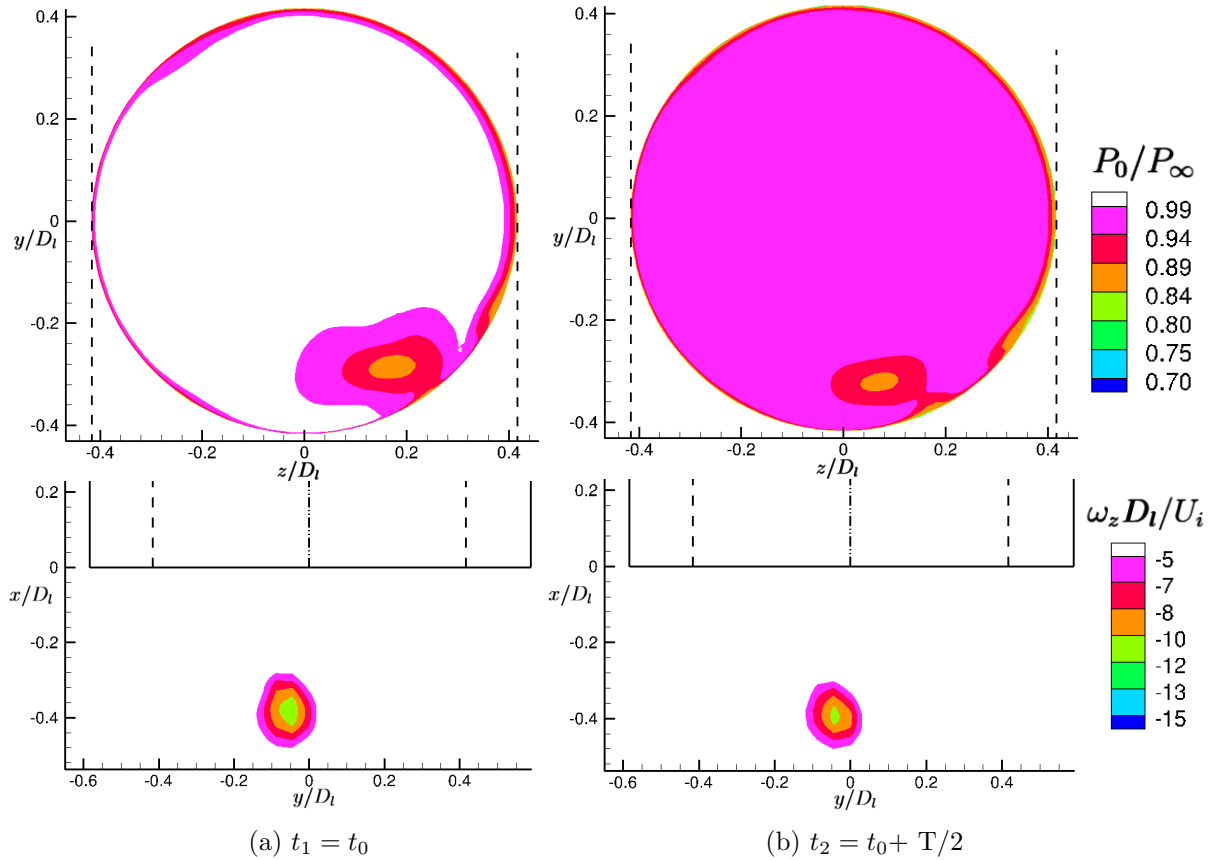
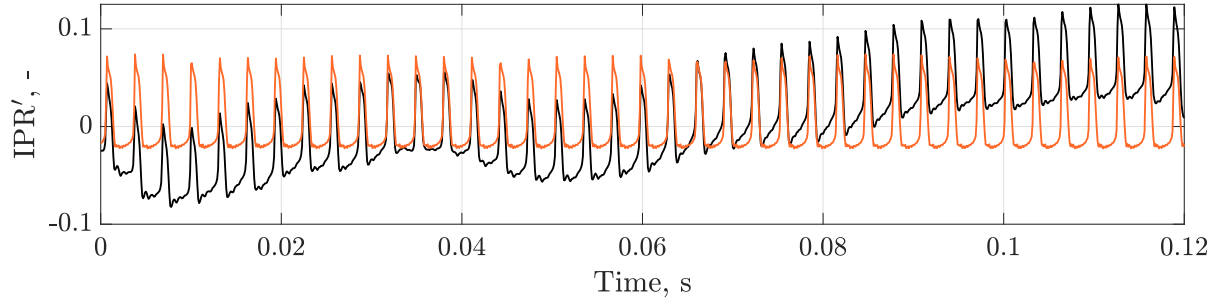
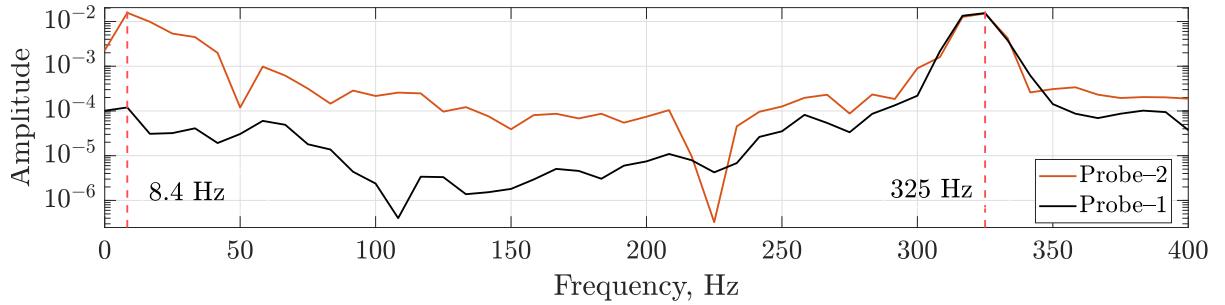


Figure 6.7: Variation of total pressure (top) and vorticity (bottom) at the AIP and PIV respectively at five instants of time for $U^*=9.1$

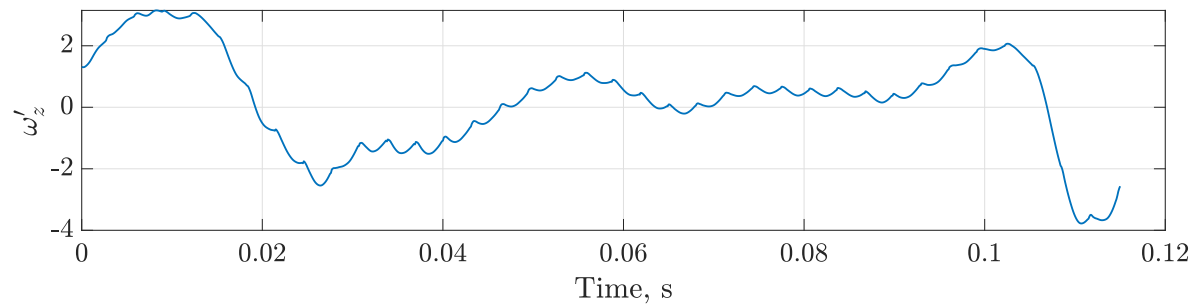
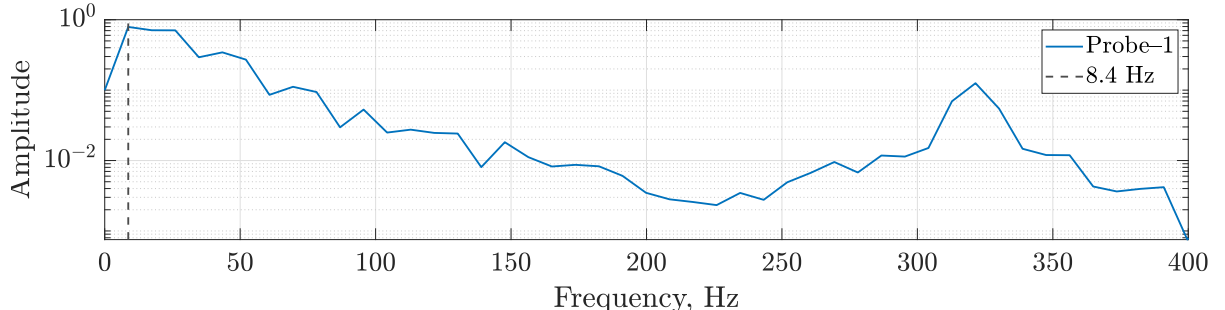
here, but there is a difference noticeable on the AIP with the core of the total pressure loss moving between 6 'O clock and 4 'O clock position. Upon FFT of the data, Fig. 6.8a shows the analysis of IPR on the AIP plane at two different probe locations, same as the case-3, the ground vortex frequency is found to be 8.4 Hz.

Since probe-2 is located in the path of the vortex picks up a stronger amplitude at 8.4 Hz compared to probe-1. This frequency of the vortex is almost one-third compared to the high crosswind case. This frequency can be confirmed from the probe data on AIP plane shown in Fig. 6.8b. However, another significant peak in the frequency domain at 325 Hz corresponds to the high-frequency spike present in the time series data. This high frequency is not physical since there is no separation present in this case which is evident from Fig. 6.7. Also, there is still a pulsation (represented by the pink contour) observed on the AIP periodically at the different time instants shown in Fig. 6.7.

Upon further investigation, it was found that this pulsation present in the intake was numerical and emerged from the mass flow boundary condition used at the intake outlet. Since the mass flow boundary condition is a weak condition, implying that the imposed mass flow is



(a) Probe-1,2 on AIP

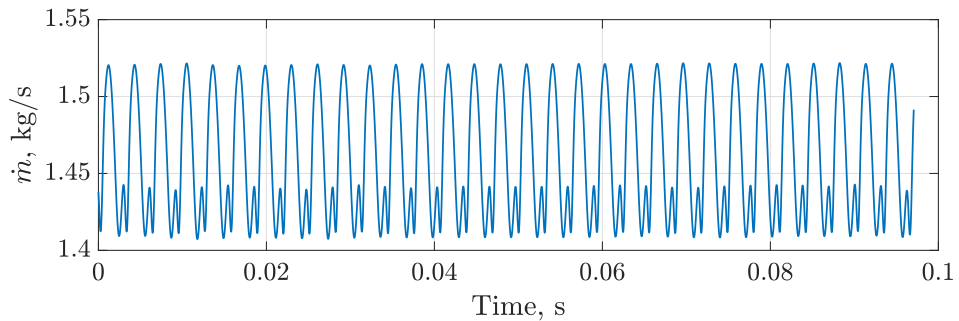


(b) Probe-1 on PIV plane

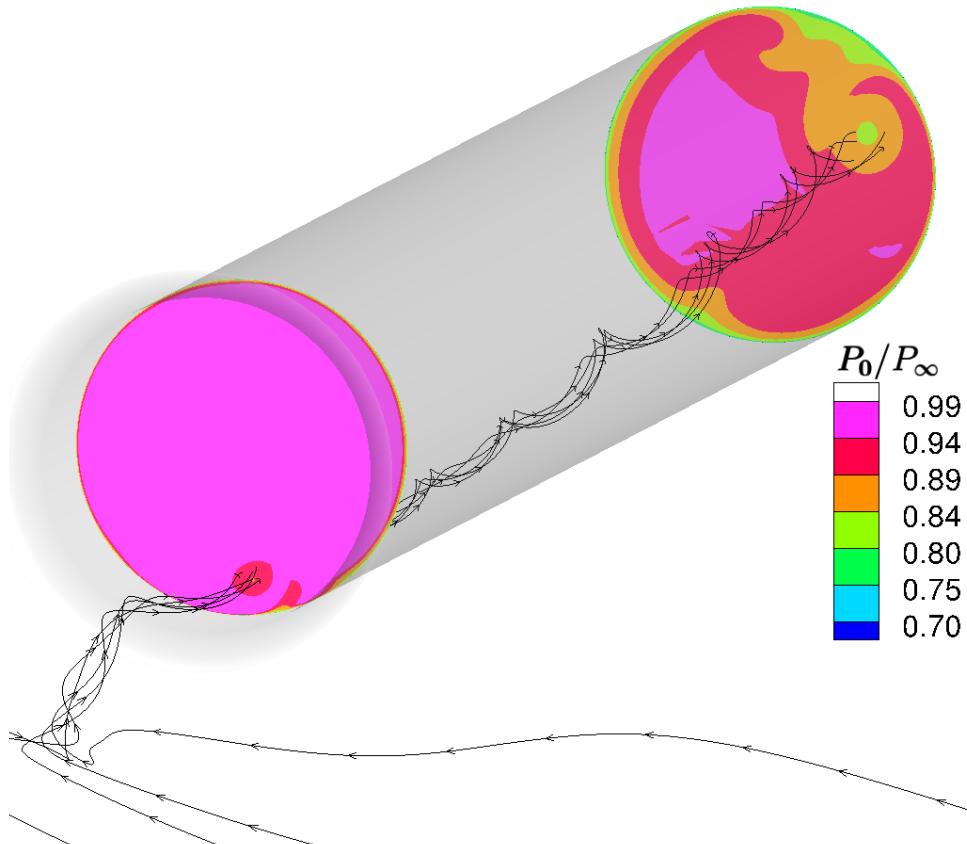
Figure 6.8: FFT analysis (top) of the time series data from probe (bottom)

maintained by regulating the static pressure. Therefore, mass flow boundary conditions don't directly influence the flow. It can be seen in Fig. 6.9a that the mass flow on the intake exit oscillates a lot about the imposed mass flow rate of 1.46 kg s^{-1} . This change is almost 8 %, and the frequency of oscillation is approximately 321 Hz. Similar behaviour was observed in the case of high crosswind conditions; it was assumed that the high frequency of 315 Hz was the separation frequency rather than the flow pulsation due to the reflection from mass flow boundary

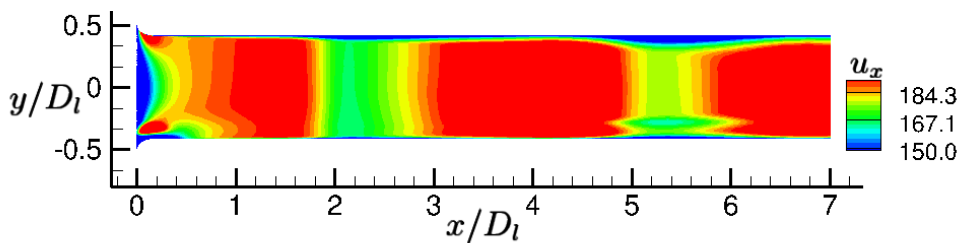
conditions.



(a) Mass flow rate fluctuation on intake exit plane



(b) Streamlines tracing the vortex travelling from ground to intake exit through AIP



(c) Centreline velocity contour for the plane ($z = 0$) passing through the centre of intake for $U^* = 9.1$ at snapshot

Figure 6.9: Mass flow boundary condition influence on numerical solution for $U^* = 9.1$

Figure 6.9b shows how the vortex is convected from the ground plane to the intake exit inside the intake. The intake exit has a reflective boundary surface; when the ingested vortex hits the exit surface, acoustic signals are transmitted from the intake exit. The mass flow boundary condition calculates the corresponding back pressure and assigns it uniformly on the entire exit surface. But, it can be seen in Fig. 6.9b that the ingested vortex travels downstream and hits the intake exit it creates a pressure difference on the surface leading to a non-uniform boundary. Therefore this difference makes the solution numerically unstable alongside the inherent unsteadiness caused by the vortex and separation. From the instantaneous flow solution inside the intake cylinder, a planar wave can be seen moving through the intake between the intake outlet and the highlight plane in Fig. 6.9c showing this instability. Therefore, the mass flow boundary condition is not the appropriate method to numerically solve the ground vortex unsteadiness problem. Hence, a better boundary condition (numerically) has to be employed to solve this pulsation issue.

6.2 Static pressure boundary condition

To tackle the problem of the reflecting acoustic back from the intake exit, the simulations are performed using static pressure boundary condition. In theory, it doesn't reduce the reflection completely but controls the amplitude of oscillation in the mass flow at the intake exit, thereby restricting the numerical instabilities of the flow solution. Though this boundary conditions specifies uniform back pressure on the intake exit, it has better control over the flow than the mass flow boundary condition.

The main problem with this boundary condition is that mass flow at the intake exit cannot be directly imposed. Therefore a corresponding static pressure has to be calculated from the previous simulation data and, using the trial and error method, the required mass flow rate close to 1.46 kg s^{-1} is achieved. Acquiring the correct mass flow is important for two reasons, one being for the comparison with the experimental results, and the other is that the separation and the ground vortex might not occur at different mass flow rates. Since the ground vortex presence depends on the interaction between sucked streamtube (which can be smaller) and the ground, acquiring a correct mass flow is essential.

While the rest of the boundary conditions remain the same, the intake exit is changed to outlet static pressure with different values of static pressure for different crosswind conditions. The static pressure values and the acquired average mass flow rate for the three cases are tabulated in Tab. 6.1. The mass flow rate at the intake exit in all three cases is very close to the required

Table 6.1: Imposed static pressure boundary condition values at intake exit

Case	Static Pressure, kPa	Mass flow rate, kg s^{-1}
1	79.04	1.46
2	78.56	1.47
3	74.82	1.47

mass flow (and the difference is less than 1%). All the unsteady simulations are performed again using these new boundary conditions.

6.2.1 Medium Crosswind Case

The medium crosswind case simulation is performed using static pressure as a boundary condition at the intake exit. Similar observations have been made as the mass flow boundary condition, except for the pulsation on the AIP plane due to the reflective boundary condition disappearing shown at random instant in Fig. 6.11a. The instantaneous locations of low IPR values for both the boundary conditions are plotted in Fig. 6.11b. It can be seen that without the presence of the reflected acoustic wave in the intake, the vortex movement inside the intake has increased. However, the vortex on the ground plane was fairly steady similar to the mass flow boundary condition.

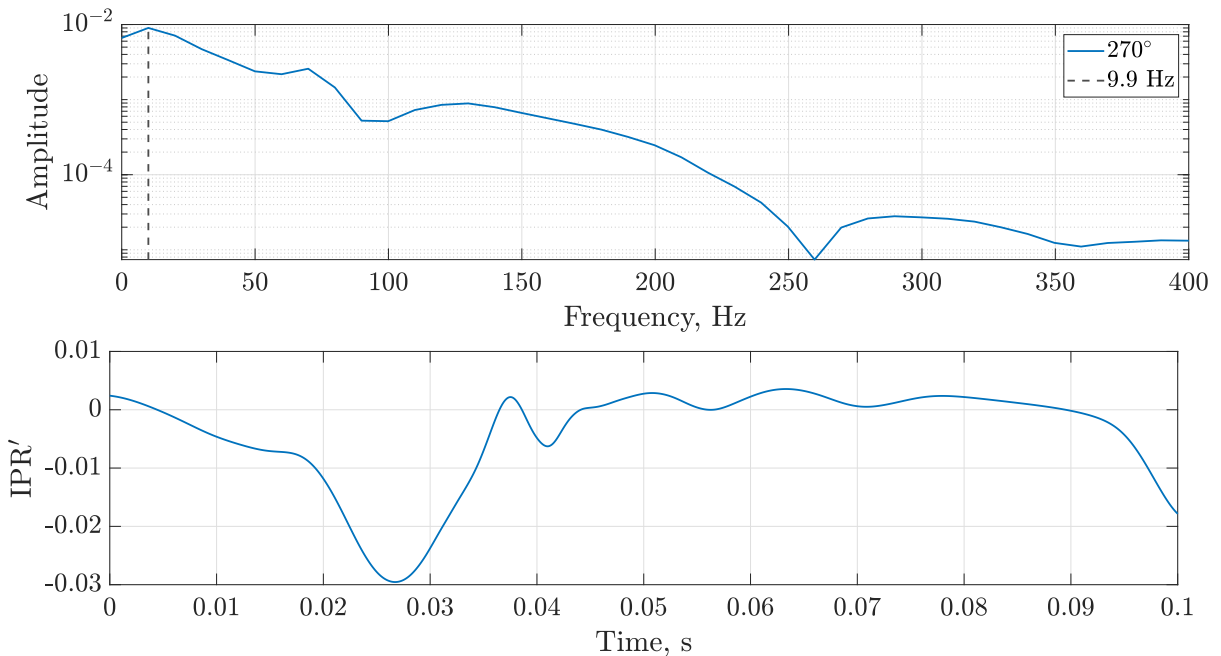
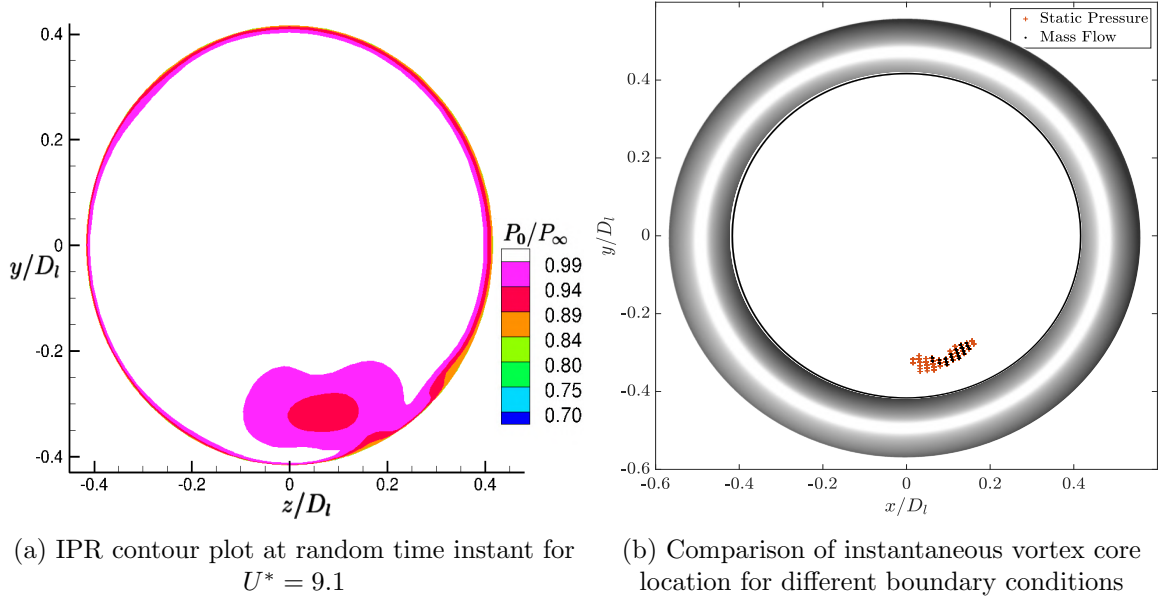


Figure 6.10: FFT analysis of probe-1 on AIP on top and time series data of IPR in the bottom

It can be seen from the FFT analysis shown in Fig. 6.10 that there is only one peak at

9.9 Hz which corresponds to the ground vortex frequency. Moreover, even if the influence of the boundary condition is not entirely eliminated, it is at least three orders of magnitude lower than the mass flow boundary condition case. There is no high-frequency content in the time data signal of IPR measured at probe-1.



(a) IPR contour plot at random time instant for $U^* = 9.1$

(b) Comparison of instantaneous vortex core location for different boundary conditions

Figure 6.11: Vortex influence on AIP

6.2.2 High Crosswind Case

With the new boundary condition, the pulsations inside the intake are also absent for this case, and some differences in the motion of the ground vortex are observed. This case still has two different periodic motions one with a longer amplitude (represented in t_1 to t_3) and other with a shorter amplitude (presented in t_4 and t_5) as seen in Fig. 6.12. The frequency of occurrence of these motions has changed compared to the mass flow boundary condition. The shorter motion frequents once after every long-term motion; therefore, the longer amplitude motion has twice the frequency of the short-term motion.

From the FFT of the probe-1 on the ground plane shown in Fig. 6.13, the frequency of 15 Hz corresponds to the shorter (or secondary) motion, making the frequency of the longer (or primary) motion as 30 Hz. The frequency peak at 60 Hz corresponds to this primary motion; since the probe is located in the middle of the longer path, each oscillation is counted as two in FFT. It must be noted that these frequency values should not be followed to the decimal; due to the shorter time signal, it is good to assume a $\pm 10\%$ range at each frequency obtained here.

Figure. 6.14 presents the instantaneous location of the vortex core for different different bound-

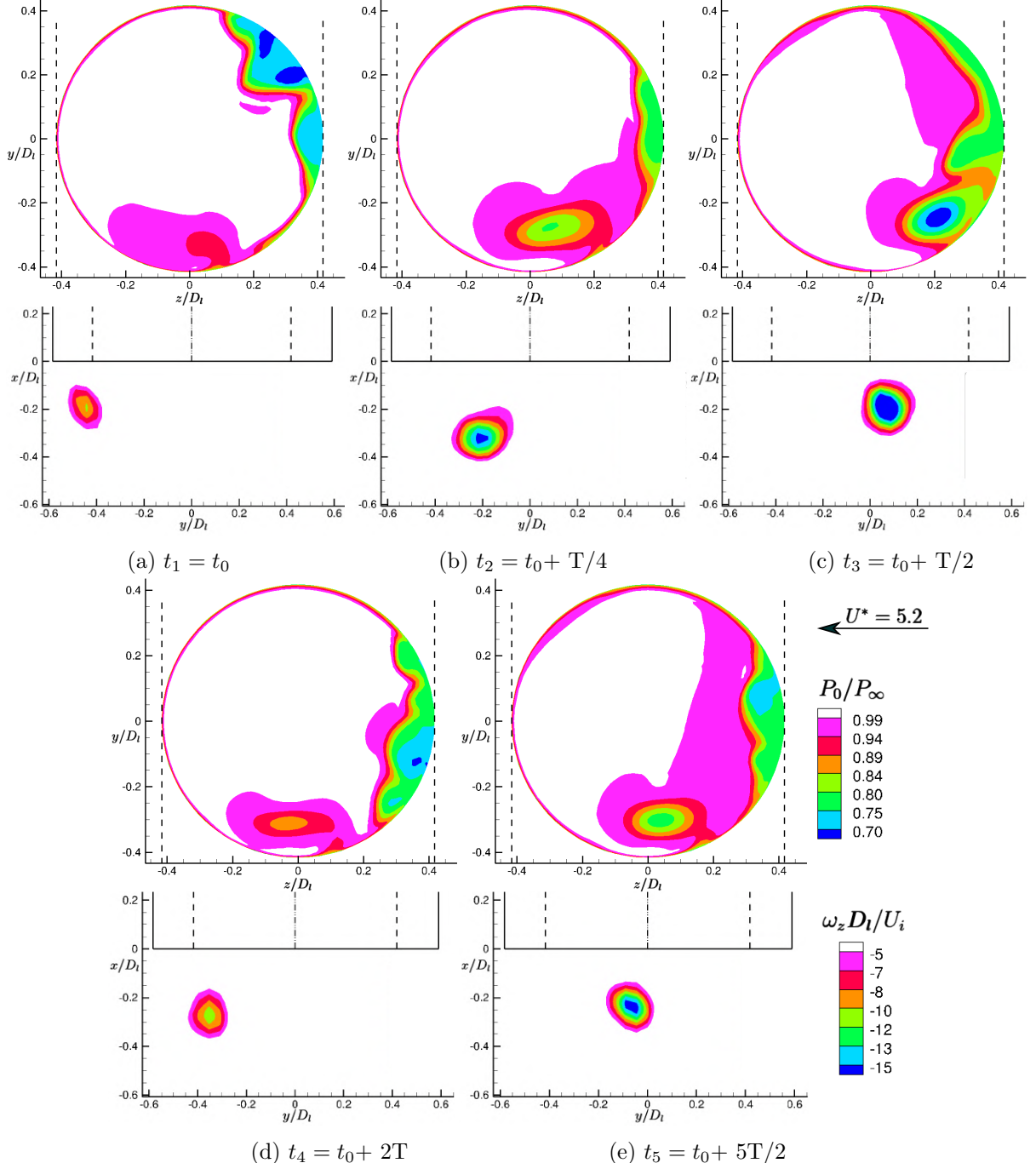


Figure 6.12: Variation of IPR (top) and ω_z^* (bottom) at the AIP and PIV respectively at five instants of time for $U^* = 5.2$

ary conditions. On the AIP plane, the amplitude of the vortex motion has increased compared to the mass flow boundary condition, and the vortex followed almost the same path. Fig. 6.14b shows the path the vortex tracks on the ground, and it is not a straight path but rather a curved path between the leeward side and the centre of the intake from t_1 to t_3 respectively. The path of the ground vortex is almost the same, with the amplitude being slightly larger for

static pressure boundary conditions. It is also clear that the amplitude of the shorter motion is half that of the longer one.

Another important flow phenomenon in the high crosswind condition is the presence of intake

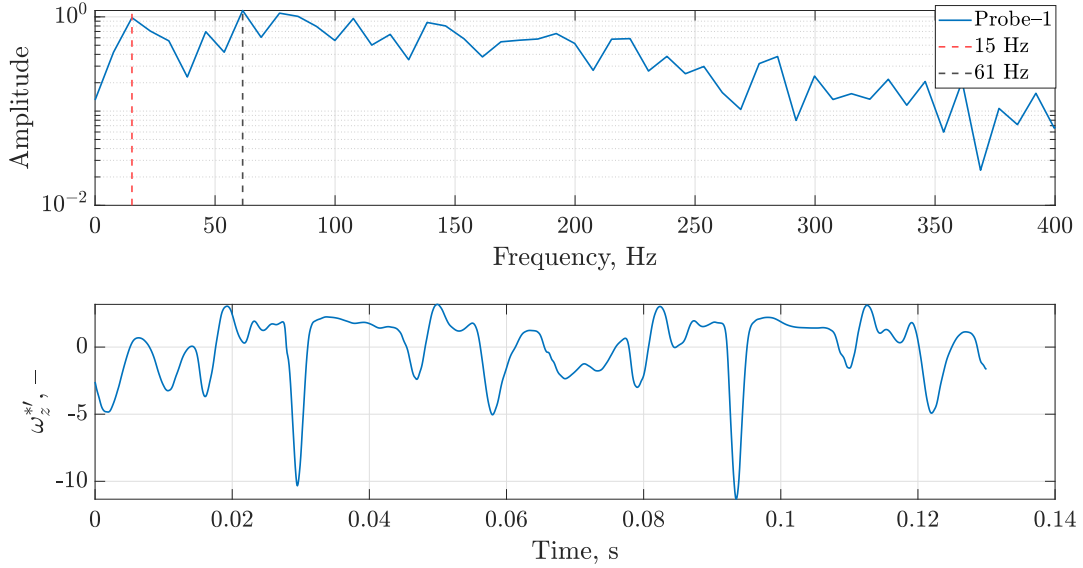


Figure 6.13: Probe on PIV with FFT analysis on top and time series data of ω_z^* in the bottom

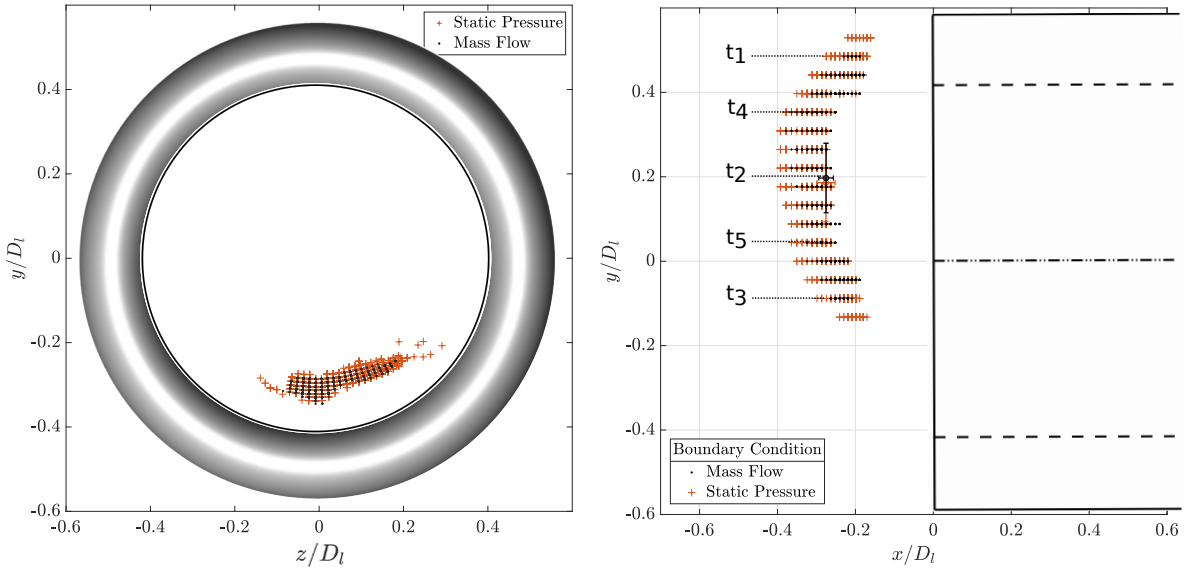


Figure 6.14: Comparison of instantaneous vortex core location representing the minimum IPR on AIP on the left, maximum ω_z^* on PIV plane on the right

lip separation on the windward side. The literature confirms that the separation has a high frequency compared to the ground vortex. Frequency domain analysis of the time data signal from probes taken inside the intake separation did not produce any single or narrow band frequency, thus it is a broadband range of frequencies. Furthermore, from Fig. 6.12, the separation shear

layer looks very peculiar. Several irregular-shaped structures are visible inside the separation zone on AIP which don't portray a clear separation. To understand this 3-dimensional separation inside the intake, a plane parallel to the ground passing through the centre of the intake is considered to see how the separation looks and propagates downstream. Moreover, three more planes parallel to AIP are considered one very close to the lip and two downstream of AIP plane at a distance of $d = 0.416D_l$ apart from each other.

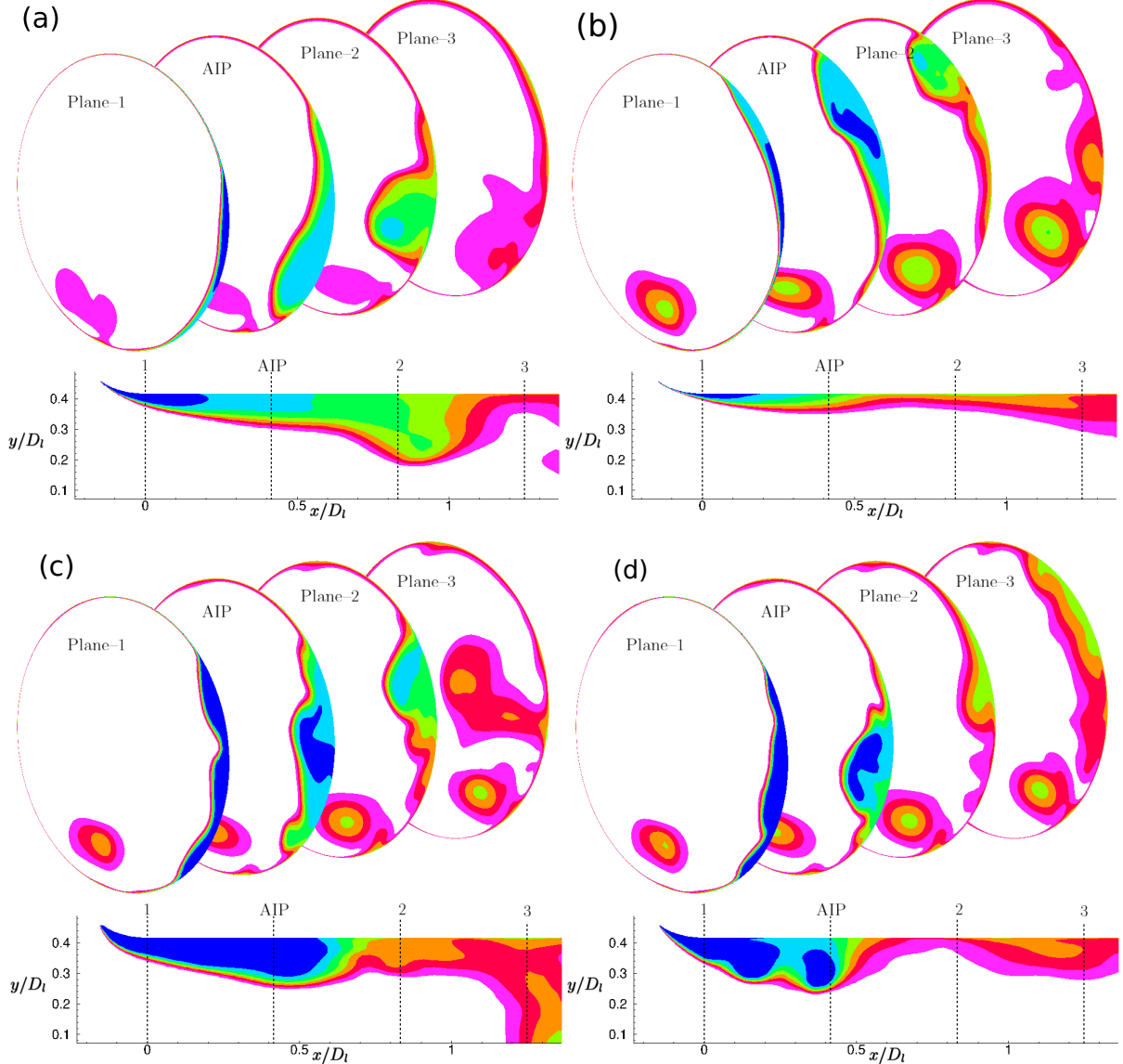


Figure 6.15: Variation of IPR at several x -planes parallel to AIP (top) and $z=0$ plane parallel to ground (bottom) through the intake at four random time instants

The plane-1 in Fig. 6.15 shows a clear separation shear layer at all the time instants that looks more physical than at AIP. This separation is highly unstable and sheds at various frequencies; therefore, the snapshots were presented randomly. The shedding is propagated

downstream into the intake and can be observed as blob-like shapes on AIP and further planes. Even at the time instants where a strong separation bubble is seen on the z -plane, the flow re-attaches before reaching plane-2. Furthermore, the vortex extends from the leeward side into the intake; as it travels downstream, it can be seen moving towards the intake's windward side and interacting with the separation. So, even though the vortex is away from the separation region on AIP, it interacts with the shed separation downstream.

Since the separation is a complex $3D$ phenomenon, more advanced data processing techniques such as Proper Orthogonal Decomposition (POD) has to be conducted to investigate the frequency and energy content.

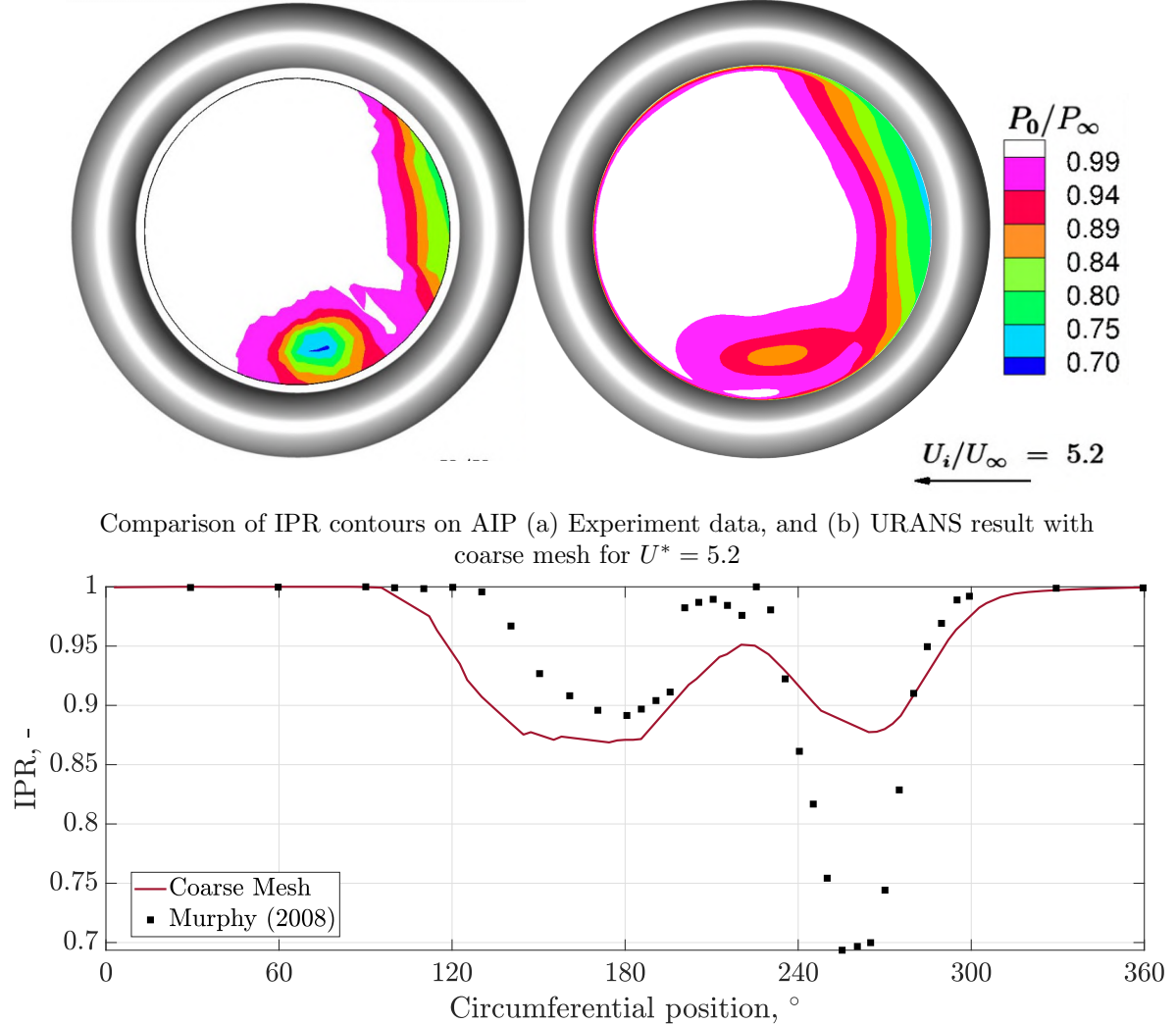
6.3 Comparison with experimental data

The experiment data provided in the AIAA PAW-05 is a time average plot over a period of 5 s with a sampling frequency of 600 Hz. Therefore time average URANS solution can be compared with the experimental data. It has to be noted that URANS simulations are performed using coarse mesh. It was concluded from the steady state results that coarse mesh could reproduce all the flow topology seen in the experiments.

Figure. 6.16a,b shows that URANS for high crosswind condition has done a much better job in predicting the flow inside the intake better than RANS analysis. The most improvement can be observed in the prediction of the separation region for high crosswind case; while the steady-state had predicted a very huge separation zone, URANS time average results shows a gradual increase in total pressure loss from the centre to the intake walls. However, the pressure loss in the separation zone and the extent of the separation is slightly over-predicted, whereas, inside the vortex core, the total pressure loss is under-estimated.

The $x - y$ line plot in Fig. 6.16c compares the IPR at all the circumferential locations at the radius of maximum pressure loss. It can be seen that there is an over-prediction in the separation region, both in the magnitude and the onset of total pressure loss which can be likely due to the coarse mesh, better agreement with fine mesh can be expected. Furthermore, this loss is spread over a wide range of 70° angle, implying a larger motion of the vortex inside the intake. This large amplitude results from the extensive movement of the vortex on PIV plane starting from the centre till the leeward side of the intake, as seen in Fig. 6.18. Since the standard deviation in y of both the data for this case looks the same, which could mean that the amplitude of the ground vortex motion is almost the same, the average of vortex movement is off by $0.1D_l$, suggesting that the vortex in the experiments is going even further in the leeward direction of

intake. From Fig. 6.17, at medium crosswind on AIP the results are fairly comparable, the



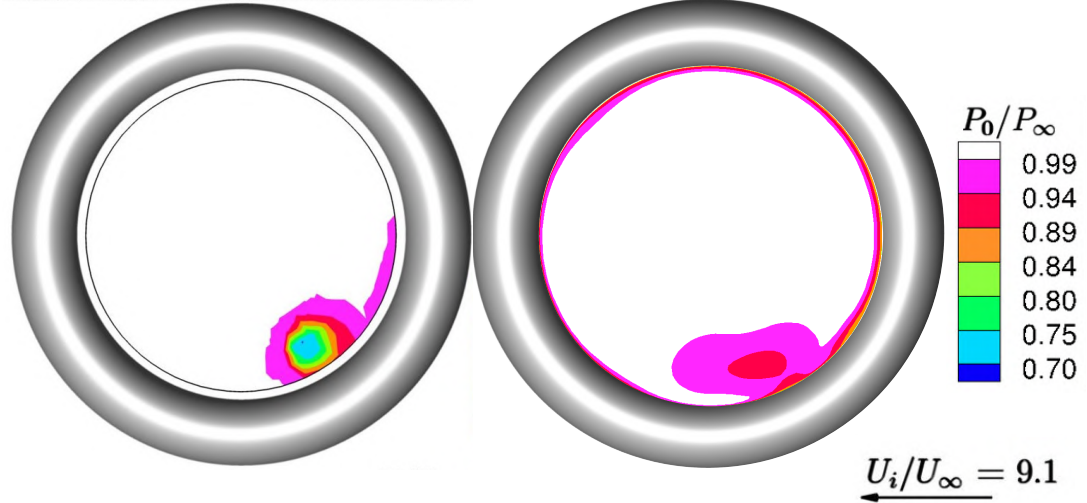
(c) Azimuthal IPR distributions at a fixed radial position crossing the peak loss flow regime

Figure 6.16: Comparison of time average data for $U^* = 5.2$ (Experiment data is recreated from [34])

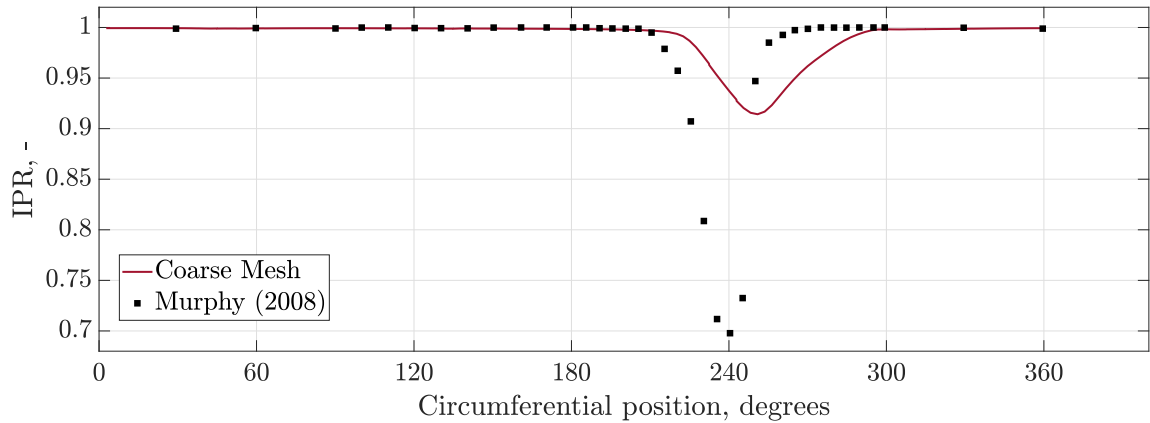
total pressure loss at vortex core is under-evaluated, and the location of vortex core is predicted to be at an offset of 10° compared to the experiments. Since it is a time average result, the circumferentially earlier existence of the vortex conveys that it is going further upward, close to the windward side of the intake. The complementing effect can be observed on the PIV plane, where the vortex has a larger movement in the experiments than in numerical simulations (see Fig. 6.18). From the experimental data, the standard deviation in the y axis looks the same as the high crosswind case; it can be inferred that the vortex is moving a lot in PIV plane, which is not seen numerically.

Concerning low crosswind speed, the steady state has provided a very good solution; it is established that at low crosswind speeds, the vortex is stationary on the ground plane. It is

evident from Fig. 6.18 that vortex is almost stationary numerically. Because of a stationary ground vortex, there is no vortex motion in the AIP as well. The average location of the predicted vortex is off by $\approx 0.15D_l$ close to all the other cases. Since the vortex motion for this case is almost negligible, no extensive study is presented in this report.



Comparison of IPR contours on AIP (a) Experiment data, and (b) URANS result with coarse mesh for $U^* = 5.2$



(c) Azimuthal IPR distributions at a fixed radial position crossing the peak loss flow regime

Figure 6.17: Comparison of time average data for $U^* = 9.1$ (Experiment data is recreated from [34])

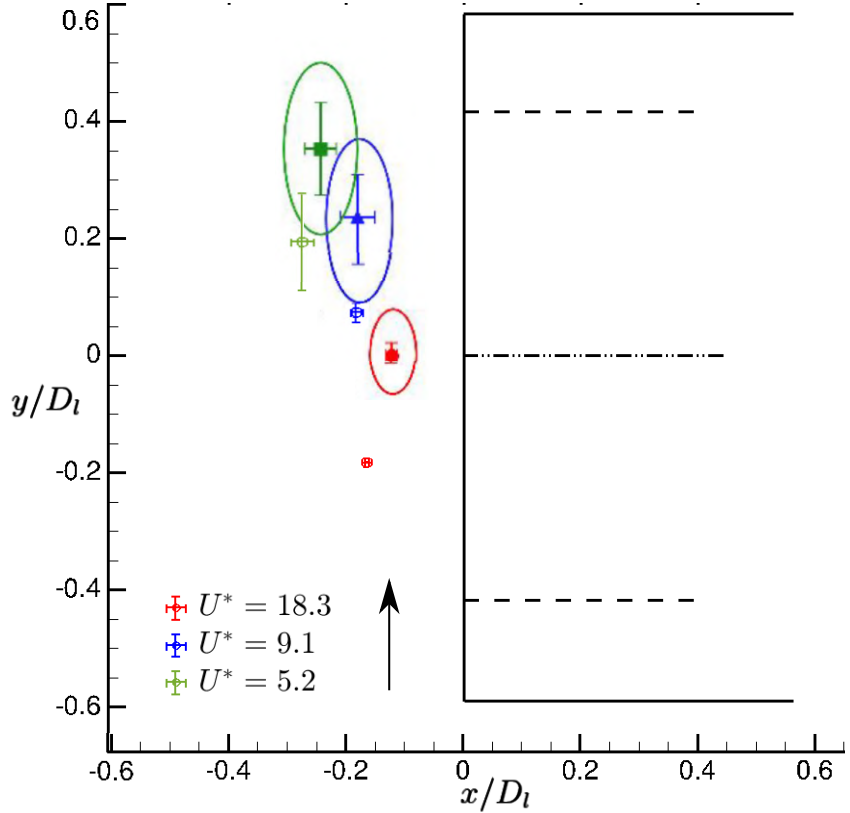


Figure 6.18: Averaged ground vortex core locations at the vortex measurement plane (experiment data highlighted in ovals) with markers representing the average location, bars indicate the standard deviation in $x - y$ plane

6.4 Chapter Summary

In this chapter, Unsteady simulations were performed in HADES[®] for the medium and high crosswind cases using coarse mesh. Firstly, a study was performed to acquire results independent of the time step used for URANS simulations. Frequency domain analysis of the time data of probes on AIP and PIV planes was used to establish the temporal convergence. For the high crosswind case, $\Delta t = 1 \times 10^{-5}$ s produced converged results. Using this time step, unsteady simulations were performed on the case-2,3 and observed two dominating frequencies. Out of these two, the smaller one corresponds to the ground vortex oscillation. The higher one, initially considered separation frequency, transpired to be a numerical acoustic wave. Upon further investigation, it emerged from the mass flow boundary condition imposed at the intake exit.

Later, the numerical acoustic wave propagating inside the intake was attenuated using static pressure boundary conditions at the intake exit. The medium crosswind case was found to have a small vortex oscillation on the ground. This ground vortex frequency is learned as 9.9 Hz.

For the high crosswind case, there is an influence of both ground vortex and separation on the intake. In this case, the ground vortex exhibits two motions of different amplitudes and different frequencies along the same path. The frequencies of 15 Hz and 30 Hz correspond to the shorter and the longer motion, respectively, with the short one being almost half the amplitude of the longer motion. This was not observed in the medium crosswind case; therefore, this secondary could have been manifested due to the complex interaction between the vortex and the intake lip separation.

To understand the separation in $3D$, several other planes were sliced inside the intake. From the study, it can be concluded that this is indeed a very complex behaviour that does not occur at one particular frequency but in an extensive range.

Finally, the time average results from URANS are compared with the experimental data. A very good match of the flow field results was observed on the AIP for both the medium and high crosswind conditions. These results defined the separation region in the experiment more clearly; since the shear layer was always oscillating, the time average gave a proper gradient of the pressure loss that matches the experiment data. There was no motion of ground vortex in the low crosswind case using URANS, and the study is not presented in this chapter. Then regarding the accuracy of prediction, the numerical simulations were a little off, but that should be fixed when the simulations are performed using a fine mesh. In this chapter, finer meshes are not explored because of the time constraint.

Chapter 7

Conclusions and Recommendation

The characteristics of intake ground vortices have been investigated for low, medium and high crosswind velocities with $U^* = 18.3, 9.1$ and 5.2 respectively, using RANS and URANS-based computational methods in HADES®. These calculations were validated against the experimental data set provided by the AIAA PAW-05 workshop and the experiments conducted by Murphy [5] at Cranfield university. The prime objective is to validate HADES and see how accurately it can predict this highly unstable and complex ground vortex motion and its effects on intake. Furthermore, a proper numerical setup and the influence of several modelling parameters and non-dimensional parameters are studied in this work.

The numerical research has been performed sequentially. Firstly, a steady state URANS study is performed to learn the effect of the incoming boundary layer and different turbulence models on the intake. Then with an established numerical setup, a mesh convergence study is performed, and the results are validated against the experimental results. Then URANS simulations are performed using these steady state results and compared with the time-average experimental data. Finally, frequency domain analysis has been performed to understand the motion of the ground vortex in front of the intake.

7.1 Conclusions on the Project

Boundary conditions of the numerical setup play a vital role in the analysis of the intake in crosswind conditions.

Firstly, the boundary layer plays a very important role in predicting the ground vortex since the intake is placed very close to the ground. From the study performed in § 4.4.1, the vortex did not appear in the high crosswind case when using uniform profile at inlet boundary condition.

This is because the boundary developed very close to the ground and blew the vortex away from the intake. Hence, the boundary layer profile measured from the experiments is used. Furthermore, different turbulence models were studied and found that the Spallart-Allmaras method coupled with rotation and curvature corrections (RC) and QCR produced the best flow topology close to the experiments.

Using the steady state RANS simulations, it is understood that low crosswind conditions are fairly steady. In this case, the results obtained by the fine mesh compare very well with the experimental data but are not entirely. Therefore, a finer grid can be investigated using this numerical setup for more accurate results. The medium and high crosswind conditions have inherent unsteadiness, which was not properly predicted by the steady-state calculations. In the high crosswind case, the total pressure loss and the extent of the separation region in the separation zone are over-predicted. Therefore, the grid independence study using steady state computation is inconclusive. To achieve grid independence, unsteady computation is required, which is outside the scope of this project.

Subsequently, URANS computations were conducted to investigate the behaviour of ground vortex and intake separation. Due to time constraints, preliminary computations were carried out using the coarse mesh. From the initial study, it is learned that there is a numerical acoustic wave coming from the intake exit tampering with the flow solution. This is because of the mass flow boundary condition used at the intake exit. This is attenuated by using the static pressure boundary condition, which has stronger control over the flow than the mass flow boundary condition. The static pressure is adjusted for different cases to acquire the desired mass flow rate inside the intake.

For high crosswind conditions, the ground vortex has two motions named in this work primary and secondary motion. The trajectory of this motion is the same, whereas the amplitude and frequency of the secondary motion are half that of the primary one. The primary frequency of the ground vortex is roughly found to be 30 Hz. It is also learnt that the intensity of the vortex on the ground plane depends on its location in the sucked stream tube interacting with the ground. With its intensity at maximum when it is far inside the streamtube, closer to the intake, the ground vortex is weakest at the edge of the stream tube. This vortex intensity directly influences the intake AIP.

The intake separation has a very complex motion and does not exhibit periodic behaviour. Therefore frequency analysis could not produce any frequency related to separation in high crosswind conditions. Also, the secondary motion of the vortex is not seen in the medium crosswind case; this could be a result of the complex interaction between the vortex and separation.

For the medium crosswind condition, the ground vortex has a low frequency of 10 Hz, and the location of the vortex on the PIV plane is stationary. Finally, using coarse mesh in the low crosswind case, the solver predicted a steady vortex with no oscillations. Therefore, it can be concluded that with the decrease in crosswind speed, the frequency of the ground vortex oscillation decreases.

The time average results from URANS go hand in hand with the experimental results in the flow topology prediction. For a better quantitative match, the finer mesh could produce much better results with URANS using the current numerical setup.

7.2 Recommendations for future work

CFD remains the best and least expensive approach to studying the phenomenon of the ingested ground vortex. In light of this fact, here are a few suggestions:

1. A better boundary condition at the intake exit, like the choked nozzle, should be studied to address the non-uniform flow present at the intake exit due to the convected vortex, thereby nullifying the effects of numerical reflection.
2. Grid independence study should be conducted using URANS.
3. DES (Detached Eddy Simulations) could be performed using the final numerical setup and compared with URANS results.
4. Advanced data processing techniques (eg. POD) should be used to study the frequency content and mode shape of intake separation.

The ground vortex has a frequency of oscillation, and the unsteady separation has a wide range of shedding frequencies. In the usual case of a fan present at AIP, it will experience unsteady excitations at these frequencies. Therefore :

5. A fan can be placed inside the intake to see if there is any change in the aerodynamic flow features.
6. Forced harmonic response analysis can be performed on the fan to study the impact of the unsteadiness on its aeroelastic stability.

Bibliography

- [1] Jeff Overton. The growth in greenhouse gas emissions from commercial aviation. *EESI*, url: <https://www.eesi.org/papers/view/fact-sheet-the-growth-in-greenhouse-gas-emissions-from-commercial-aviation> [accessed: 2021-04-23], 2019.
- [2] Fábio Coelho Barbosa. Ultra high bypass ratio engine technology review-the efficiency frontier for the turbofanpropulsion. 2022.
- [3] DE Glenny and NGTE Pyestock. Ingestion of debris into intakes by vortex action. 1970.
- [4] Lewis A Rodert and Floyd B Garrett. Ingestion of foreign objects into turbine engines by vortices. Technical report, 1955.
- [5] John Murphy. *Intake ground vortex aerodynamics*. PhD thesis, 2008.
- [6] Wenqiang Zhang, Sina Stapelfeldt, and Mehdi Vahdati. Influence of the inlet distortion on fan stall margin at different rotational speeds. *Aerospace Science and Technology*, 98: 105668, 2020.
- [7] Keith Blincow. Intake vortex ingestion. <http://www.rob.com/pix/oops/c17vortex>.
- [8] JS Green. Forced response of a large civil fan assembly. In *Turbo Expo: Power for Land, Sea, and Air*, volume 43154, pages 685–692, 2008.
- [9] Thomas Berthelon, Alain Dugeai, Jonathan Langridge, and Fabrice Thouverez. Analysis of vortex ingestion impact on the dynamic response of the fan in resonance condition. In *Turbo Expo: Power for Land, Sea, and Air*, volume 58684, page V07AT36A010. American Society of Mechanical Engineers, 2019.
- [10] Harold Klein. *An aerodynamic screen for jet engines*. Institute of the Aeronautical Sciences, 1957.

- [11] D Motycka, W Walter, and G Muller. An analytical and experimental study of inlet ground vortices. In *9th Propulsion Conference*, page 1313, 1973.
- [12] S Brix, G Neuwerth, and D Jacob. The inlet-vortex system of jet engines operating near the ground. In *18th applied aerodynamics conference*, page 3998, 2000.
- [13] Harold J Klein. Vortex inhibitor for aircraft jet engines, December 1 1959. US Patent 2,915,262.
- [14] James Franklin Campbell. *Patterns in the sky: natural visualization of aircraft flow fields*, volume 514. NASA, Langley Research Center, 1994.
- [15] Luís Gustavo Trapp and Roberto da Motta Girardi. Crosswind effects on engine inlets: The inlet vortex. *Journal of aircraft*, 47(2):577–590, 2010.
- [16] Luis Gustavo Trapp and Roberto Girardi. Evaluation of engine inlet vortices using cfd. In *50th AIAA Aerospace Sciences Meeting including the New Horizons Forum and Aerospace Exposition*, page 1200, 2012.
- [17] Jingjing Chen, Yadong Wu, Ouyang Hua, and Anjenq Wang. Research on the ground vortex and inlet flow field under the ground crosswind condition. *Aerospace Science and Technology*, 115:106772, 2021.
- [18] H Kline. Small scale tests on jet engine pebble aspiration tests. *Douglas Aircraft Company, Report SM-14885*, 1953.
- [19] JL Colehour and BW Farquhar. Inlet vortex. *Journal of Aircraft*, 8(1):39–43, 1971.
- [20] F De Siervi, HC Viguier, EM Greitzer, and CS Tan. Mechanisms of inlet-vortex formation. *Journal of Fluid Mechanics*, 124:173–207, 1982.
- [21] W Liu, EM Greitzer, and CS Tan. Surface static pressures in an inlet vortex flow field. 1985.
- [22] Wen Liu. *Design and analysis of an experimental facility for inlet vortex investigation*. PhD thesis, Massachusetts Institute of Technology, 1982.
- [23] HW Shin, EM Greitzer, WK Cheng, CS Tan, and CL Shippee. Circulation measurements and vortical structure in an inlet-vortex flow field. *Journal of Fluid Mechanics*, 162:463–487, 1986.

- [24] A Nakayama and JR Jones. Correlation for formation of inlet vortex. *AIAA journal*, 37(4):508–510, 1999.
- [25] Arne Karlsson and Laszlo Fuchs. Time evolution of the vortex between an air inlet and the ground. In *38th Aerospace Sciences Meeting and Exhibit*, page 990, 2000.
- [26] Arne Karlsson and Laszlo Fuchs. Vortex systems and the interaction between an air inlet and the ground. In *ICAS 2000 Congress*, pages 522–1, 2000.
- [27] Norbert C Bissinger and Gerhard W Braun. On the inlet vortex system. Technical report, 1974.
- [28] Andrei Secareanu, Dragos Moroianu, Arne Karlsson, and Laszlo Fuchs. Experimental and numerical study of ground vortex interaction in an air-intake. In *43rd AIAA aerospace sciences meeting and exhibit*, page 1206, 2005.
- [29] Yoram Yadlin and Arvin Shmilovich. Simulation of vortex flows for airplanes in ground operations. In *44th AIAA Aerospace Sciences Meeting and Exhibit*, page 56, 2006.
- [30] M Jermy and Wei Hua Ho. Location of the vortex formation threshold at suction inlets near ground planes by computational fluid dynamics simulation. *Proceedings of the Institution of Mechanical Engineers, Part G: Journal of Aerospace Engineering*, 222(3):393–402, 2008.
- [31] S Zantopp, D MacManus, and John Murphy. Computational and experimental study of intake ground vortices. *The Aeronautical Journal*, 114(1162):769–784, 2010.
- [32] Nityabh Mishra, D MacManus, and John Murphy. Intake ground vortex characteristics. *Proceedings of the Institution of Mechanical Engineers, Part G: Journal of Aerospace Engineering*, 226(11):1387–1400, 2012.
- [33] Nathan Rosendo Horvath. *Inlet vortex formation under crosswind conditions*. PhD thesis, Worcester Polytechnic Institute, 2013.
- [34] Jeffrey Flamm. Aiaa propulsion aerodynamics workshop. <https://paw.larc.nasa.gov/paw5-inlet-test-case/>, Apr 2021.
- [35] JP Murphy and DG MacManus. Ground vortex aerodynamics under crosswind conditions. *Experiments in Fluids*, 50(1):109–124, 2011.
- [36] Cranfield University. Cranfield wind tunnel. <https://www.cranfield.ac.uk/facilities/8x6-wind-tunnel>.

- [37] Markus Raffel, Christian E Willert, Jürgen Kompenhans, *et al.* *Particle image velocimetry: a practical guide*, volume 2. Springer, 1998.
- [38] NASA. 5th aiaa propulsion aerodynamic workshop 2020 paw05 – ground vortex intake. https://paw.larc.nasa.gov/wp-content/uploads/sites/83/2020/08/PAW5_Inlet_Participant_Guide.pdf.
- [39] Jeyatharsan Selvanayagam, Cristhian Aliaga, and John Stokes. Cfd simulation of ground vortex intake test case using ansys fluent. In *AIAA SCITECH 2022 Forum*, page 0222, 2022.
- [40] Andre F Ribeiro. Unsteady analysis of ground vortex ingestion with lbm-vles. In *AIAA SCITECH 2022 Forum*, page 0224, 2022.
- [41] Luis Gustavo Trapp, Kelvin Cristofalo de Moraes, Diego F Abreu, and Luiz Tobaldini Neto. Comparison of cfd ground vortex results with the 5th paw intake near the ground experiment. In *AIAA SCITECH 2022 Forum*, page 0223, 2022.
- [42] Amarnatha Sarma Potturi, Oshin Peroomian, and Paul Batten. Computational analysis of an inlet ground vortex test case using cfd++. In *AIAA SCITECH 2022 Forum*, page 1252, 2022.
- [43] Deric A Babcock, Luiz Tobaldini Neto, Zach Davis, Kristen Karman-Shoemake, Carolyn Woeber, Raul Bajimaya, and David MacManus. Summary of the 5th propulsion aerodynamics workshop: Inlet cross-flow results. In *AIAA SCITECH 2022 Forum*, page 0814, 2022.
- [44] Lennart Harjes, Christoph Bode, Jonas Grubert, Philip Frantzheld, Patrick Koch, and Jens Friedrichs. Investigation of jet engine intake distortions caused by crosswind conditions. *Journal of the Global Power and Propulsion Society*, 4:48–62, 2020.
- [45] Sylvain Mouton. Simulation of atmospheric boundary layer for air inlet testing in crossflow. *AIAA Journal*, 59(7):2603–2612, 2021.
- [46] P. Spalart and S. Allmaras. A one-equation turbulence model for aerodynamic flows. In *30th Aerosp. Sci. Meet. Exhib.*, Reston, Virigina, January 1992. American Institute of Aeronautics and Astronautics. doi: 10.2514/6.1992-439. URL <http://arc.aiaa.org/doi/10.2514/6.1992-439>.

- [47] Stephen B. Pope. *Turbulent Flows*. Cambridge University Press, Cambridge, 2000. ISBN 978-0-521-59886-6. URL <https://www.cambridge.org/core/books/turbulent-flows/69322053C06F73F7EB7124915F9256BD>.
- [48] Xiao He, Fanzhou Zhao, and Mehdi Vahdati. Evaluation of Spalart-Allmaras turbulence model forms for a transonic axial compressor. In *Proc. Glob. Power Propuls. Soc.*, pages GPPS-CH-2020-0013, Chania, Greece, 2020.
- [49] Xiao He, Fanzhou Zhao, and Mehdi Vahdati. Detached Eddy Simulation: Recent Development and Application to Compressor Tip Leakage Flow. *Journal of Turbomachinery*, 144(1):011009, January 2022. ISSN 0889-504X, 1528-8900. doi: 10.1115/1.4052019. URL <https://asmedigitalcollection.asme.org/turbomachinery/article/144/1/011009/1115511/Detached-Eddy-Simulation-Recent-Development-and>.
- [50] Philippe Spalart and Steven Allmaras. A one-equation turbulence model for aerodynamic flows. In *30th aerospace sciences meeting and exhibit*, page 439, 1992.
- [51] PR Spalart and M Shur. On the sensitization of turbulence models to rotation and curvature. *Aerospace Science and Technology*, 1(5):297–302, 1997.
- [52] Christopher Rumsey. Turbulence modeling resource. <https://turbmodels.larc.nasa.gov/spalart.html#sa>, May 2022.
- [53] Michael L Shur, Michael K Strelets, Andrey K Travin, and Philippe R Spalart. Turbulence modeling in rotating and curved channels: assessing the spalart-shur correction. *AIAA journal*, 38(5):784–792, 2000.
- [54] Kazuomi Yamamoto, Kentaro Tanaka, and Mitsuhiro Murayama. Effect of a nonlinear constitutive relation for turbulence modeling on predicting flow separation at wing-body juncture of transonic commercial aircraft. In *30th AIAA Applied Aerodynamics Conference*, page 2895, 2012.
- [55] Philippe R Spalart. Strategies for turbulence modelling and simulations. *International journal of heat and fluid flow*, 21(3):252–263, 2000.
- [56] Julien Dandois. Improvement of corner flow prediction using the quadratic constitutive relation. *AIAA journal*, 52(12):2795–2806, 2014.

- [57] CL Rumsey, J-R Carlson, TH Pulliam, and PR Spalart. Improvements to the quadratic constitutive relation based on nasa juncture flow data. *AIAA Journal*, 58(10):4374–4384, 2020.